CENTRAL CIRCUITRY UNDERLYING THE MEDIAL OLIVOCOCHLEAR EFFERENT SYSTEM

By

Gabriel Enrique Romero

A DISSERTATION

Presented to the Department of Physiology & Pharmacology
and the Oregon Health & Science University
School of Medicine
in partial fulfillment of
the requirement for the degree of

Doctor of Philosophy

February 2021

School of Medicine

Oregon Health & Science University

CERTIFICATE OF APPROVAL

This is to certify that the PhD dissertation of

Gabriel Enrique Romero

has been approved

_____

Advisor, Laurence Trussell, PhD

_____

Member and Chair, Stephen David, PhD

_____

Member, Catherine Morgans, PhD

_____

Member, Lina Reiss, PhD

_____

Member, Tianyi Mao, PhD

_____

Member, Sue Aicher, PhD

TABLE OF CONTENTS

LIST OF FIGURES

LIST OF TABLES

LIST OF ABBREVIATIONS

ABBREVIATION	FULL DESCRIPTION
4V	Fourth ventricle
7N	Facial motor nucleus
AAV	Adeno-associated virus
AChE	Acetylcholinesterase
AMPA	α-amino-3-hydroxy-5-methyl-4-isoxazolepropionic acid
AMPAR	AMPA receptor
ANOVA	Analysis of variance
AVCN	Anterior ventral cochlear nucleus
BAC	Bacterial artificial chromosome
CGRP	Calcitonin gene-related peptide
ChAT	Choline acetyltransferase
ChR2	Channelrhodopsin
cIC	Contralateral inferior colliculus
C_m	Membrane capacitance
CNS	Central nervous system
CP-AMPAR	Calcium permeable AMPA receptor
CTB	Cholera toxin subunit-B
DAQ	Data acquisition instrument
DCN	Dorsal cochlear nucleus
DPOAE	Distortion product otoacoustic emission
EBFP	Enhanced blue fluorescent protein
EDTA	Ethylenediaminetetraacetic acid
EGTA	Ethylene glycol-bis(β-aminoethyl ether)-N,N,N′,N′-tetraacetic acid
EPSC	Excitatory postsynaptic current
EPSG	Excitatory postsynaptic conductance
E_r	Reversal potential
EYFP	Enhanced yellow fluorescent protein
FS	Firing sensitivity
GABA	γ-aminobutyric acid
GBC	Globular bushy cell
GFP	Green fluorescent protein
GlyT2	Glycine transporter 2
grC	Granule cell layer
HCN	Hyperpolarization-activated cyclic nucleotide–gated
HRP	Horseradish peroxidase
IC	Inferior colliculus
IEI	Inter-event interval
IHC	Inner hair cell
iIC	Ipsilateral inferior colliculus

LL	Lateral lemniscus
LNTB	Lateral nucleus of the trapezoid body
LOC	Lateral olivocochlear
LSO	Lateral superior olive
mcp	Middle cerebellar peduncle
mEPSC	Miniature excitatory postsynaptic current
MG	Medial geniculate
MNTB	Medial nucleus of the trapezoid body
MOC	Medial olivocochlear
nAChR	Nicotinic acetylcholine receptor
NLL	Nucleus of the lateral lemniscus
NMDA	N-Methyl-D-aspartate
OCB	Olivocochlear bundle
OHC	Outer hair cell
PBS	Phosphate buffer solution
PSCC	Posterior semicircular canal
PSTH	Peristimulus time histogram
PVCN	Posterior ventral cochlear nucleus
R_m	Membrane resistance
RPO	Rostral periolivary nucleus
SGN	Spiral ganglion neuron
SK2	Small conductance calcium-activated potassium channel
SOC	Superior olivary complex
Sst	Somatostatin
TEA	Tetraethylammonium
TTX	Tetrodotoxin
VCN	Ventral cochlear nucleus
V_m	Membrane voltage
VNLL	Ventral nucleus of the lateral lemniscus
VNTB	Ventral nucleus of the trapezoid body
WPRE	Woodchuck hepatitis virus posttranscriptional regulatory element

ACKNOWLEDGEMENTS

Most importantly, I thank Dr. Larry Trussell. None of the findings described in this dissertation would have been possible without his encouragement, creativity, and guidance. He constantly pushed me to explore scientific questions in new ways, and gave me greater appreciation for the implications of this work. Thank you for teaching me to be a neurophysiologist—your professional training and personal advice will follow me throughout my career and life.

Special thanks to my current and former labmates, Tavita Garrett and Doug Zeppenfeld, and Drs. Dan Yaeger, Hsin-Wei Lu, Tomohiko Irie, Luci Moore, Jeffrey Tang, Tim Balmer, Tenzin Ngodup, and Hui Hong. The world of patch clamp electrophysiology would have been difficult to navigate if not for their support, friendship, and advice. Thanks also to Michael Bateschell, Ruby Larisch, Jenn Goldsmith, and Sean Elkis for providing vital assistance with mouse husbandry, genotyping, and technical assistance over the years.

Much thanks to current and previous committee members, Drs. Stephen David, Tianyi Mao, Catherine Morgans, Lina Reiss, Sue Aicher, and Craig Jahr for the invaluable mentorship they have provided me. Their excellent feedback and suggestions substantially impacted this work and my development as a scientist.

I am very grateful to Drs. Robert Miller and Lilian Yuan for providing me the opportunity to work as a technician in each of their laboratories at the University of

Minnesota nearly a decade ago. It was there where I gained curiosity and enthusiasm for scientific work. I would also like to thank Drs. Anusha Mishra and Steve Sullivan; they have provided encouragement and advice since the very beginning of my scientific career, and commented on early drafts of this dissertation.

Thanks are also due to the Howard Hughes Medical Institute for their financial assistance, and the community that came along with it. The friends and colleagues that I have made through the Gilliam Fellowship are irreplaceable.

I am truly thankful for all of the support I've received from family and friends when outside of the laboratory. First and foremost, thank you to my wife, Megan Romero, for encouraging me along every step of the way. As ever, I'm immensely thankful to my parents, Julie Kay Leslie and Enrique Romero, for raising me to always follow my passions. And thank you to my brother, Jacob Romero, for providing moral support and professional advice. Finally, many thanks to the friendships I cultivated at Oregon Health and Science University and beyond. They have also helped shape my scientific journey and I would be remiss not to acknowledge their contributions.

ABSTRACT

The medial olivocochlear (MOC) system aids in the prevention of age- and noise-induced hearing loss, and enhances the detection of salient sound in diverse sensory environments. In response to sound the MOC system acts as a reflex and exerts control over the level of cochlear gain in a frequency and intensity specific manner. This direct inhibitory control over acoustic amplification is provided by cholinergic MOC efferent neurons, which synapse directly onto sensory hair cells in the cochlea. While function of the MOC system has been well studied at the level of the periphery, there are gaps in our knowledge concerning the underlying central circuitry—hindering our understanding of the protective role of efferent neurons and the central mechanisms underlying their normal function. The present study used an optogenetic and electrophysiological approach to investigate excitatory responses of MOC neurons to ascending ventral cochlear nucleus (VCN) and descending inferior colliculus (IC) inputs. MOC neurons were found to be homogeneous in their spike firing properties and remarkably well suited to encoding stimulus intensity. Both sources of input transmitted to postsynaptic Ca^{2+}-permeable AMPARs. Surprisingly, ascending and descending input to MOC neurons utilized opposite forms of short-term plasticity, such that descending inputs from IC grew stronger, while ascending inputs weakened during repetitive stimulation. Conductance clamp experiments revealed that the plasticity of these inputs are specialized for maintaining repetitive firing over a surprisingly wide dynamic range. Furthermore, ascending input responsible for mediating the acoustically evoked MOC reflex could be enhanced or overridden by powerful IC input, implicating a dominant role for descending pathways over the strength of cochlear amplification.

CHAPTER I: INTRODUCTION TO AUDITORY EFFERENTS

1.1 Parallel processing of sound utilizes ascending and descending pathways

Nervous systems depend on sensory modalities to form a subjective experience of the external environment. This information is assigned importance in a context-dependent manner to inform decisions that result in behavior. For example, an auditory percept may be relegated to "background noise", such as hearing a person speak in a hushed voice in an adjacent room. However, if one believed they were home alone this same auditory stimulus would be prominent, likely causing great alarm and requiring immediate attention. This dynamic extraction and encoding of relevant information from acoustic signals is optimized through a wealth of specialized parallel processing pathways in the brain.

The ascending auditory pathway begins with the cochlea and consists of many interconnected nuclei, culminating in the auditory cortex (Figure 1.1) (Smith and Spirou, 2002; Malmierca, 2003; Cant, 2019). Sound waves that enter the ear are detected by tonotopically arranged sensory cells, called hair cells, which transduce mechanical vibrations to electrical signals. These signals are transmitted to auditory nerve fibers, forming the 8^{th} cranial nerve, which enters the brainstem and provides excitatory input to the cochlear nucleus, where all central auditory processing begins. These fibers bifurcate and send collaterals to ventral and dorsal regions of the cochlear nucleus (VCN and DCN, respectively), beginning the partition of auditory signals into parallel processing

pathways, while at the same time preserving their tonotopicity. Each successive nucleus contains microcircuits made of multiple populations of neurons with different morphologies, inputs, projection targets, transmitters, and physiological properties (Cant and Oliver, 2018). The auditory system's computational workload is distributed among these specialized microcircuits, allowing for increased processing speed as each is individually tasked with encoding specific features of sound. The schematic in Figure 1.1

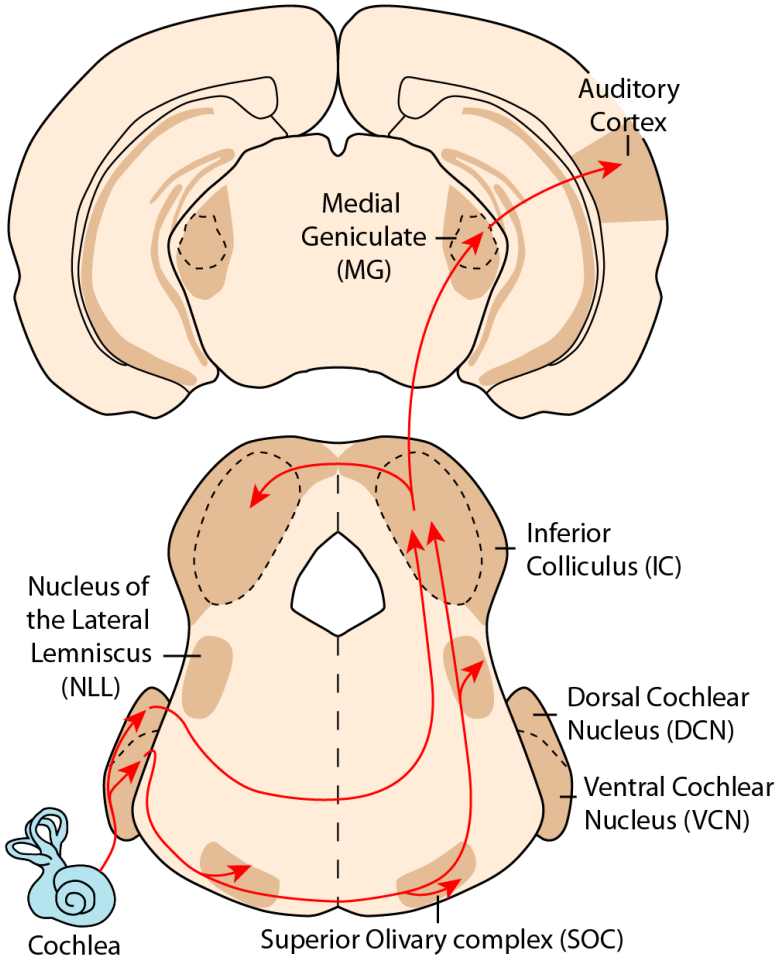

Figure 1.1: Simplified illustration of the rodent ascending auditory pathway. Spiral ganglion neurons of the auditory nerve bifurcate and project to the ventral and dorsal cochlear nucleus (VCN and DCN, respectively). The cochlear nucleus sends a majority of its ascending projections to the contralateral inferior colliculus (IC) and nucleus of the lateral lemniscus (NLL), with bilateral axon collaterals to the superior olivary complex (SOC). Projections from IC terminate in the medial geniculate (MG) of the thalamus, which provides sensory input to auditory cortex.

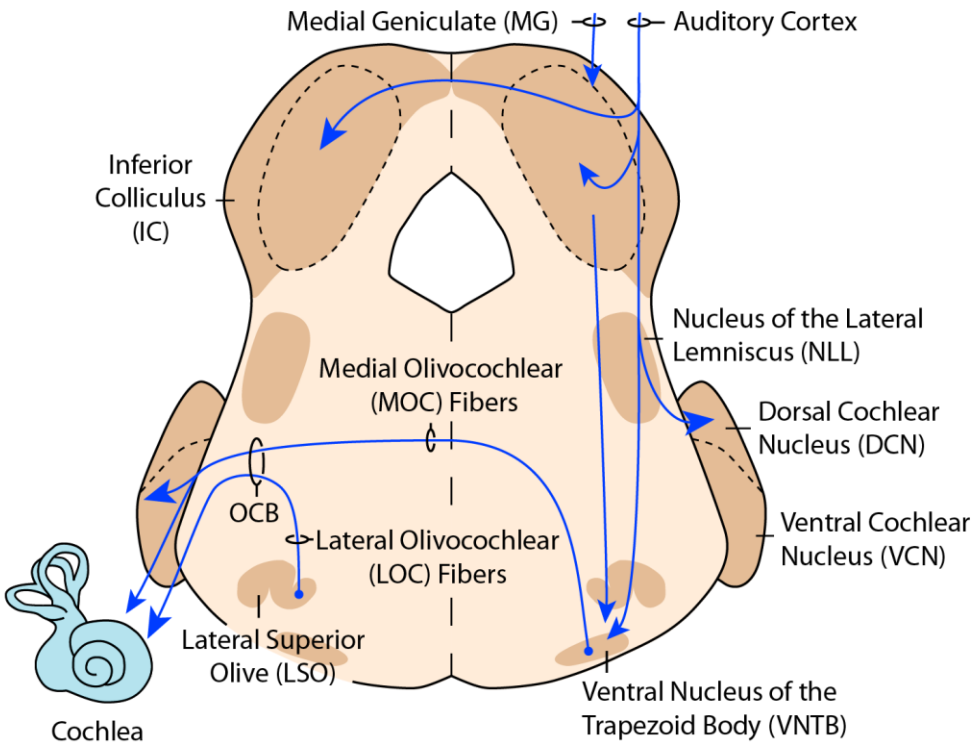

Figure 1.2: Simplified illustration of the rodent descending auditory pathway. The auditory cortex sends far-spanning projections to MG (thalamus), IC (midbrain), and brainstem (NLL, DCN, and VNTB). Fibers from medial- and lateral-olivocochlear (MOC and LOC) efferent neurons project from the ventral nucleus of the trapezoid body (VNTB) and lateral superior olive (LSO) of the SOC, respectively. These fibers converge and form the olivocochlear bundle (OCB), which sends collaterals to VCN, and terminates in the cochlea.

implies there is a direct flow of information from one well-defined nucleus to the next; however, they are highly interconnected—as each structure projects to many targets, and receives input from many sources, including the descending auditory pathway.

Largely, the descending pathway operates in reverse (Figure 1.2), providing higher levels of the auditory system extensive opportunity to modulate and influence the processing of acoustic signals. The auditory cortex alone sends subcollicular projections

to numerous midbrain and brainstem areas, including inferior colliculus (IC), the superior olivary complex (SOC), and cochlear nuclei (Saldaña, 2015). Of the many nuclei receiving cortical input, the ventral nucleus of the trapezoid body (VNTB) of the SOC is emerging as a major hub of the descending auditory pathway (Schofield and Beebe, 2019), as it distributes higher-level input to many subcortical targets and sends efferent projections directly to the cochlea.

1.2 Olivocochlear efferents provide central control over auditory input

Since Grant Rasmussen's discovery of auditory efferent fibers (1946, 1953) it has been evident that the central nervous system could directly control or modulate auditory signals at the level of the cochlea, before any processing of these signals in central auditory nuclei. Indeed, soon after their discovery it was found that electrical stimulation of these fibers suppressed sound-evoked auditory nerve activity (Galambos, 1956), demonstrating inhibitory control over acoustic input. These early anatomical and physiological studies suggested that cochlear output through the auditory nerve was influenced both by acoustic stimuli and input from the central nervous system. Thus, auditory efferent neurons represent the final and only connection of the descending auditory pathway to the cochlea (Figure 1.2), and provide the earliest point of intersection between descending and ascending pathways.

It is accepted that efferent neurons modulate acoustic input at the most peripheral neural level. However, as their anatomy and physiology have been further revealed their

role in hearing has become increasingly multifaceted. Most strikingly, Warr and Guinan's (1979) discovery of two distinct efferent systems, lateral and medial olivocochlear efferents (LOC and MOC, respectively), suggested even more complexity and specialization of descending modulation. Therefore, it is first important to understand the anatomy and physiology of these two systems in order to gain insight into their potential roles in hearing. This dissertation is focused on the MOC efferent system; however, because LOC and MOC efferents are historically and biologically intertwined, both will be discussed in this introduction.

1.3 Neuroanatomy of olivocochlear efferents

Efferent projections to the cochlea originating from the olivary complex were first identified by anterograde degeneration studies using the Marchi method, an osmium-based stain (Rasmussen, 1946, 1953). Hence, they are referred to in this text by their anatomically derived name, "olivocochlear" efferents. Nearly thirty years after their discovery, Warr (1975) revealed their somatic morphology, approximate quantity, and bilateral distribution within the brainstem. His seminal characterization of auditory efferents was accomplished by post-hoc visualization of a retrograde label, horseradish peroxidase (HRP), after injection into the cochlear labyrinth of kittens. In the same study, Warr demonstrated that retrogradely labeled somata histochemically colocalized with acetylcholinesterase (AChE), indicating that olivocochlear efferent neurons were cholinergic and therefore may transmit with acetylcholine to sensory epithelium in the cochlea.

Olivocochlear efferents form two distinct groups of neurons which provide divergent innervation of the cochlea, termed LOC and MOC due to their relatively lateral and medial somatic locations within the olivary complex (Warr & Guinan, 1979). Generally, LOC neuron somata reside in the lateral superior olive (LSO), and terminate onto type I spiral ganglion neuron (SGN) dendrites directly beneath inner hair cells (IHCs) in the ipsilateral cochlea (Figure 1.3) (Warr and Guinan, 1979; Robertson, 1985; Brown, 1987; Warr et al., 1997). The LOC neurons can be further divided into two subgroups: smaller "intrinsic" neurons, which are restricted to the LSO, and larger "shell" neurons, which are sparse in number and border the margins of the same nucleus (Vetter and Mugnaini, 1992). Dendrites of intrinsic neurons align parallel to isofrequency bands

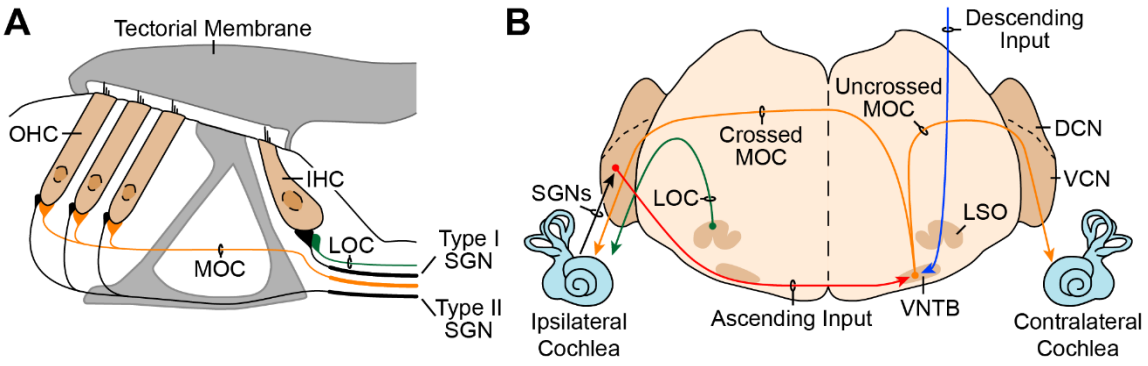

Figure 1.3: General anatomy of efferent pathways. (**A**) Schematic of efferent and afferent innervation of the organ of Corti in the cochlea. Unmyelinated lateral olivocochlear (LOC) fibers synapse onto afferent dendrites of type I spiral ganglion neurons (SGN), near inner hair cells (IHC). Myelinated medial olivocochlear (MOC) fibers synapse onto outer hair cells (OHC) near type II SGN dendrites. (**B**) Coronal brainstem schematic of efferent related pathways. Afferent fibers (type I and type II SGNs) terminate in the dorsal and ventral cochlear nuclei (DCN and VCN, respectively). Axons from ascending VCN neurons (likely T-stellate cells) cross the midline and terminate on MOC neurons in the ventral nucleus of the trapezoid body (VNTB). Crossed and uncrossed MOC neurons innervate ipsilateral and contralateral cochleae, respectively. LOC neurons innervate the ipsilateral cochlea. MOC neurons receive descending input from auditory cortex and inferior colliculus.

within the LSO, whereas shell neurons extend their dendrites into the LSO and to the surrounding reticular formation.

MOC neurons reside in medial nuclei of the SOC, predominantly in the VNTB (Figure 1.3 B) (Brown & Levine, 2008; Warr, 1975). While individual MOC neurons from both sides of the brainstem project axons to either cochlea, where they directly synapse onto outer hair cells (OHCs) (Figure 1.3 A) (Warr & Guinan, 1979), in most species they are biased toward contralateral projections (Warr, 1992). When unilaterally stimulated with an electrode near their somata, MOC neurons act strongest on the contralateral ear (Gifford and Guinan, 1987), reflecting their anatomical preference for contralateral projections. Additionally, the location of MOC neuron somata extend more rostral than LOC neurons, spanning the entirety of the rostral periolivary region (RPO) (Vetter & Mugnaini, 1992; Warr et al., 2002). While the total number of olivocochlear neurons can vastly differ between and within different species, the estimated ratio of MOC compared to LOC neurons is generally low. For example, out of approximately 1,365 olivocochlear neurons in humans, about 26% are MOC and 74% are LOC (Arnesen, 1984). Similarly, out of approximately 475 olivocochlear neurons in mice, about 35% are MOC and 65% are LOC (Campbell and Henson, 1988).

Unlike LOC neurons, which have thin unmyelinated axons, MOC axons are thicker and heavily myelinated (Guinan et al., 1983). Together, these mixed-diameter fibers enter the cochlea at the basal turn alongside afferent SGNs of the auditory nerve.

Before the discovery of two separate efferent systems, all olivocochlear fibers were originally categorized as either “crossed” or “uncrossed” with respect to the midline of the brainstem (Rasmussen, 1946). While olivocochlear fibers are now better described as LOC or MOC, the “crossed” and “uncrossed” terminology is still useful for distinguishing fibers within each efferent system, as they each send projections to both cochlea. Generally, projections from individual LOC neurons are to ipsilateral cochlea, while MOC neurons project to contralateral cochlea and in rare instances (~5.4%) bifurcate and terminate in both (Robertson et al., 1987).

Collateral branches from MOC axons en route to the cochlea terminate in the cochlear nucleus around areas with a high density of granule cells (Liberman and Brown, 1986; Brown et al., 1988) and less so in the core of the VCN (Osen et al., 1984; Ryan et al., 1990; Brown, 1993). Olivocochlear collaterals also target vestibular nuclei (Brown et al., 1988; Ryan et al., 1990; Brown, 1993; Benson and Brown, 1996). It has been proposed that shell LOC neurons send collaterals to VCN, whereas intrinsic LOC neurons do not (Ryan et al., 1990; Horváth et al., 2000). Interestingly, dendrites of type II SGNs contact OHCs in the cochlea and send collaterals to the granule-cell lamina of the cochlear nucleus (Brown and Ledwith, 1990), both which are targets of MOC neurons. This suggests that MOC neurons may influence type II SGN signaling directly or indirectly via their presynaptic inputs or post-synaptic targets.

1.4 Medial olivocochlear reflex pathway

MOC neurons are involved in a reflex pathway which uses sound-driven input to provide inhibitory feedback to the cochlea (Guinan, 2018). This reflex is bilateral, as sound delivered to one ear elicits both ipsilateral and contralateral cochlear responses (Robertson, 1984; Liberman and Brown, 1986; Brown, 1989). The three-neuron arc forming the MOC reflex begins and ends in the organ of Corti, starting with type I SGNs that project to the cochlear nucleus and ending with MOC neuron terminals on OHCs (Figure 1.3 A). The precise identity of the neurons mediating this arc, termed "reflex interneurons", are unknown ("Ascending input" in Figure 1.3 B). Mounting evidence suggests they consist of ascending projection neurons that originate from the posteroventral cochlear nucleus (PVCN) (Robertson and Winter, 1988; Thompson and Thompson, 1991; De Venecia et al., 2005). Using tract-tracing techniques, T-stellate (planar multipolar) neurons have been identified as a putative interneuron (Warr, 1972; Darrow et al., 2012). Anatomically, they are well-positioned to transmit acoustic signals to MOC neurons as they receive auditory nerve input, their somata primarily reside in PVCN, and they innervate VNTB (Oertel et al., 2011). In response to tones, T-stellate neurons fire sustained action potentials that increase monotonically with sound intensity (Rhode and Smith, 1986; Smith and Rhode, 1989), similar to *in vivo* responses recorded from MOC fibers (Liberman and Brown, 1986; Brown, 1989). However, their specific synapse onto MOC neurons has not been definitively described nor functionally demonstrated.

Cochlear nuclei may provide additional input to MOC neurons. Bushy cells of the VCN send projections with calyceal-like endings to VNTB and RPO (Smith et al., 1993). This type of bouton has been observed on MOC neurons in the albino rat using electron-microscopy (White, 1986), supporting the possibility that bushy cells may also be a source of input. Using injected tract-tracers, Ye et al. (2000) determined that the marginal shell of the anteroventral cochlear nucleus (AVCN) may also project to MOC neurons, but these findings have not been well-reproduced with other methods. For example, retrograde transneuronal tract-tracing from MOC neurons using pseudorabies virus abundantly labeled many VCN neurons, but not the marginal shell region (Brown et al., 2013). Additionally, kainic acid lesions of PVCN, but not AVCN, impeded the ipsilateral MOC reflex (De Venecia et al., 2005).

The ipsilateral reflex pathway is often describe as “double crossed” with respect to the midline of the brain (Warr, 1992; Guinan, 2011, 2018), as (1) reflex interneuron axons cross it and synapse onto contralateral MOC neurons, which (2) cross back over to the ipsilateral cochlea (crossed MOC, Figure 1.3 B). MOC neurons which receive crossed interneuron input but do not cross the midline themselves are thought to be involved in the contralateral reflex (uncrossed MOC, Figure 1.3 B). However, the interneuron projections are incompletely described and likely also provide ipsilateral input to MOC neurons (Thompson and Thompson, 1991). Indeed, at least some T-stellate neurons project to ipsilateral VNTB (Warr, 1995; Doucet and Ryugo, 2003; Darrow et al., 2012) where they may synapse onto MOC neurons.

In silent backgrounds, most olivocochlear fibers respond only to ipsilateral or contralateral sound stimuli but not the other (Liberman and Brown, 1986; Brown, 1989). However, a great majority of these same unilaterally activated fibers respond more robustly when sound is presented to both ears simultaneously (Liberman, 1988a). This suggests that many MOC neurons either receive interneuron input from ipsilateral and contralateral VCN, or that binaural stimuli utilize a pathway which differs from that of the canonical reflex pathway.

1.5 Descending and modulatory inputs to medial olivocochlear neurons

MOC neurons receive descending input from higher brain regions that may control or modulate the reflex pathway. These inputs originate from IC (Faye-Lund, 1986; Thompson and Thompson, 1993; Vetter et al., 1993; Mulders and Robertson, 2002) and auditory cortex (Figure 1.2 and 1.3 B) (Mulders and Robertson, 2000; Coomes and Schofield, 2007). Descending IC projections are glutamatergic, tonotopically arranged, and mainly target ipsilateral VNTB (Caicedo and Herbert, 1993; Schofield and Cant, 1999; Suthakar and Ryugo, 2017). This input contacts many VNTB cell-types, including MOC neurons. As the IC is a major site of convergence for auditory and non-auditory pathways it likely integrates multimodal information to fine tune MOC fiber output. Electrical stimulation of the IC results in decreased sound-evoked auditory nerve activity and suppression of distortion product otoacoustic emissions (DPOAEs) (Mulders and Robertson, 2000, 2002; Popelar et al., 2002; Groff and Liberman, 2003; Zhang and Dolan, 2006), which are ear-canal sounds mediated by OHCs (Guinan, 2018). This

suggests the IC can directly enhance MOC inhibition of cochlear gain. As electrical stimulation is non-specific the detected effects could alternatively have resulted from antidromic activation of T-stellate neurons, which are a major source of ascending input to IC and likely contact MOC neurons (Oertel et al., 2011). That being said, it is unclear to what extent individual T-stellate neurons contact MOC neurons, IC neurons, or both.

The VNTB receives neuromodulatory input from many brainstem nuclei, some of which directly contact MOC neurons. Serotonergic and noradrenergic varicosities have been identified in the VNTB using tract-tracing and histochemical techniques (Thompson and Thompson, 1995; Mulders and Robertson, 2000), and likely originate from raphe nuclei and locus coeruleus, respectively (Mulders and Robertson, 2001; Horvath et al., 2003; Brown et al., 2013). There is also evidence for peptidergic input as terminals containing substance P, cholecystokinin and encephalin appear to be in close apposition to MOC somata and dendrites (Mulders and Robertson, 2000). Wang and Robertson (1997, 1998) found that bath application of noradrenaline and substance P onto voltage-clamped MOC neurons generally elicited an excitatory response, suggesting these types of input enhance efferent signaling. While their role in regard to hearing is unknown, these inputs presumably modulate efferent action in response to changes in global brain state.

1.6 Action of olivocochlear efferents in the cochlea

When sounds enter the inner ear, they cause oscillatory motions which travel along the cochlea as a wave (Von Békésy, 1960; Hudspeth, 1989). This wave travels from the base of the basilar membrane toward the apex, encoding high- to low-frequency sound, respectively. The wave's amplitude is actively boosted by the "cochlear amplifier", which is a positive feedback mechanism mediated by OHCs (LeMasurier and Gillespie, 2005; Dallos, 2008). Ultimately, this same wave is detected by IHCs which transmit to SGNs of the auditory nerve. Olivocochlear efferents directly impact these cochlear functions by exerting control over the cochlear amplifier and output of the auditory nerve. Briefly, the process by which hair cells detect and transmit sound input will be reviewed in order to better understand the impact of olivocochlear efferents on cochlear mechanics and auditory signaling.

Sound-induced vibrations are detected and converted into electrical conductances by tonotopically arranged sensory hair cells using a process termed mechanotransduction (Hudspeth and Jacobs, 1979). This process begins in hair bundles on the apical surface of these cells which are exceptionally sensitive to mechanical deflections. Movement of the hair bundle triggers the opening of a non-selective cation channel, the transduction channel (Corey and Hudspeth, 1979), which is likely formed by dimerized transmembrane channel-like proteins 1 and 2 (TMC1 and TMC2) (Pan et al., 2018; Jia et al., 2020). While this channel is nonspecific to many cations, its current is largely carried

by potassium *in vivo* (Corey and Hudspeth, 1979) as mammalian hair bundles are exposed to endolymph, a high-potassium extracellular fluid.

Each cochlear hair cell type exhibits a specialized response to mechano-transduction. In IHCs, depolarization causes the opening of voltage-dependent calcium channels on the basolateral surface which initiates graded release of an excitatory transmitter, glutamate, onto SGNs (Koyano and Ohmori, 1996; Ottersen et al., 1998). OHCs respond to depolarization with voltage-dependent contractions and elongations (Brownell et al., 1985) mediated by the voltage-sensitive membrane protein, prestin (Zheng et al., 2000). This rapid conversion of membrane potential to movement is known as electromotility, which generates the mechanical force upon the basilar membrane responsible for cochlear amplification—thereby boosting the traveling wave at the same frequency being detected.

MOC efferents regulate OHC electromotility by controlling the membrane potential of the cell and its potassium conductance. Terminals from these efferent fibers are cholinergic and transmit to postsynaptic α9/α10 nicotinic acetylcholine receptors on the basolateral surface of OHCs that have a high permeability for calcium over sodium (Katz et al., 2000; Weisstaub et al., 2002). This calcium influx into OHCs leads to an inhibitory efflux of potassium through small conductance calcium-activated potassium (SK2) channels (Housley and Ashmore, 1991; Fuchs and Murrow, 1992a, 1992b; Kong et al., 2008). The activation of these SK2 channels is likely enhanced by calcium-induced

calcium release from intracellular stores (Wersinger and Fuchs, 2011). The resulting hyperpolarization diminishes the degree of electromotility in response to mechanotransduction, therefore reducing cochlear amplification.

LOC neurons likely modulate the postsynaptic activity of IHCs by altering the sensitivity and firing rate of auditory nerve fibers, as they directly synapse onto the dendrites of type I SGNs (Warr and Guinan, 1979; Brown, 1987). The majority of LOC neurons are cholinergic (Safieddine and Eybalin, 1992; Maison et al., 2003); however, they possibly utilize a number of additional neurotransmitters and modulators: dopamine, calcitonin gene-related peptide (CGRP), γ-aminobutyric acid (GABA), and opioid peptides (encephalins and dynorphins) (Vetter et al., 1991; Eybalin, 1993; Darrow et al., 2006; Wu et al., 2020). Currently, how LOC efferents utilize their many transmitters, the mechanisms in which they modulate auditory nerve activity, and the roles played by LOC neuron subtypes are contentious (Liberman, 1990; Groff and Liberman, 2003; Le Prell et al., 2003; Darrow et al., 2006; Maison et al., 2012). This is likely due to (1) the difficulty of specifically activating LOC neurons *in vivo*, and (2) the recent discovery that they dynamically regulate transmitter expression in response to sound exposure (Wu et al., 2020). This indicates that the content of transmitter released in the cochlea is dependent on the animal's most recent auditory experience, possibly confounding the interpretation of previous studies.

1.7 Physiology of medial olivocochlear efferents

To investigate efferent mediated effects on the cochlear response to sound, MOC fibers are typically experimentally activated in one of two ways: direct electrical stimulation of efferent axons at the floor of the fourth ventricle (the crossed olivocochlear bundle) or activation of the contralateral MOC-reflex by playing sound in the ear opposing the side being studied. As a result of efferent stimulation during sound stimuli, OHC conductance is increased. This correlates with an increase in the cochlear microphonic potential (Gifford and Guinan, 1987; Elgueda et al., 2011). Concurrently, OHC electromotility is diminished, which is reflected by a decrease in DPOAE amplitude (Mountain, 1980). This efferent-mediated suppression of cochlear gain has been verified at each successive level of sound transduction, measured as a reduction of: basilar membrane movement (Murugasu and Russell, 1996; Russell and Murugasu, 1997), the IHC intracellular potential (Brown et al., 1983; Brown and Nuttall, 1984), the auditory nerve compound action potential (Galambos, 1956; Gifford and Guinan, 1987), and single unit responses of afferent fibers (Wiederhold and Kiang, 1970; Buño, 1978; Warren and Liberman, 1989). The resulting decrease in cochlear responsiveness shifts the dynamic range of afferent fibers toward higher sound levels (Wiederhold and Kiang 1970) and broadens their frequency-threshold tuning curves (Guinan, 2006, 2018).

Tuning curves of individual MOC fibers are similar to afferent fibers of the same characteristic frequency, but their sharpness varies between species (Fex, 1962; Cody and Johnstone, 1982; Robertson, 1984; Liberman and Brown, 1986; Liberman, 1988b;

Brown, 1989, 2014). In silent backgrounds, MOC fibers show little to no spontaneous activity, but respond to noise and tone bursts with sustained spiking rates which monotonically increase with sound intensity. Their maximum *in vivo* spiking rate varies between ~20 to 140 spikes per second (Liberman, 1988a; Brown, 1989), but their overall activity considerably depends on the depth and type of anesthesia used, affecting both spontaneous and maximum firing rates (Robertson and Gummer, 1985; Brown, 1989). Recent work comparing awake to anesthetized animals confirmed that anesthesia greatly reduces MOC efferent responses (Guitton et al., 2004; Chambers et al., 2012; Aedo et al., 2015).

When presented with monaural sound stimuli the responses of individual fibers correlate well with the ratio of crossed, uncrossed, and bilateral MOC projections (see Table 7.1 in Warr, 1992, for review on anatomical distributions of fibers across species). For example, in the cat and guinea pig a majority of single fibers respond best to ipsilateral sound stimuli, a third to contralateral sounds, and a tenth to sound from either ear (Liberman and Brown, 1986; Brown, 1989). However, as mentioned previously (see Section 1.4), most MOC fibers that only respond to sound in one ear are enhanced when sound is concurrently presented in the other, a phenomenon termed “binaural facilitation”. This type of facilitation has been observed in human subjects by measuring changes in otoacoustic emissions (Lilaonitkul and Guinan, 2009).

While MOC efferent innervation of the cochlea is broader than that of afferent fibers (Brown, 2014), their suppressive effect is typically greatest at their characteristic frequency. Accordingly, MOC projections are tonotopically arranged (Liberman and Brown, 1986; Brown, 1989, 2016), with higher characteristic frequency fibers projecting toward the base of the cochlea and lower characteristic frequency fibers projecting more apically. This is generally true of all MOC fibers with the acceptation of those that respond to contralateral sounds. These fibers span greater frequency ranges in the cochlea than those that respond to ipsilateral sounds (Brown, 2014).

In response to narrow-band noise, MOC mediated inhibition is generally frequency specific, but the magnitude of inhibition increases with increasing noise bandwidth (Lilaonitkul and Guinan, 2009). Narrow-band noise is more effective ipsilaterally than contralaterally, but broadband noise elicits a more equal effect regardless of side. Binaural noise elicits the greatest response, with broadband noise eliciting the strongest response. Together, this indicates that MOC reflex output is due to the integration of inputs representing a wide spectrum of frequencies from both cochleae.

The time it takes for the MOC reflex to effect auditory nerve transmission is dependent on (1) cochlear mechanics, (2) the number of neurons involved and their axonal lengths, (3) the properties of each neuron and synapse, and (4) the time-course of OHC inhibition. When MOC fibers are directly stimulated at the olivocochlear bundle, it takes tens to hundreds of milliseconds to maximally effect the spiking rate of auditory

nerve fibers (Wiederhold and Kiang, 1970). In response to contralateral sounds, it takes ~100 to 200 milliseconds for auditory nerve fibers to reach their maximum level of suppression (Warren and Liberman, 1989). The time-course is predictably greater in response to sound than when compared to direct stimulation, as MOC neuron output is additionally dependent on the presynaptic portion of the reflex pathway. Moreover, efferent fibers seldom respond to sounds with durations less than 25 milliseconds (Liberman and Brown, 1986) reflecting a preference for sustained responses. In animal studies, the time-course of MOC suppressive effects on basilar membrane vibrations (Cooper and Guinan, 2003), DPOAEs (Liberman et al., 1996), and the auditory nerve compound action potential (Sridhar et al., 1995) can be separated into a fast component lasting tens to hundreds of milliseconds, and slow component lasting tens to hundreds of seconds. While both components are initiated by MOC activation, the slow component often persists after lesioning the olivocochlear bundle. It has been hypothesized that the slow component is due to a gradual decrease of OHC stiffness that remains after prolonged efferent activation (Cooper and Guinan, 2003; Guinan, 2011, 2018). Humans have analogous fast and slow components with similar time-courses, as measured with otoacoustic emissions (Kim et al., 2001; Backus and Guinan, 2006; Zhao and Dhar, 2011). The slow component may play a role in protecting the auditory system from acoustic trauma (Reiter and Liberman, 1995).

1.8 Multiple roles of olivocochlear efferents in hearing

Olivocochlear neurons play many roles in auditory system function and development. However, they are most commonly associated with their ability to protect the auditory system from acoustic trauma (Fuente, 2015; Guinan, 2018). Loud sounds can permanently damage cochlear sensory epithelium and auditory nerve fibers, resulting in hearing loss and tinnitus (i.e. ringing in the ears) (Kujawa and Liberman, 2009; Le et al., 2017). Depending on the frequency, intensity, and duration of noxious sound stimuli, the resulting hearing loss can be permanent or temporary. The type of loss is typically diagnosed by a hearing threshold test (e.g. audiogram) and depends on whether the elevated shift in threshold is permanent, or recovers over time. However, temporary hearing loss may be a misnomer as there is evidence for permanent afferent degeneration and terminal loss after thresholds recover to normal, a phenomenon termed "hidden hearing loss" (Kujawa and Liberman, 2009). This type of neuropathy likely contributes to perceptual dysfunctions that cannot be diagnosed merely with a threshold test.

Lesion studies suggest that both MOC and LOC efferents protect the auditory system from permanent hearing loss due to loud (>100 dB SPL) (Attanasio et al., 1999; Darrow et al., 2007) and moderate (84 dB SPL) levels of sound exposure (Maison et al., 2013). This suggests that olivocochlear neurons are needed to prevent hearing loss in everyday acoustic environments, in addition to extreme conditions. Cody and Johnstone (1982) demonstrated that temporary hearing loss due to loud sounds can be alleviated with simultaneous contralateral suppression at the same frequency. It is likely that MOC

mediated inhibition of the cochlear amplifier protects the auditory system by reducing the extent of vibrational damage in the cochlea and by reducing excitotoxicity at the IHC to SGN synapse. The protective mechanism which LOC fibers use is more disputed, but they may protect Type I SGNs from excitotoxicity by reducing cochlear nerve excitability (Darrow et al., 2007). There is also evidence that LOC neurons maintain a balance between left and right auditory nerve fibers (Guinan, 1996; Darrow et al., 2006), but there is also evidence against this (Larsen and Liberman, 2010).

In addition to its protective role in hearing, the MOC reflex enhances the auditory system's ability to discriminate salient signals in noise, an effect called "anti-masking". For example, activation of the contralateral reflex enhances auditory nerve fiber responses to tone bursts (Kawase and Liberman, 1993) and can improve the detection of speech in noise (Kumar and Vanaja, 2004; Mishra and Lutman, 2014). Indeed, the inclusion of MOC mediated suppression improves speech recognition when added to computational models (Messing et al., 2009; Brown et al., 2010) and enhances sound coding for binaural cochlear implants (Lopez-poveda et al., 2016). In contrast, de Boer et al. (2012) found that reflex activation decreases the detection of speech in noise and proposed that anti-masking may instead depend on attention or experience dependent activation of MOC fibers. While these studies suggest that efferent activation can aid the detection of sound in noise under certain experimental conditions, their role in aiding speech detection is unclear.

Neuroanatomical and physiological evidence suggests that auditory efferents are modulated by cognitive tasks, such as selective attention to auditory or visual stimuli (Delano et al., 2007; Smith et al., 2012; Terreros and Delano, 2015; Walsh et al., 2015). The magnitude and effect of efferent modulation is dependent on the task being assayed, suggesting multiple cortico-olivocochlear pathways (Terreros and Delano, 2015). The MOC system in particular is likely utilized as a top-down frequency filter and receives direct descending input from IC and auditory cortex, and from many of their targets. In chinchillas, auditory cortex stimulation modulates cochlear sensitivity (Dragicevic et al., 2015), functionally demonstrating that descending cortical pathways influence MOC system strength.

In addition to adult physiological functions, efferents are essential for normal auditory system development and maintenance (Frank and Goodrich, 2018). Lesioning of the olivocochlear bundle in neonatal animals leads to broad auditory nerve fiber tuning, suggesting efferents are critical in the early development of afferent responses (Walsh et al., 1998). Additionally, MOC efferents transiently contact IHCs early in development and this projection is lost after hearing onset (Simmons, 2002). Similar to mature OHC contacts, these transient inputs are likely inhibitory (Glowatzki, 2000; Katz et al., 2004) and may play a homeostatic role in maintaining the fine tuning of afferent responses and downstream auditory system tonotopy during early development (Clause et al., 2014). Genetic or surgical disruption of olivocochlear efferents results in accelerated age-related hearing loss and neuropathies indicative of hidden hearing loss (Maison et al., 2013; Chumak et al., 2016). For this reason, genetic and functional assays which gauge for

abnormalities in efferent function may be important for predicting early onset age-related hearing loss.

1.9 Efferent response to sound depends on underlying circuitry and physiology

While auditory efferents play an assorted array of roles in hearing, no single function is obligatory, as efferents are not required for the basic operation of adult hair cells or sound transduction (Robertson, 2009). Evolutionarily, they appeared alongside hair cells, and their most ancient functions are protection from overstimulation and improvement of signal detection in acoustically complex environments (Köppl, 2011). In mammals, the diversification and specialization of these functions is a testament to the versatility afforded by their ability to modulate cochlear output—and depends on the functional properties of the neurons and circuitry involved in each task. In the context of the MOC system, which ultimately inhibits the cochlear amplifier, neurocircuitry underlying any functional role can be broadly associated with ascending or descending pathways which modulate or drive MOC neurons. This circuitry determines the intensity, frequency, and time course of their activity. Therefore, in order to fully understand their normal function in response to sound or descending commands, it is first important to understand the intrinsic properties of MOC neurons and their presynaptic inputs. These properties are currently unknown.

1.10 Overview of dissertation

The present work is directed toward elucidating the central pathways of MOC system circuity, particularly their inputs, to reveal mechanisms underlying their normal function. To identify cholinergic MOC neurons in acute brain sections for use with whole-cell electrophysiology, a transgenic mouse-line expressing a fluorophore under the choline acetyltransferase promotor is characterized in Section 4.1, and utilized throughout Chapter IV.

Section 4.4 provides direct evidence that T-stellate cells of the VCN are indeed an excitatory interneuron of the MOC reflex, overcoming previous limitations by utilizing a novel intersectional adeno-associated virus (AAV) approach. T-stellate cell axons that project to the midbrain were retrogradely infected with AAV expressing Cre-recombinase, and somatically infected with virus expressing Cre-dependent channelrhodopsin (ChR2), enabling a new method of manipulating a clinically significant reflex in regard to acoustic trauma. The Appendix describes the characterization of VCN neurons in a transgenic line that may be used as an alternative approach to manipulating T-stellate cells, albeit with less specificity than the AAV approach in Section 4.4.

Sections 4.2 through 4.8 characterize the intrinsic and synaptic properties of MOC neurons and their inputs. The intrinsic electrophysiological properties of MOC neurons were found to be remarkably homogenous, and seem well suited to encoding stimulus intensity in a continuous fashion. The IC and VCN were targeted with a ChR2 expressing

AAV to investigate pre- and post-synaptic responses onto MOC neurons from nucleus-specific inputs. Each type of input showed distinct, opposite forms of short-term plasticity. Conductance clamp experiments in Section 4.9 and 4.10 demonstrate that this variation in presynaptic plasticity enables firing of MOC neurons over a wide dynamic range by utilizing their intrinsic properties, and the significance of these results are discussed with respect to the roles that efferents perform in hearing.

CHAPTER II: DISTINCT FORMS OF SYNAPTIC PLASTICITY DURING ASCENDING VERSUS DESCENDING CONTROL OF MEDIAL OLIVOCOCHLEAR NEURONS

Gabriel E. Romero[1] and Laurence O. Trussell[2]

[1]Physiology and Pharmacology Graduate Program, [2]Oregon Hearing Research Center and Vollum Institute, Oregon Health and Science University. Portland, Oregon 97219, USA.

Author Contributions: G.E.R. designed, performed, and analyzed experiments and wrote the manuscript. L.O.T. designed, and analyzed experiments and wrote the manuscript.

2.1 Abstract

Activity in each brain region is shaped by the convergence of ascending and descending axonal pathways, and the balance and characteristics of these determine neural output. The medial olivocochlear (MOC) efferent system is part of a reflex arc that critically controls auditory sensitivity. Multiple central pathways contact MOC neurons, raising the question of how a reflex arc could be engaged by diverse inputs. We examined functional properties of synapses onto brainstem MOC neurons from ascending (ventral cochlear nucleus, VCN), and descending (inferior colliculus, IC) sources in mice using an optogenetic approach. We found that these pathways exhibited opposing forms of short-term plasticity, with VCN input showing depression and IC input showing marked facilitation. By using a conductance clamp approach, we found that combinations of facilitating and depressing inputs enabled firing of MOC neurons over a surprisingly wide dynamic range, suggesting an essential role for descending signaling to a brainstem nucleus.

2.2 Introduction

The cochlea is the peripheral organ of hearing. As such, it communicates with the central nervous system by its centrally-projecting afferent fibers. However, the cochlea also receives input from a population of cochlear efferent fibers that originate in the brainstem. The medial olivocochlear (MOC) system provides many of these efferent fibers, and may serve to protect the cochlea from acoustic trauma (Rajan, 1988; Kujawa and Liberman, 1997; Darrow et al., 2007) and to dynamically enhance the detection of salient sound in diverse sensory environments (Winslow and Sachs, 1987a; Kawase and Liberman, 1993) by controlling cochlear gain in a frequency and intensity specific manner. MOC efferent fibers arise from cholinergic neurons whose somata primarily reside in the ventral nucleus of the trapezoid body (VNTB) of the superior olivary complex (SOC) (Warr, 1975b), and project to outer hair cells in the cochlea (Guinan et al., 1983, 1984; Wilson et al., 1991), and this peripheral control by efferents has been extensively studied (Guinan, 2010, 2018). MOC fibers respond to sound and form a negative feedback system, and is thus described as a reflex providing frequency-specific feedback to the cochlea (Liberman and Brown, 1986; Winslow and Sachs, 1987b; Brown, 2016). This feedback is mediated by acetylcholine released from terminals of MOC fibers, thereby inhibiting outer hair cell motility and decreasing cochlear sensitivity (Wiederhold and Kiang, 1970).

In contrast to this detailed understanding of peripheral efferent mechanisms, the electrophysiological properties of the efferent neurons and their control by central pathways remain unclear, and indeed it is not known even to what extent these neurons

function as a reflex arc or as mediators of descending control by higher brain regions. For example, excitatory synaptic inputs that modulate and control MOC neuron function are made both by ascending input from the cochlear nucleus (termed here the 'reflex pathway'), and by descending input from areas that include brainstem, inferior colliculus (IC), and auditory cortex (Thompson and Thompson, 1993; Vetter et al., 1993; Mulders and Robertson, 2002). The reflex MOC pathway receives ascending auditory input from principal neurons in the ventral cochlear nucleus (VCN), possibly by T-stellate cells (Thompson and Thompson, 1991; De Venecia et al., 2005; Darrow et al., 2012; Brown et al., 2013). While T-stellate cells are anatomically and physiologically well suited to provide auditory information to MOC neurons (Oertel et al., 2011), and receive input from type I spiral ganglion neurons, whose axons form the auditory nerve, in fact no direct evidence shows that these neurons activate MOC neurons. Descending projections from the IC contact MOC neurons (Faye-Lund, 1986; Thompson and Thompson, 1993; Vetter et al., 1993), and are tonotopically arranged, as low-frequency fibers project laterally, and high frequencies increasingly project more medially (Caicedo and Herbert, 1993; Suthakar and Ryugo, 2017). Descending input may utilize the MOC system to suppress cochlear input during non-auditory tasks (Delano et al., 2007; Wittekindt et al., 2014), and is well positioned to aid sound detection in noise by contextually inhibiting background frequency spectra (Farhadi et al., 2021). However, again direct evidence for the significance of such descending control is lacking, and in particular whether such inputs can drive the efferent system, or merely modify the control mediated by the reflex pathway.

We have investigated the physiological properties of MOC neurons, testing the relative efficacy of synaptic inputs made by reflex vs descending pathways. MOC efferent neurons were labeled for targeted patch-clamp recording in brain slices from 30- to 48-day-old ChAT-IRES-Cre mice, and properties of ascending and descending synaptic inputs onto these neurons from VCN and IC were analyzed using virally-driven optogenetic excitation. By making recordings from identified neurons in mature mice we found that MOC neurons are exceptionally homogeneous in their electrophysiological properties, and are well suited to encoding stimulus intensity and duration with sustained firing at constant rates. Synaptic inputs to MOC neurons from the VCN and IC are glutamatergic, and both transmit using fast-gating Ca^{2+}-permeable α-amino-3-hydroxy-5-methyl-4-isoxazolepropionic acid (AMPA) receptors. Using a novel intersectional adeno-associated virus (AAV) approach that enabled optical excitation of only T-stellate cells in the VCN, we were able to provide direct evidence that T-stellate cells are an excitatory interneuron involved in MOC reflex circuitry. However, comparing the short-term synaptic plasticity of VCN and IC inputs, we discovered that at the same stimulus rates, VCN input exhibited rapid short-term depression, while IC input exhibited augmentation, increasing several-fold in synaptic strength. Conductance-clamp experiments, in which these inputs were simulated with realistic patterns of activity, showed that descending control of hair cell activity may be a potent means for engaging the full dynamic range of activity of MOC neurons, thus permitting broad control of cochlear sensitivity.

CHAPTER III: MATERIALS AND METHODS

3.1 Animals

Transgenic mice of both sexes expressing Cre recombinase under the endogenous choline acetyltransferase promoter (ChAT-IRES-Cre, Jackson Labs 006410) (Rossi et al., 2011) were crossed to a tdTomato reporter line (Ai9(RCL-tdT), Jackson Labs 007909) to generate mice expressing tdTomato in cholinergic neurons (referred to as ChAT-Cre/tdTomato). A small fraction of ChAT-Cre/tdTomato mice exhibit ectopic expression of Cre recombinase, which labels vasculature and astrocytes (https://www.jax.org/strain/006410). When ectopic expression was observed, the slices were not used for experimental data. Mouse lines were maintained in an animal facility managed by the Department of Comparative Medicine at Oregon Health and Science University. All procedures were approved by the Oregon Health and Science University's Institutional Animal Care and Use Committee and met the recommendations of the Society for Neuroscience.

3.2 Immunohistochemistry and imaging

Mice were deeply anesthetized with isoflurane and then perfused through the heart with 0.1 M phosphate buffered saline (PBS), pH 7.4, 33 °C, followed by ice-cold 4% paraformaldehyde in 0.1 M PBS using a peristaltic pump. Brains were surgically extracted and incubated with 4% paraformaldehyde in 0.1 M PBS overnight at 4°C.

Brains were washed in 0.1 M PBS three times, 10 minutes per wash, and then 50-µm sections were made on a vibratome (Leica, VT1000S) and saved as floating sections in 0.1 M PBS. To visualize cells that were filled with biocytin during whole-cell recording, 300-µM acute brain slices were fixed with 4% paraformaldehyde in 0.1 M PBS overnight at 4°C. Sections used for antibody labeling were permeabilized and blocked in 2% bovine serum albumin, 2% fish gelatin, 0.2% Triton X-100 in 0.1 M PBS for two hours at room temperature on a 2-D rocker. Sections were then incubated in primary antibodies for two days at 4°C on a 2-D rocker. Sections were washed in 0.1 M PBS three times, 10 minutes per wash, and then incubated in secondary antibodies and streptavidin-conjugated fluorophores for two days at 4°C on a 2-D rocker. Sections were washed in 0.1 M PBS three times, 10 minutes each wash, followed by incubation in 4% paraformaldehyde in 0.1 M PBS for 30 minutes. Some brain sections with high fluorophore expression were not enhanced with antibody labeling to reduce background. All sections were mounted on microscope slides and coverslipped with Fluoromount-G (SouthernBiotech) mounting medium, then sealed with clear nail polish. All images of histological sections were acquired on a Zeiss LSM780 confocal microscope system. Images were processed for contrast, brightness and gamma using Fiji (Schindelin et al., 2012).

3.3 Acute brain slice preparation

Mice were deeply anesthetized with isoflurane and decapitated. The brain was rapidly extracted while submerged in warm (40°C) artificial cerebral spinal fluid (aCSF) containing (in mM): 130 NaCl, 2.1 KCl, 1.2 KH_2PO_4, 3 Na-HEPES, 11 glucose, 20 $NaHCO_3$, 1 $MgSO_4$, 1.7 $CaCl_2$, bubbled with 5% CO_2/95% O_2. Parasagittal and coronal

sections of brain containing the superior olive, cochlear nucleus, or inferior colliculus were cut at 300 µm with a vibratome (VT1200S, Leica, or 7000smz-2, Campden) in warm aCSF. Throughout sectioning, brain slices were collected and stored in aCSF at 31°C. When sectioning was completed slices were incubated an additional 30 minutes at 31°C, followed by storage at room temperature, ~23°C.

3.4 Electrophysiology

Acute brain slices were transferred to a recording chamber and submerged in aCSF. Slices were anchored to the chamber using a platinum harp with nylon threads and placed on a fixed stage microscope (Axioskop 2 FS Plus, Zeiss). The recording chamber was perfused with aCSF at 3 ml/minute, and maintained at 31-33°C with an in-line heater (TC-344A, Warner Instrument Corp). Neurons in each slice were viewed using full-field fluorescence with a white-light LED attached to the epifluorescence port of the microscope that was passed through a tdTomato filter-set with a 40X water-immersion objective (Zeiss), and a digital camera (Retiga ELECTRO, QImaging). In slices from ChAT-Cre/tdTomato mice, MOC neurons were identified in the VNTB by their tdTomato fluorescence and morphology. Borosilicate glass capillaries (OD 1.5 mm, World Precision Instruments) were pulled on a P-97 Flaming/Brown micropipette puller (Sutter) to a tip resistance of 1-5 MΩ. All whole-cell current-clamp experiments were conducted with an internal pipette solution containing (in mM): 113 K-gluconate, 2.75 $MgCl_2$, 1.75 $MgSO_4$, 9 HEPES, 0.1 EGTA, 14 tris-phosphocreatine, 0.3 tris-GTP, 4 Na_2-ATP, pH adjusted to 7.2 with KOH, and osmolality adjusted to 290 mOsm with sucrose. Whole-cell voltage-clamp experiments were conducted using a K-gluconate-based pipette

solution, or a cesium-based pipette solution (in mM): 103 CsCl, 10 TEA-Cl, 3.5 QX-314-Cl, 2.75 $MgCl_2$, 1.74 $MgSO_4$, 9 HEPES, 0.1 EGTA, 0.1 spermine, 14 tris-phosphocreatine, 0.3 tris-GTP, 4 Na_2-ATP, with pH adjusted to 7.2 with CsOH, and osmolality adjusted to 290 mOsm with sucrose. All IV-relation experiments used a cesium-based pipette solution. Polyamine-free cesium-based pipette solutions omitted spermine. Reported voltages are corrected for their liquid junction potential: -12.4 mV for K-gluconate based pipette solution and -2.8 mV for cesium-based pipette solution. Loose-patch recordings were conducted with aCSF as the pipette solution. In some experiments, 0.1% biocytin (B1592, Thermo Fisher Scientific) was added to the pipette solution for post-hoc identification of MOC neurons. Whole-cell recordings were amplified (5X gain), low-pass filtered (14 kHz Bessel, Multiclamp 700B, Molecular Devices) and digitized using pClamp software (50-80 kHz, Digidata 1440A, Molecular Devices). Series resistance compensation was set to 60% correction and prediction with a bandwidth of 1.02 kHz. The majority of pipettes used for voltage clamp were wrapped with Parafilm M (Bemis) to reduce pipette capacitance. Cells were voltage-clamped at -62.8 mV unless noted otherwise. The average series resistance (R_s) when patched onto a neuron was 14.5 ± 0.9 MΩ. 1-mM glutamate in aCSF was puffed onto cells from a patch-pipette attached to a Picospritzer II (Parker). The puff pressure was adjusted between 5-10 psi, and 2-15 msec duration to achieve glutamate-evoked currents. Example current traces are baselined to zero pA unless noted otherwise. ChR2 was activated using 2-ms flashes of light through a GFP filter set from a 470 nm LED attached to the epifluorescence port of the microscope. Light stimulation was made through a 40X water immersion objective (Zeiss). At some synapses, ChR2 stimulation can exhibit artificial

synaptic depression (Jackman et al., 2014). To confirm that light-evoked short-term plasticity observed from activation of MOC neuron inputs were not an artifact of ChR2 stimulation at presynaptic boutons (i.e. action potential broadening, increasing the probability of vesicle release), light stimulation was compared over input axons and MOC neuron somata (Figure 4.7—Supplemental Figure 1). In sagittal sections, moving the objective lens away from the recorded neuron and toward the IC in 230 µm steps delayed the onset of light-evoked EPSCs. No EPSC could be evoked when light stimulation was directly ventral to the recorded neuron where there was an absence of brain tissue, confirming that light stimulation was confined to the location of the objective lens. A plot of change in EPSC delay over camera position was best fit with a linear equation and the axon velocity was calculated to be 0.571 meters per second (Figure 4.7—Supplemental Figure 1C). Similar short-term plasticity was observed with both axonal and somatic stimulation (Figure 4.7—Supplemental Figure 1D).

3.5 Miniature EPSC analysis

Miniature EPSCs were recorded in the presence of 1 µM tetrodotoxin (TTX) to block spontaneous spike-driven events, 0.5 µM strychnine and 10 µM SR95531 to block inhibitory receptors, and 10 µM MK-801 to block NMDA receptors. Spontaneous miniature events were detected using a template search function in AxoGraph (1.7.4) from continuously collected data that was stable for more than 3 min. Events were captured and aligned by their onset, and then the average amplitude, time course, and inter-event interval was calculated. Events that appeared artificial or contained multiple

EPSCs were rejected by eye. The decay of average mEPSC data was analyzed in Igor Pro 8 (WaveMetrics) and fit with a double exponential equation:

$$I(t) = A_{fast} \exp\left(\frac{-t}{\tau_{fast}}\right) + A_{slow} \exp\left(\frac{-t}{\tau_{slow}}\right),$$

where $I(t)$ is the current as a function of time, τ_{fast} and τ_{slow} reveal fast and slow decay time constants, and A_{fast} and A_{slow} their relative amplitudes.

3.6 Conductance clamp

To accurately record membrane voltage while simultaneously injecting conductance waveforms, individual MOC neurons were patched simultaneously with two recording electrodes in whole-cell configuration, both containing K-gluconate based pipette solution (Figure 3.1). One electrode served as a voltage follower while the other injected current, thereby avoiding the possibility of distortion of fast waveforms by voltage drop across the series resistance or of capacity transients. Conductance clamp experiments were recorded in the presence of aCSF containing 0.5 µM strychnine, 10 µM SR95531, 10 µM MK-801 and 5 µM NBQX to block all major inhibitory and excitatory inputs. Simulated excitatory postsynaptic conductance waveforms (EPSGs) were injected using an analog conductance injection circuit, Synaptic Module 1 (SM-1) (Cambridge Conductance), driven by a digital computer. The SM-1 unit was set to rectifying mode and E_{rev} was set to +10 mV, to simulate MOC neuron CP-AMPARs (Fig. 3F and 5E).

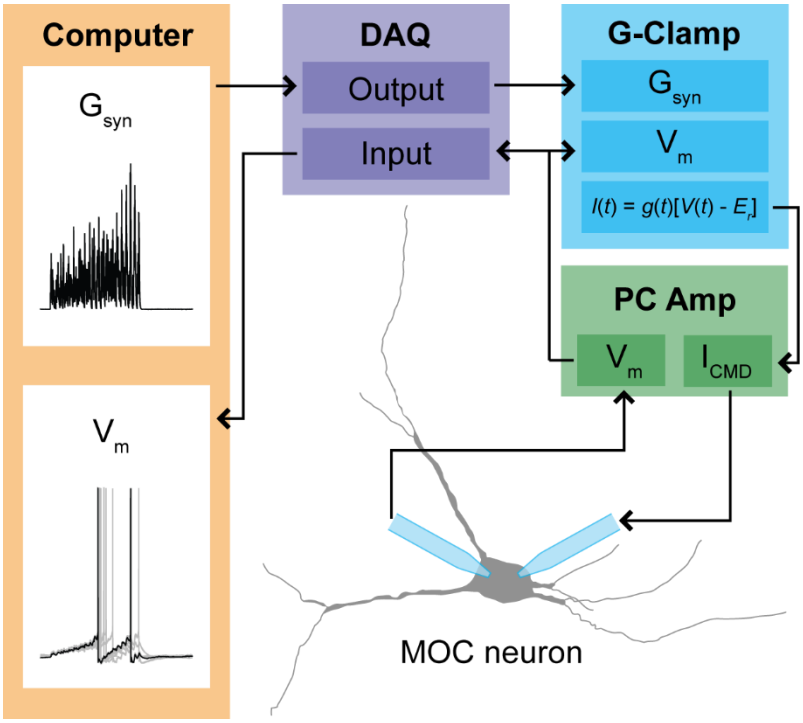

Figure 3.1: Flowchart of conductance clamp configuration. Computer generated conductance waveforms (G_{syn}) were sent to a data acquisition (DAQ) instrument, which was connected to a rectifying G_{syn}-command input on an analog conductance-clamp (G-Clamp) amplifier. MOC neurons were patched simultaneously with two patch pipettes connected to a patch-clamp amplifier (PC Amp). One electrode served as a membrane voltage (V_m) follower while the other injected current. In real-time, the conductance input to the G-Clamp amplifier instantaneously reacted to the membrane potential, producing a current, following the equation: $I_{CMD}(t) = G_{syn}(t)[V_m(t) - E_r]$. The membrane potential signal was sent to the DAQ instrument, and was digitally recorded by a computer.

Conductance waveforms were created using Igor Pro 8 and modeled using physiological data. Whole-cell recordings were made from MOC neurons in the presence of 0.5 nM strychnine, 10 µM SR95531, and 10 µM MK-801 to isolate AMPAR mediated EPSCs. ChR2-positive IC or VCN input was minimally stimulated (~50% chance of evoking an EPSC) using a Lambda TLED light source (Sutter) to reveal unitary responses. Unitary responses were measured to have a maximum conductance (G_{max}) of 0.40 ± 0.01 nS for IC inputs (N = 3), and 0.46 ± 0.06 nS for VCN inputs (N = 3). Thus,

simulated unitary EPSGs were set to a G_{max} of 0.40 nS for synapses modeling short term facilitation (IC input) or 0.46 nS for those modeling short term depression (VCN input) (Fig. 8 and 9). The unitary EPSG waveform:

$$EPSG(t) = (1 - e^{\frac{-t}{\tau_{rise}}}) \times (e^{\frac{-t}{\tau_{decay}}}),$$

was based on a fit to averaged EPSCs from IC and VCN, with τ_{rise} = 0.27 ms, and τ_{decay} = 1.9 ms. Timing and frequency of EPSGs were convolved to action potential timing from T-stellate cells in response to repeated 500-ms current injections, and each repetition (trial) was considered an input (Figures 4.8A and 4.9A). T-stellate cells were identified by virally mediated retrograde labeling (AAVrg-pmSyn1-EBFP-Cre) (Figure 4.4) from the contralateral IC in Ai9(RCL-tdT) mice. For each individual input, short term plasticity was simulated in a frequency invariant manner by weighting G_{max} of unitary EPSGs according to exponential fits of physiological data (Fig. 7D). For short term facilitation, $EPSG_0 = G_{max}$, and,

$$EPSG_n = G_{\max}(Fac_{max} + Ae^{\frac{-(n-n_0)}{\tau}}),$$

where Fac_{max} = 2.43, τ = 12.9 and A = -1.42. For short term depression, $EPSG_0 = G_{max}$, and,

$$EPSG_n = G_{max}(Dep_{max} + A_1 e^{\frac{-(n-n_0)}{\tau_1}} + A_2 e^{\frac{-(n-n_0)}{\tau_2}}),$$

where Dep_{max} = 0.309, τ_1 = 0.771, A_1 = 0.443, τ_2 = 4.10, and A_2 = 0.248.

3.7 Stereotactic injections

Glass capillaries (WireTrol II, Drummond Scientific) were pulled on a P-97 Flaming/Brown micropipette puller (Sutter) and beveled to 45-degree angle with a tip diameter of 30-40 µm using a diamond lapping disc (0.5 µm grit, 3M). Mice (P22-24) were anesthetized with isoflurane (5% induction, 1.5-2% maintenance) and secured in a small stereotaxic frame (David Kopf). While mice were under isoflurane anesthesia, viral injections were made with a single-axis manipulator (MO-10, Narishige) and pipette vice (Ronal) attached to a triple axis motorized manipulator (IVM Triple, Scientifica). After application of 10% povidone iodine, the scalp was cut, and the head was leveled using bregma and lambda. The lateral-medial axis was leveled by focusing a 10X objective 2-mm lateral from lambda to be in the same focal plane on the left and right skull. The location of IC was visually detected after removing a 1-mm^2 unilateral section of occipital bone directly caudal to the lambdoid suture and was pressure injected at a depth of 1 mm. After removing a 1 mm caudal by 2 mm lateral unilateral section of occipital bone caudal to the lambdoid suture, the VCN was located by stereotactic coordinates (0.7 mm lateral, 0.95 mm rostral, and 4.0 mm depth) starting from the surface junction point of the IC, cerebellar lobule IV-V and simple lobule, which is often marked by a Y-shaped branch from the transverse sinus. Post-injection, the incision was closed with nylon sutures. Experiments were conducted 1-3 weeks post-surgery.

3.8 Posterior semi-circular canal injections

Our protocol was adapted from Suzuki et al., (2017), who developed a procedure to deliver viral vectors to the cochlea via the posterior semi-circular canal (PSCC) which minimizes auditory system damage. Briefly, mice were anesthetized and secured to a stereotaxic frame in a manner identical to stereotactic injections, and then rotated 90 degrees onto their side. A small post-auricular incision was made and muscle tissue overlying the temporal bone was dissected to reveal the bony wall of the PSCC. A small hole was made in the PSCC using a 26-gauge hypodermic needle (Kendall), and lymphatic fluid was allowed to drain for 5 minutes. The tip of a small polyethylene tube (PE-10) attached to a pipette vice (Ronal) containing cholera toxin subunit B (CTB, 0.5 % in 0.05 M Tris, 0.2 M NaCl, 0.001 M NaEDTA, 0.003 M NaN3, pH 7.5) was placed into the PSCC oriented toward the ampulla, and sealed with fragments of muscle and cyanoacrylate glue (3M Vetbond Tissue Adhesive). One to two microliters of CTB was injected into the PSCC, and the polyethylene tube was left in place for an additional 5 minutes. After removing the polyethylene tube, the hole was plugged with small pieces of muscle and covered with cyanoacrylate glue. The skin was closed with nylon sutures and mice were perfused for histochemistry 1-5 days later.

3.9 Experimental design and statistical analysis

Electrophysiological traces were analyzed with pClamp 10.7 (Molecular Devices) and IGOR Pro 8 (Wavemetrics) using the NeuroMatic 3.0 package (Rothman and Silver, 2018). Miniature events were analyzed with Axograph 1.7.4 (Clements and Bekkers,

1997) and IGOR Pro 8. Averages are represented as mean ± SEM. Statistical analysis was conducted with IGOR Pro 8, and significance between group means were examined using a two-way analysis of variance (ANOVA) test with a *post-hoc* Tukey's test to identify means that significantly differed. Two-tailed Student's *t*-test was used for comparison between two means. The significance threshold was set at $p<.05$ for all statistical tests. Figures were created with IGOR Pro 8 and Adobe Illustrator (CS2).

CHAPTER IV: RESULTS

4.1 Cholinergic auditory efferent neurons are tdTomato-positive in ChAT-Cre/tdTomato mice

The SOC features two groups of cholinergic olivocochlear efferent neurons, lateral olivocochlear (LOC) neurons and MOC neurons (Warr and Guinan, 1979). The somata of MOC neurons reside primarily in the VNTB, whereas LOC neurons are smaller, more numerous, and located in the lateral superior olive (LSO). While MOC neurons exert inhibitory control over outer hair cells in the cochlea, LOC neurons modulate the excitability of the auditory nerve, as they mainly terminate onto dendrites of Type I spiral ganglion neurons near sensory inner hair cells (Liberman, 1980).

In order to visualize cholinergic efferent neurons in the SOC of acute brain slices for whole-cell recording, we crossed a ChAT-IRES-Cre mouse line with a reporter line, Ai9(RCL-tdT), that expressed the fluorophore tdTomato in a Cre recombinase-dependent manner (Torres Cadenas et al., 2019). This cross will be referred to as ChAT-Cre/tdTomato. Neurons positive for tdTomato were visible in the LSO and VNTB of the SOC, and co-labeled with anti-ChAT antibody, confirming they were cholinergic neurons (Figure 4.1A-C). A majority of tdTomato positive neurons in the ipsilateral LSO and contralateral VNTB were retrogradely labeled by injecting cholera toxin subunit B (CTB) into the cochlea, confirming that they were indeed auditory efferent neurons (Figure 4.1D-E). While MOC neurons project primarily to contralateral cochlea, and LOC

neurons project primarily to ipsilateral cochlea, each group contains fibers projecting to both cochleae (Warr, 1975a; Warr and Guinan, 1979; Brown and Levine, 2008). Contralateral to unilateral cochlear CTB injections, 66.1 % of tdTomato positive VNTB neurons were labeled, and in ipsilateral VNTB 28.9 % were labeled (Figure 4.1F).

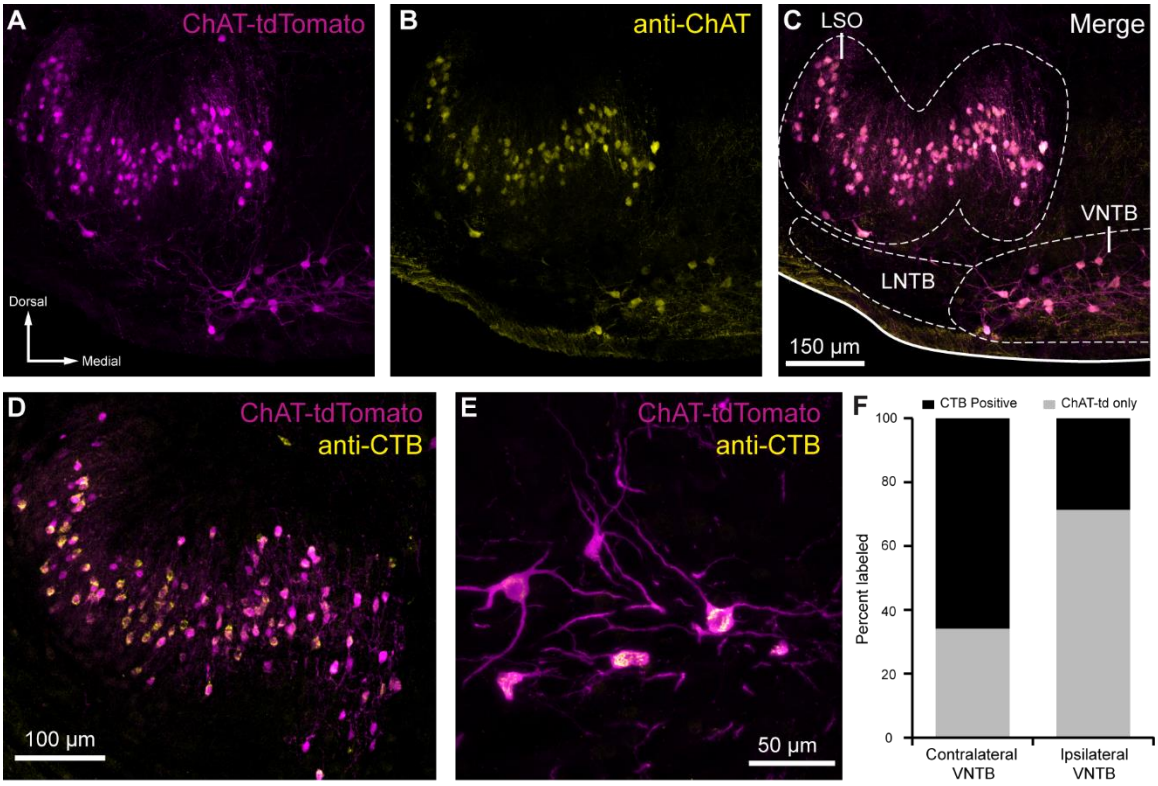

Figure 4.1: Cholinergic auditory efferent neurons identified with the retrograde tracer CTB were tdTomato-positive in ChAT-Cre/tdTomato mice.
(**A**) ChAT-Cre/tdTomato positive neurons in the LSO and VNTB of the superior olivary complex co-label with anti-ChAT antibody (**B**) confirming they are cholinergic neurons (**C**). ChAT-Cre/tdTomato positive neurons in the ipsilateral LSO (**D**) and contralateral VNTB (**E**) were retrogradely labeled by cochlear CTB injections. (**F**) Contralateral to cochlear CTB injections, 66.1 % of ChAT-Cre/tdTomato positive VNTB neurons were labeled. In ipsilateral VNTB, 28.9 % of ChAT-Cre/tdTomato positive neurons were labeled (*N* = 3 mice, 205 cells). Abbreviations: lateral nucleus of the trapezoid body (LNTB)

4.2 Medial olivocochlear neurons accurately encode stimulus intensity and duration

In vivo recordings have revealed that MOC neurons exhibit little or no spontaneous activity, and respond to sound in a frequency- and intensity-dependent manner (Robertson and Gummer, 1985; Liberman and Brown, 1986). To investigate how intrinsic membrane properties of MOC neurons underlie *in vivo* responses, whole-cell patch-clamp recordings were made from tdTomato positive MOC neurons in the VNTB from acute brain slices of ChAT-Cre/tdTomato mice. We found that the majority of MOC neurons had a resting membrane potential of -80.4 ± 0.8 mV (N = 56), and were silent at rest (only 3/59 neurons were spontaneously active), consistent with the low frequency of spontaneous activity observed *in vivo* (Fex, 1962; Cody and Johnstone, 1982; Robertson, 1984; Robertson and Gummer, 1985). The membrane capacitance (C_m) and resistance (R_m) were 36.5 ± 1.6 pF and 123 ± 9 MΩ (N = 59), respectively. In response to hyperpolarizing current injections, MOC neurons lacked an apparent voltage 'sag', indicating minimal expression of hyperpolarization-activated cyclic nucleotide-gated (HCN) channels (Figure 4.2A). Depolarizing currents near action potential threshold revealed a biphasic after-hyperpolarization waveform following each spike (Figure 4.2A, see arrowhead in +0.5 nA example, observed in 57/59 MOC neurons). In response to increasing amplitude of 500-ms depolarizing current injections, MOC neurons fired action potentials that encoded stimulus current intensity with a remarkably linear increase in spike rate (Figure 4.2A-D). For injections up to 900 pA, MOC neurons (N = 33) responded with linearly increasing spike rates, such that the rate nearly doubled when current injections were doubled in intensity, as reflected by the slope of a linear fit to the mean data (slope = 0.150 Hz/pA) (Figure 4.2C). Many MOC neurons continued to

respond linearly to current injections up to 2-4 nA (Figure 4.2A & D) before entering depolarization block. Throughout the duration of these 500-ms depolarizing current injections, action potentials fired with a generally consistent instantaneous rate (Figure 4.2B & E). The ratio of instantaneous spike-rate during the last five action potentials (i.e., the steady-state frequency) compared to spikes #5-10 (initial frequency) decreased somewhat with increasing current intensity (Figure 4.2E & F); 0.86 ± 0.01 at 200 pA, and 0.69 ± 0.02 at 900 pA (N = 11). However, individual cells linearly encoded current intensity with both their initial and their steady-state instantaneous spike-frequencies (initial slope = 0.255 Hz/pA; steady-state slope = 0.158 Hz/pA) (Figure 4.2F). These results using current steps suggest that MOC neurons are well suited to delivering steady efferent signals to the cochlea in exact proportion to the intensity of their ongoing synaptic input. Therefore, we next explored the properties of synaptic inputs to MOC neurons to determine how this intrinsic firing capacity is utilized under more physiological conditions.

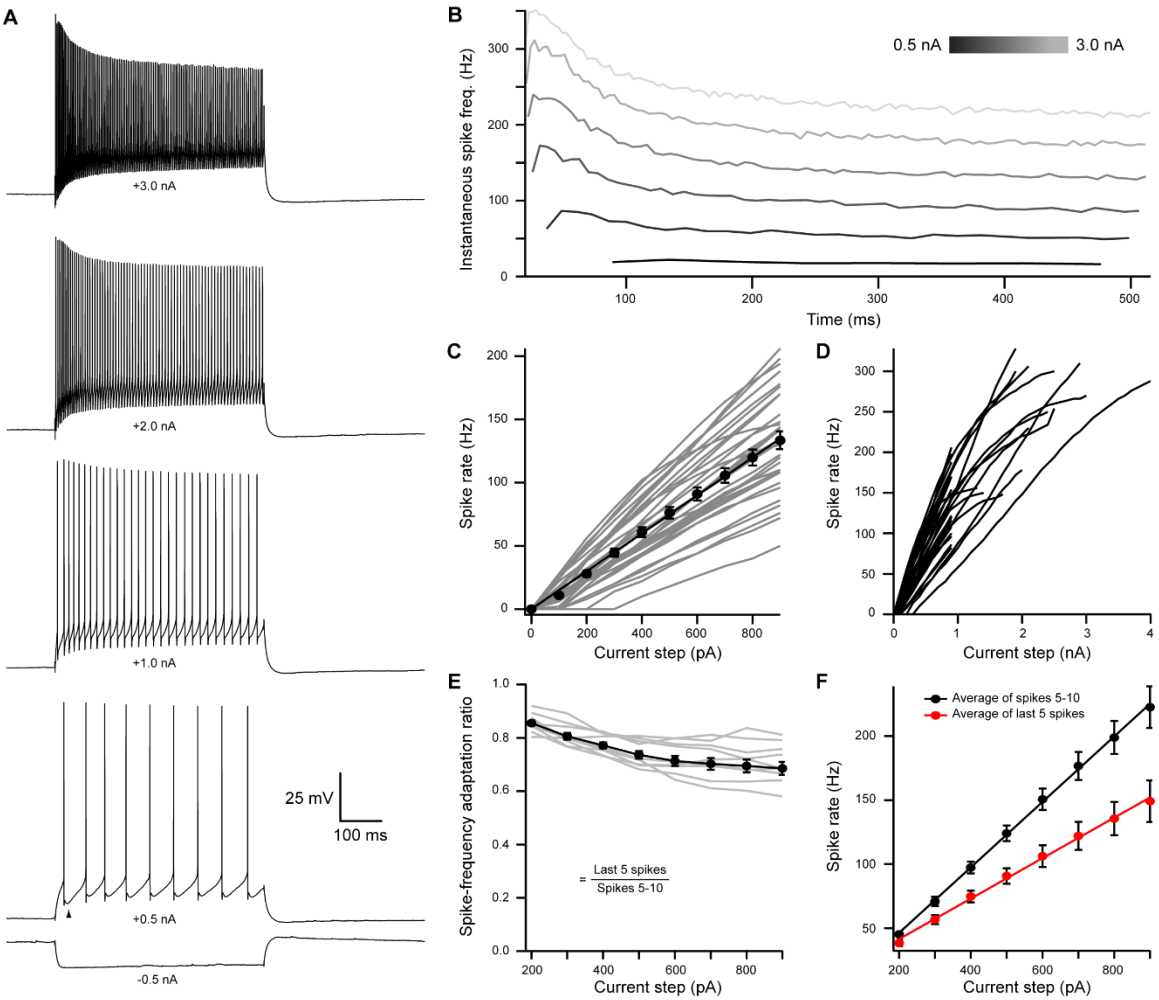

Figure 4.2: Medial olivocochlear neurons accurately encoded stimulus intensity and duration.

(**A**) Whole-cell current-clamp recording example of MOC neuron voltage responses to current injections. Black arrowhead illustrates a double undershoot after-hyperpolarization waveform often observed at action potential threshold-level current injection, and is characteristic of MOC neurons.

(**B**) Example of the instantaneous spike rate over time at increasing current injections from the same neuron in **A**. Current steps begin at 0.5 nA and increase to 3.0 nA in 0.5 nA steps.

(**C**) Mean spike rate during 500 ms current injections of increasing intensity (N = 33). Averages for current injections up to 900 pA demonstrated a linear input-output curve. A linear function was fit to the mean data and the y-intercept was forced to 0 pA ($\boldsymbol{slope} = \mathbf{0.150}\frac{\boldsymbol{Hz}}{\boldsymbol{pA}}$, r^2 = 0.972).

(**D**) Same neurons from **C**, with current injections up to 4 nA.

(Continued on next page)

(**E**) The ratio of spike rate adaptation during the last five spikes compared to spikes #1-5 (N = 11). Analysis was not performed on current steps below 200 pA for panels **E** and **F**, as no MOC neuron met the minimum requirement of fifteen action potentials at those current intensities.
(**F**) The mean spike rate of spikes #5-10, and the mean spike rate of the last five spikes. All error bars are ± SEM (N = 11). Linear functions were fit to the average spike rate of spikes #5-10 ($\boldsymbol{y = 0.255x - 4.69}$, r^2 = 0.999), and the average spike rate of the last five spikes ($\boldsymbol{y = 0.158x - 9.95}$, r^2 = 0.997).

4.3 Light-evoked EPSCs produced by ascending ventral cochlear nucleus input are due to fast-gating, inwardly-rectifying AMPARs

To activate excitatory ascending VCN input onto MOC neurons, the VCN was unilaterally infected with 50 nL of AAV expressing channelrhodopsin (ChR2) fused to the fluorophore Venus (AAV1-CAG-ChR2-Venus-WPRE-SV40) (Figure 4.3—Supplemental Figure 1A). These injections resulted in Venus expression in VCN (Figure 4.3A) and Venus-positive fiber projections to the contralateral VNTB and rostral periolivary regions (RPO) (Figure 4.3B); moreover, Venus positive boutons were observed in close proximity to MOC neuron dendrites and somata in the VNTB (Figure 4.3C). Loose patch recordings were conducted in acute brain slices on Venus positive VCN neurons to determine if potentials mediated by light-activation of virally transduced ChR2 would reach action potential threshold at the level of the soma. Venus positive VCN neurons reliably fired action potentials in response to repetitive 2-ms flashes of blue light (see example, Figure 4.3D). The postsynaptic effects of activation of ChR2 were then examined in whole-cell recordings from MOC neurons made in the presence of 5 µM strychnine and 10 µM SR95531 to block inhibitory receptors, and 10 µM MK-801 to block NMDA receptors. Light-evoked EPSCs were observed in MOC neurons both ipsi- and contralateral to the injection site, and the data were combined. EPSCs were abolished with a selective non-competitive AMPA receptor antagonist, GYKI 53655 (50 µM, N = 3, not shown) indicating that they were glutamatergic and used AMPA receptors. For individual neurons held at -62.8 mV, twenty light-evoked EPSCs were averaged and their decay phases were best fit with either a single (N = 7) or double (N = 5) exponential equation. The decay time constant (τ) of double exponential fits were reported as a fast

decay component (τ_{fast}), and slow decay component (τ_{slow}), see Table 1. For comparison between double and single exponential fits, τ_{fast} and τ_{slow} were converted to a weighted decay time constant:

$$\tau_w = \tau_{fast} * \%A_{fast} + \tau_{slow} * (1 - \%A_{fast}), \text{ where } \%A_{fast} = \frac{A_{fast}}{A_{slow}+A_{fast}}.$$

A_{fast} and A_{slow} are the absolute amplitudes of each component. There was no significant difference between τ from single exponential fits and τ_w. Current voltage relations were constructed by plotting the peak amplitude of EPSCs evoked at holding potentials between -82.8 and +57.2 mV (20-mV steps), and exhibited prominent inward rectification (Figure 4.3E-F). The voltage sensitivity of the peak currents, together with the fast decay of the EPSCs are strongly suggestive of postsynaptic GluA2-lacking, Ca^{2+}-permeable AMPARs (CP-AMPARs) (Mosbacher et al., 1994; Bowie and Mayer, 1995; Donevan and Rogawski, 1995; Geiger et al., 1995).

Table 1. Decay time constants for evoked and miniature EPSCs.

	Double exponential						Single exponential
	τ_{fast} (ms)	τ_{slow} (ms)	A_{fast} (pA)	A_{slow} (pA)	$\%A_{fast}$ (*100)	τ_w (ms)	τ (ms)
VCN input *N* = 12	0.75 ± 0.26 (*7*)	4.11 ± 0.86 (*7*)	-78.63 ± 21.10 (*7*)	-37.98 ± 13.10 (*7*)	70.79 ± 0.25 (*7*)	1.59 ± 0.25 (*7*)	2.22 ± 0.68 (*5*)
T-stellate input *N* = 4	0.62 (*1*)	3.32 (*1*)	-131.60 (*1*)	-54.12 (*1*)	70.86 (*1*)	1.19 (*1*)	1.73 ± 0.57 (*3*)
IC input *N* = 28	0.63 ± 0.09 (*13*)	3.43 ± 0.30 (*13*)	-73.09 ± 16.55 (*13*)	-45.44 ± 9.13 (*13*)	60.64 ± 5.00 (*13*)	1.72 ± 0.22 (*13*)	2.09 ± 0.28 (*15*)
mEPSC *N* = 3	0.17 ± 0.01 (*3*)	1.72 ± 0.43 (*3*)	-47.07 ± 5.36 (*3*)	-5.63 ± 1.37 (*3*)	89.04 ± 3.00 (*3*)	0.32 ± 0.02 (*3*)	N/A

$\tau_w = \tau_{fast} * \%A_{fast} + \tau_{slow} * (1 - \%A_{fast})$, $\%A_{fast} = \frac{A_{fast}}{A_{fast}+A_{slow}}$. Number of cells per data point denoted as (*N*).

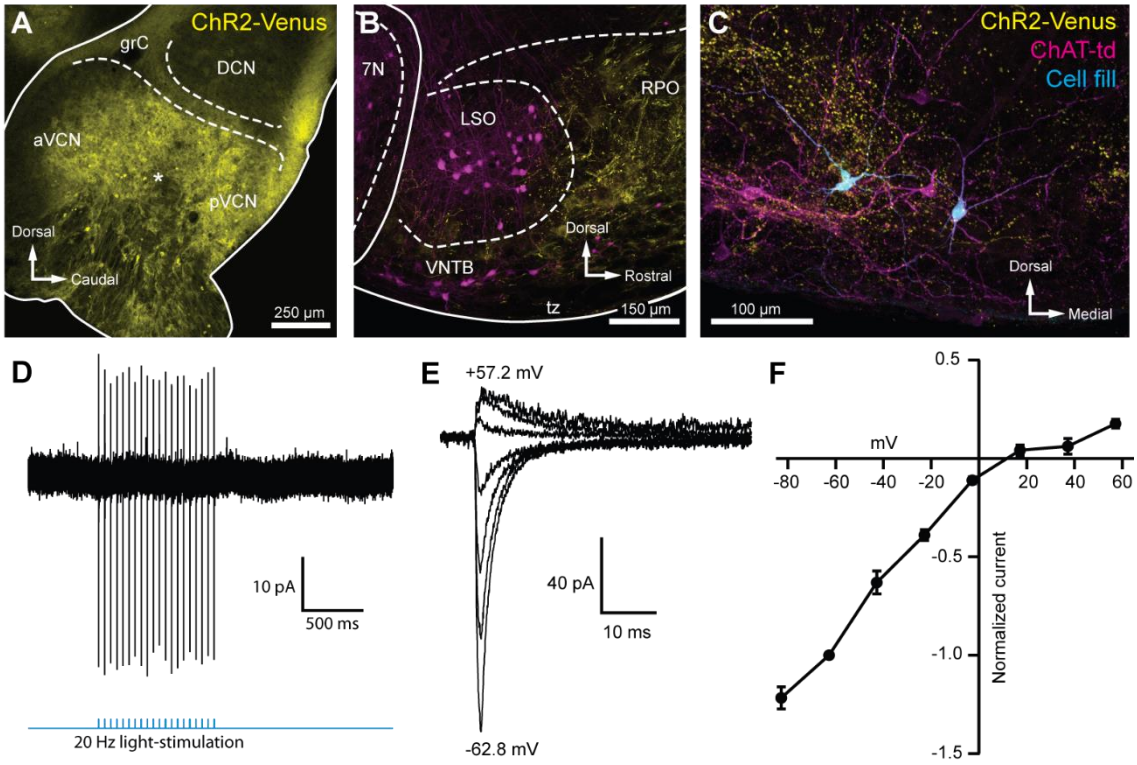

Figure 4.3: Light-evoked EPSCs produced by ascending cochlear nucleus input were due to inwardly rectifying AMPARs.
(**A**) Sagittal micrograph of a ChR2-Venus positive ventral cochlear nucleus (* marks presumed injection site).
(**B**) Micrograph from the same mouse as A, where ChR2-positive fibers are present in the VNTB and RPO near MOC neuron somata.
(**C**) Two MOC neurons in the VNTB that were recorded from in a coronal brain section and filled with biocytin after post-hoc histochemistry.
(**D**) Example loose patch, cell attached recording of a ChR2-Venus positive neuron in the VCN. Neurons positive for ChR2-Venus can reliably fire action-potentials in response to light stimuli.
(**E**) An example of EPSCs evoked during voltage clamp, with holding potentials ranging from -62.8 mV to +57.2 mV in 20 mV steps. Each sweep was baselined to 0 pA and low-pass Bessel filtered at 3000 Hz.
(**F**) I-V relation of normalized cumulative data (N = 3 to 9 per mean). Error bars are ± SEM. Abbreviations: anteroventral cochlear nucleus (AVCN), posteroventral cochlear nucleus (PVCN), dorsal cochlear nucleus (DCN), granule cell layer (grC), facial motor nucleus (7N), rostral periolivary region (RPO).

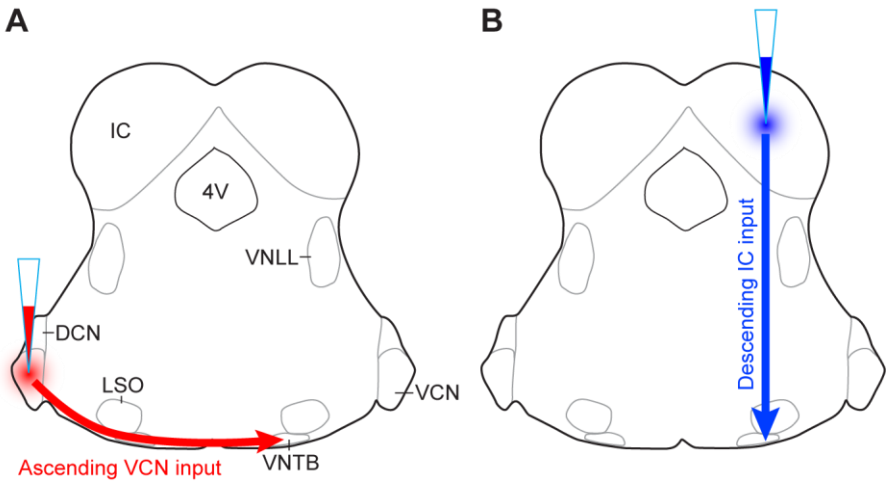

Figure 4.3—Supplemental Figure 1: AAV injection schemes to target ascending or descending inputs to MOC neurons.
Schematics depict a unilateral injection of ChR2-Venus expressing AAV (AAV1-CAG-ChR2-Venus-WPRE-SV40) into (**A**) VCN or (**B**) IC of ChAT-Cre/tdTomato mice.

4.4 Selective activation of T-stellate neurons using an intersectional AAV approach

The results described above indicate that input from VCN-originating axons generate EPSCs in MOC neurons, but do not indicate which subtype of VCN neuron is involved. Given the presence of multiple subtypes of VCN excitatory neurons, and the absence of selective Cre lines for these subtypes (see Appendix), a definitive demonstration of the source of input to MOC neurons is challenging. T-stellate (also called planar multipolar) cells of the VCN are excitatory projection neurons that receive auditory nerve input (Oertel et al., 2011). As a population, they may encode sound intensity and frequency spectrum. T-stellate cells are a major ascending pathway of the auditory system which project widely to many targets, and are the only VCN cell which projects to the IC.

Several reports suggest that T-stellate cells serve as an interneuron in the MOC reflex pathway (Thompson and Thompson, 1991; De Venecia et al., 2005; Darrow et al., 2012), although there is currently no direct evidence for functional connectivity between T-stellate cells and MOC neurons. We developed a scheme to selectively activate T-stellate cells using an intersectional AAV approach in order to perform virally driven optogenetic studies of ascending MOC circuitry (Figure 4.4Ai-ii). An AAV engineered to infect axons in addition to neurons local to the injection site (AAVrg-pmSyn1-EBFP-Cre) (Tervo et al., 2016) was injected into IC of ChAT-Cre/tdTomato mice, causing Cre-dependent tdTomato expression in cells that project to and from IC, including T-stellate cells in the VCN (Figure 4.4Ai & Bii). Prior to AAV infection, no somata were positive

for tdTomato in VCN or IC of ChAT-Cre/tdTomato mice (Figure 4.4Bi, Figure 4.4—Supplemental Figure 1A). One-to-two weeks post IC infection with AAVrg-pmSyn1-EBFP-Cre, tdTomato positive somata were located near the injection site and nuclei that send projections to IC, including contralateral IC (Figure 4.4—Supplemental Figure 1B). A majority of retrogradely labeled VCN somata were located contralateral to the injection site (Figure 4.4Bii), whereas few were seen in ipsilateral VCN (Figure 4.4—Supplemental Figure 1C), reflecting previously described ipsilateral T-stellate cell projections (Adams, 1979; Thompson, 1998).

In recordings from tdTomato positive VCN neurons (N = 13) in AAVrg-pmSyn1-EBFP-Cre infected ChAT-Cre/tdTomato mice, all neurons exhibited responses to current injections that were characteristic of T-stellate cells (see example in Figure 4.4C). Action potentials fired tonically with a sustained rate in response to depolarizing current injections (Figure 4.4D). Hyperpolarizing current injections revealed a rectifying voltage response characteristic of HCN nonselective cation channels (Figure 4.4C). Additionally, membrane resistance (R_m = 147.6 ± 21.5 MΩ) and membrane capacitance (C_m = 32.9 ± 2.6 pF) were typical of T-stellate cells (Wu and Oertel, 1987; Ferragamo et al., 1998; Golding et al., 1999).

A second virus that expressed Cre-dependent ChR2 and enhanced yellow fluorescent protein (EYFP) was then injected into the VCN, enabling ChR2 and EYFP expression only in T-stellate cells that project to contralateral IC (Figure 4.4Aii, Ei-F).

VCN neurons positive for EYFP were also positive for tdTomato (Figure 4.4Ei-F), confirming the selectivity of this intersectional AAV approach. Dual infected VCN neurons projected to known T-stellate cell target nuclei, including contralateral IC, contralateral and ipsilateral VNTB, ipsilateral LSO, and contralateral lateral lemniscus (Figure 4.4—Supplemental Figure 1D-I). During whole-cell voltage-clamp recording, optogenetic activation of T-stellate input evoked EPSCs in contralateral MOC neurons (N = 4, Figure 4.4G) confirming that T-stellate neurons excite post-synaptic MOC efferent neurons. Decay kinetics of T-stellate input to MOC neurons were not significantly different compared to non-specific VCN-input (Table 1), suggesting similar post-synaptic AMPA receptor composition. These results definitively show that at least a subset of IC projecting T-stellate cells provide glutamatergic excitatory input to MOC neurons.

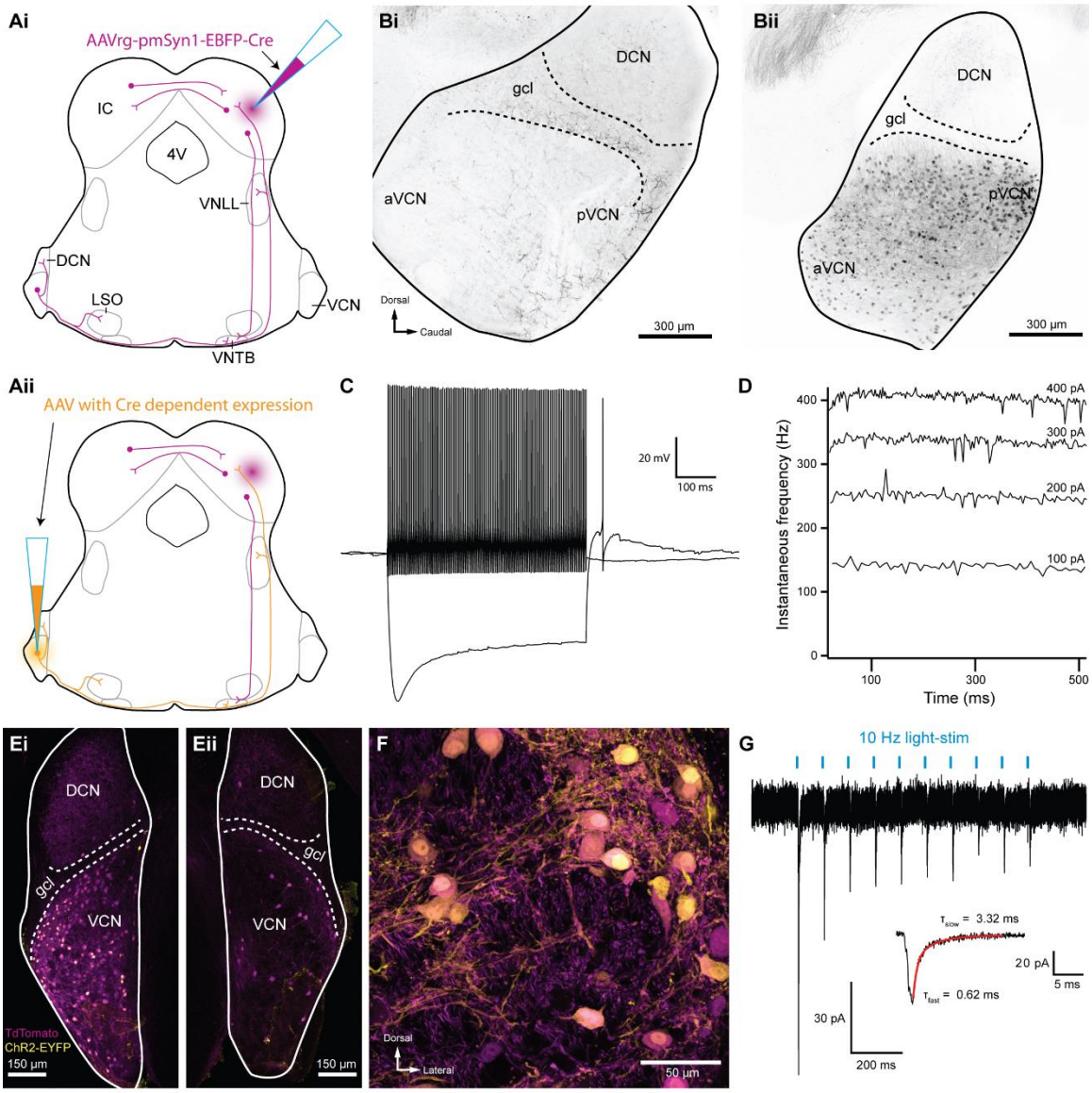

Figure 4.4: Inferior colliculus projecting T-stellate neurons synapsed onto MOC neurons in the ventral nucleus of the trapezoid body.

(**Ai**) Schematic depicting an inferior colliculus injection site of Cre recombinase expressing retrograde-AAV (AAVrg-pmSyn1-EBFP-Cre), and putative retrogradely infected neurons and projections (magenta), including T-stellate cells and descending IC projections to olivocochlear efferents.

(**Aii**) Continuation of Ai, depicting the ventral cochlear nucleus injection site for a second AAV expressing a Cre dependent channelrhodopsin. T-stellate neurons (orange) positive for both AAVs project to the ventral nucleus of the trapezoid body (VNTB), where MOC neuron somata reside.

(Continued on next page)

(**Bi**) Sagittal micrograph of a ChAT-Cre/tdTomato cochlear nucleus. TdTomato positive fibers were visible throughout the nucleus, however, there was a complete lack of tdTomato positive somata in VCN.
(**Bii**) Sagittal micrograph of a ChAT-Cre/tdTomato cochlear nucleus infected with Cre expressing retrograde AAV that was injected into the contralateral to IC. TdTomato positive somata were visible throughout the VCN.
(**C**) Example of a current-clamp whole-cell recording from an AAVrg-pmSyn1-EBFP-Cre/tdTomato positive cell in the VCN. All recordings from tdTomato positive cells in VCN (N = 13) exhibited responses to current injections characteristic of T-stellate cells. Action potentials fired tonically with a sustained rate in response to depolarizing current injections (0.2 nA). Hyperpolarizing current injections (-0.5 nA) revealed a rectifying voltage response.
(**D**) Example plot of instantaneous frequency of action potentials throughout the duration of depolarizing stimuli ranging from 100 to 400 pA. The spike frequency is sustained throughout the duration of the stimulus, which is characteristic of T-stellate neurons in the VCN.
(**Ei**) Coronal micrograph of a cochlear nucleus contralateral to Cre expressing retrograde AAV infection of IC. The VCN contralateral to IC infection was additionally infected with AAV2-EF1a-DIO-hChR2(E123T/T159C)-p2A-EYFP (UNC Vector Core), which expressed EYFP in the cytosol.
(**Eii**) Coronal micrograph of a cochlear nucleus ipsilateral to Cre expressing retrograde AAV infection of IC from the same mouse as Ei. Many somata positive for both tdTomato and EYFP are seen in VCN contralateral to the IC infection, **Ei**, whereas no cells positive for EYFP are seen in VCN ipsilateral to the IC infection, **Eii**.
(**F**) A micrograph of VCN contralateral to Cre expressing retrograde AAV infection of the IC depicting tdTomato and EYFP expression from the same mouse as Ei & Eii.
(**G**) Whole-cell voltage clamp recording from an MOC neuron of a ChAT-Cre/tdTomato mouse contralateral to T-stellate cells expressing ChR2 via the intersectional AAV approach. Light-evoked EPSCs were stimulated with 2 ms pulses of blue light at 10 Hz, and in this example the EPSCs depressed with repetitive stimulation. This trace was created by averaging 20 sweeps of the same protocol from the same MOC neuron. Inset illustrates fast and slow decay time constants (τ) of the first averaged EPSC and was fit with a double exponential function (red).
Abbreviations: inferior colliculus (IC), fourth ventricle (4V), ventral nucleus of the lateral lemniscus (VNLL), dorsal cochlear nucleus (DCN), ventral cochlear nucleus (VCN), anteroventral cochlear nucleus (aVCN), posteroventral cochlear nucleus (pVCN), lateral superior olive (LSO), ventral nucleus of the trapezoid body (VNTB).

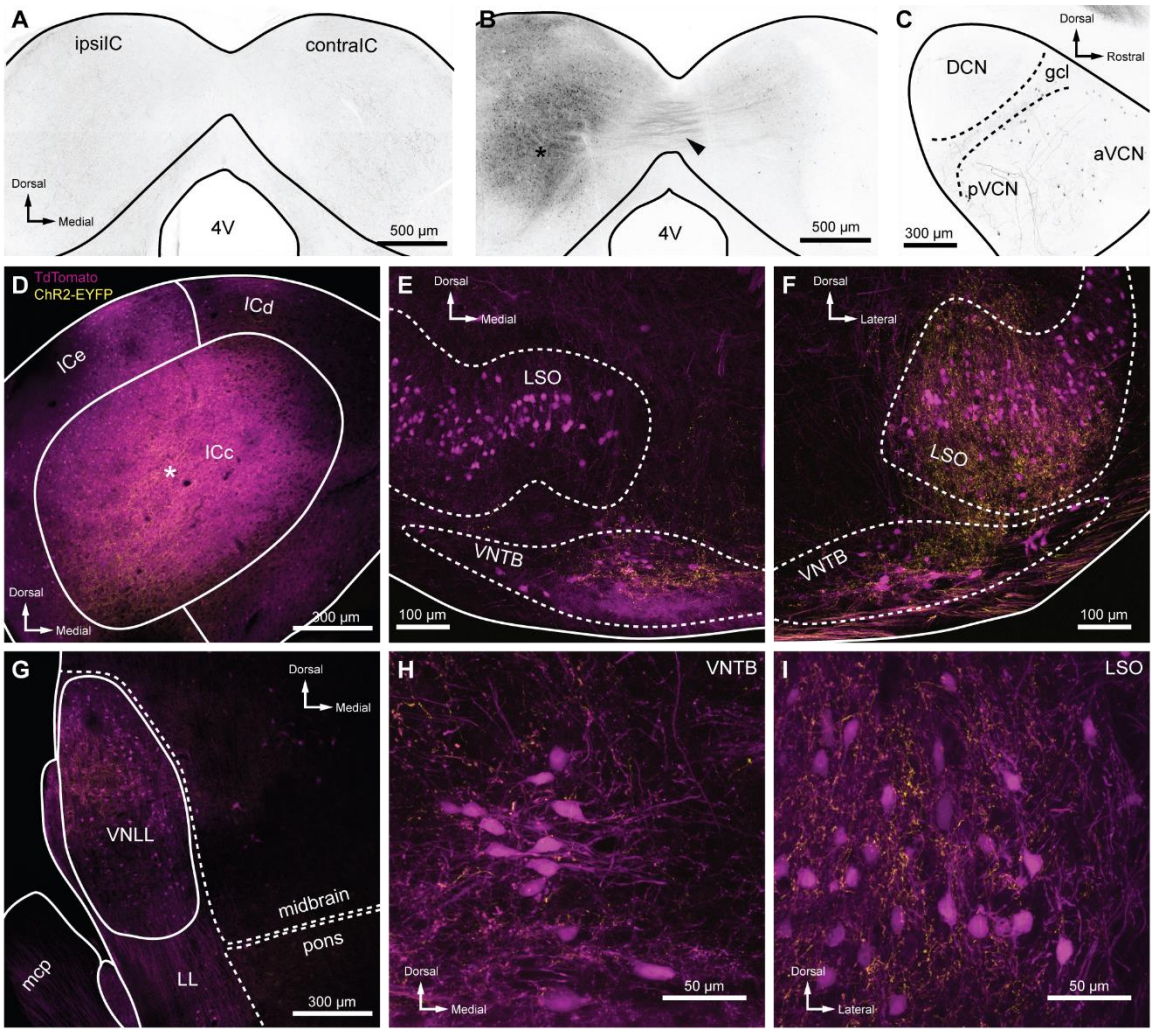

Figure 4.4—Supplemental Figure 1: Intersectional AAV injection micrographs and T-stellate cell targets.

(**A**) The ChAT-Cre line was crossed to an Ai9 reporter to generate mice with tdTomato in Cre positive cells (ChAT-Cre/tdTomato). This coronal micrograph of the IC showed tdTomato expression before AAV infection. TdTomato fluorescence is represented in greyscale.

(**B**) Coronal micrograph of the IC, ipsilateral (ipsilIC) and contralateral (contralIC) to the injection site of retrograde-AAV (AAVrg-pmSyn1-EBFP-Cre, asterisk), which infected local neurons, and neurons that projected to the injection site. TdTomato expressing projections in the commissure of the IC were visible (arrowhead), as were retrogradely labeled cells in IC contralateral to the infection (contraIC).

(**C**) Sagittal micrograph of cochlear nucleus ipsilateral to Cre expressing retrograde-AAV infection of ipsilIC, same mouse as **B**. All micrographs in **D-I** were from coronal sections of a ChAT-Cre/tdTomato mouse infected with AAVrg-pmSyn1-EBFP-Cre in IC, and AAV9-EF1a-DIO-hChR2(H134R)-EYFP in VCN contralateral to IC infection. EYFP is fused to ChR2, enhancing the visualization of T-stellate projections over cytosolic fluorophores. (Continued on next page)

(**D**) Coronal micrograph of IC, where ChAT-Cre/tdTomato positive neurons were seen in close proximity to an AAVrg-pmSyn1-EBFP injection site (asterisk). T-stellate originating ChR2-EYFP positive fibers projecting to the central nucleus of the inferior colliculus (ICc) were also visible (yellow).
(**E**) Micrograph of the superior olivary complex ipsilateral to the IC infection. Cholinergic neurons positive for ChAT-Cre/tdTomato delineate the lateral superior olive (LSO) and ventral nucleus of the trapezoid body (VNTB). TdTomato positive fibers originating from the IC were seen in the ventral VNTB (compare to contralateral VNTB in panel **F**). T-stellate fibers positive for ChR2-EYFP were prominently visible within, and dorsal to, VNTB with little to no expression in LSO.
(**F**) Micrograph of superior olivary complex contralateral to IC infection. T-stellate fibers positive for ChR2-EYFP were prominently visible within LSO and VNTB.
(**G**) Micrograph of lateral lemniscus (LL) ipsilateral to the IC infection. T-stellate fibers were visible within the ventral nucleus of the lateral lemniscus (VNLL). Cells positive for tdTomato were likely due to trans-synaptic Cre expression (Zingg et al., 2017) or ectopic ChAT-Cre expression.
(**H**-**I**) High magnification micrographs of VNTB (H) and LSO (**I**) ipsilateral and contralateral to IC infection, respectively. T-stellate boutons positive for ChR2-EYFP terminated in both nuclei.

4.5 Light evoked EPSCs produced by descending inferior colliculus input are due to fast-gating, inwardly rectifying AMPARs

To activate excitatory descending IC input onto MOC neurons, the IC of ChAT-Cre/tdTomato mice were unilaterally infected with 100 nL of AAV1-CAG-ChR2-Venus-WPRE-SV40 (Petreanu et al., 2009) (Figure 4.3—Supplemental Figure 1B), an anterograde-transported viral construct. One-to-two weeks post-infection, Venus was observed in somata throughout the injected IC (Figure 4.5A). The majority of Venus positive fibers were visible in the ventral portion of the VNTB and RPO in close apposition to MOC neuron somata and dendrites (Figure 4.5B, Figure 4.5—Supplemental Figure 1). Loose patch, cell-attached recordings of Venus positive neurons in the IC were conducted to assess ChR2 expression. IC neurons positive for Venus fired action potentials in response to 2-ms flashes of blue light (see example in Figure 4.5C), confirming that ChR2 currents could reliably elicit action potentials in response to high-frequency light stimuli. Similar to VCN input onto MOC neurons, evoked EPSCs originating from IC input were mediated by inwardly-rectifying AMPARs (Figure 4.5D-E). This suggests that IC and VCN synapses onto MOC neurons both transmit by means of postsynaptic CP-AMPARs.

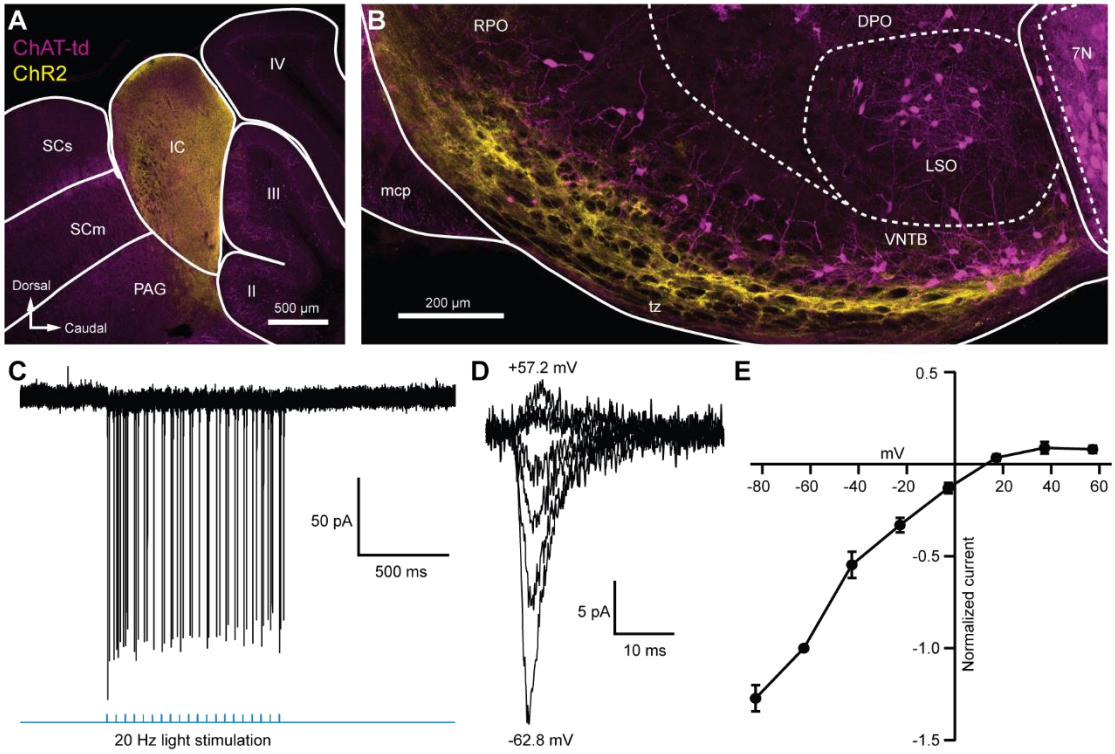

Figure 4.5: Light evoked EPSCs produced by descending inferior colliculus input were due to inwardly rectifying AMPARs.
(**A**) Sagittal micrograph of a ChAT-Cre/tdTomato brain section showing an IC injection site positive for ChR2-Venus.
(**B**) Sagittal micrograph of the superior olivary complex from the same mouse as in **A**. The majority of ChR2 positive fibers were visible in the ventral portion of the VNTB/RPO, near MOC neuron somata.
(**C**) Loose patch, cell attached recording of a ChR2-positive neuron in the IC. ChR2-Venus positive neurons can reliably fire action potentials in response to light stimuli.
(**D**) An example of EPSCs evoked during voltage clamp, with holding potentials ranging from -62.8 mV to +57.2 mV in 20 mV steps.
(**E**) I-V relation reporting normalized cumulative data (N = 4 to 7 per mean, N = 2 at +57.2 mV). Error bars are ± SEM.
Abbreviations: Superior colliculus (sensory, SCs; motor, SCm), periaqueductal gray (PAG), cerebellar lobules (labeled II-IV), pontine gray (PG), rostral periolivary region (RPO), dorsal periolivary region (DPO), middle cerebellar peduncle (mcp), lateral superior olive (LSO), ventral nucleus of the trapezoid body (VNTB), facial motor nucleus (7N).

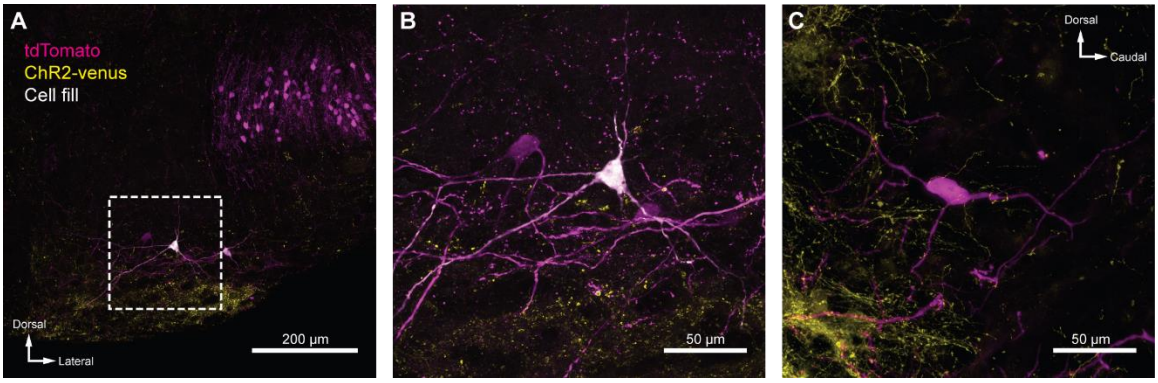

Figure 4.5—Supplemental Figure 1: IC projections to MOC neurons.
(**A**) Coronal micrograph of biocytin-filled MOC neuron in VNTB ipsilateral to ChR2-Venus infected IC.
(**B**) High magnification micrograph of MOC neuron from **A**.
(**C**) High magnification sagittal micrograph of a putative MOC neuron from Figure 5B. While a majority of ChR2-Venus positive fibers were ventral to MOC neurons, many positive fibers were in close apposition to MOC neuron dendrites and somata.

4.6 Inward rectification is due to endogenous polyamine block and Ca^{2+}-permeable AMPARs

GluR2-lacking, or CP-AMPARs, show rapid decay kinetics, and inward rectification due to voltage-dependent block by intracellular polyamines (Bowie and Mayer, 1995; Donevan and Rogawski, 1995). Demonstration of such block by polyamines could support the interpretation that inputs to MOC neurons are indeed GluR2-lacking. We reasoned that removal of endogenous polyamines by dialysis would be most effective near the patch pipette, and comparatively weak in dendrites where excitatory synapses are likely concentrated. Therefore, we applied glutamate by pressure ejection directly to the soma, and tested voltage dependence in recordings in which the patch pipette solution contained or lacked the polyamine spermine (100 μM). In the presence of intracellular spermine, glutamate-evoked currents resulted in an inwardly rectifying current-voltage (I-V) relation (Figure 4.6A-B), similar to light-evoked EPSCs from IC or VCN input (Figures 4.3E-F & 4.4D-E). When recordings were made with a spermine-free solution, the I-V relation was linear (Figure 4.6A-B). At +37.2 mV and +57.2 mV, 57.9 % and 58.9 % of the outward current was blocked by spermine, respectively, suggesting a majority of AMPAR-mediated currents are due to CP-AMPARs.

CP-AMPARs are selectively blocked by IEM 1925 dihydrobromide, which binds to the ion-channel pore in GluA2-lacking receptors more potently than GluA2-containing receptors (Zaitsev et al., 2011; Twomey et al., 2018). CP-AMPAR block by IEM 1925 is both activity and voltage dependent, requiring open-state channels and negative

potentials. Thus, the amount of block is weakest during spontaneous and evoked synaptic events, and is greatest during continuous application of agonist. To maximally inhibit CP-AMPAR mediated currents with IEM 1925, MOC neurons were held at a potential of -82.8 mV in voltage-clamp mode, and 1 mM glutamate was pressure-puffed near MOC neuron somata. After bath application of 25 μM IEM 1925, glutamate-evoked currents were reduced by 55.3 ± 1.6 %, and returned to 81.2 ± 3.0 % of control after wash (N = 3, Figure 4.6C). This percentage of block by IEM 1925 was similar to that of spermine block in our dialysis experiments (Figure 4.6B). The blocking effect of IEM 1925 on glutamate-evoked currents pharmacologically confirmed that MOC neurons express GluA2-lacking CP-AMPARs.

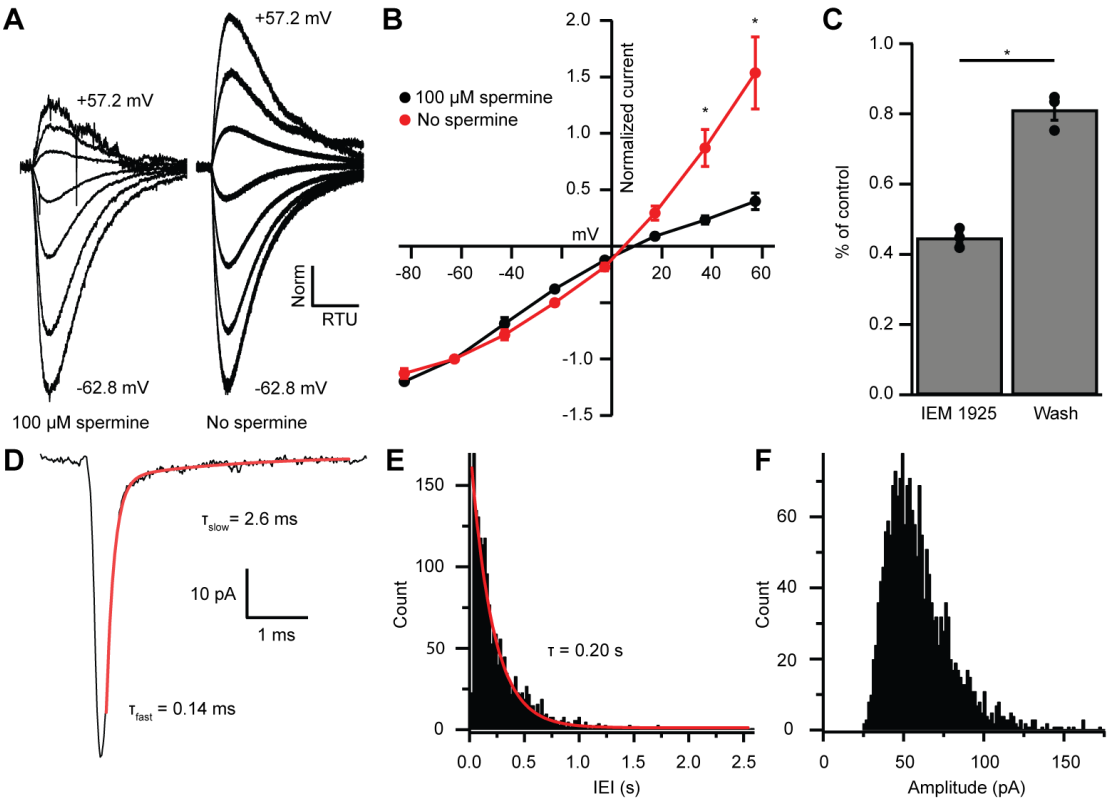

Figure 4.6: EPSC inward rectification was due to endogenous polyamine block and Ca2+-permeable AMPARs.

(**A**) AMPAR mediated currents in MOC neurons evoked by 1 mM pressure-puffed glutamate near the cell soma. The soma of MOC neurons were dialyzed with an internal pipette solution containing 100 µM, or no spermine. In the presence of spermine, glutamate-evoked currents resulted in an inwardly rectifying I-V relation. In the absence of spermine, the rectification was relieved though dialysis, which resulted in a linear I-V relation. Voltage steps ranged from -62.8 mV to +57.2 mV in 20 mV steps. Average of 3 to 10 sweeps per trace. Each sweep was baselined to 0 pA, Bessel filtered at 3000 Hz, and normalized to glutamate-current decays and maximum amplitudes at -62.8 mV.

(**B**) An I-V curve showing the average amplitudes (normalized to -62.8 mV) of glutamate-evoked currents in spermine-free (N = 3) and 100 µM spermine (N = 4) conditions. Error bars are ± SEM. Conditions were significantly different at +37.2 and +57.2 mV ($p<.05$).

(**C**) At -82.8 mV, AMPAR mediated currents were reduced by 55.29 ± 1.60 % with bath application of Ca^{2+}-permeable AMPAR antagonist, IEM 1925 (25 µM). Wash-out of IEM 1925 resulted in inward-currents that recovered to 81.20 ± 2.97 % of control.

(**D**) Average of 582 mEPSCs from one neuron. The fast component (τ_{fast}) was responsible for 93.2 % of the decay amplitude. Fast decay kinetics are indicative of GluA2 lacking, CP-AMPARs.

(**E**) Inter-event-interval (IEI) distribution of mEPSC activity, 0.02 second bins, 1873 events from 3 neurons.

(**F**) Amplitude distribution of mEPSCs, 1.5 pA bins.

4.7 MOC neuron miniature EPSCs are mediated by fast-gating AMPARs

To determine if rapid decay kinetics measured from IC and VCN originating EPSCs were synapse specific, or a fundamental feature of MOC neuron excitatory synaptic events, we conducted an analysis of miniature EPSCs (mEPSCs). AMPA receptor mediated currents were pharmacologically isolated and recorded in the presence of 1 µM TTX to block spontaneous spike-driven events. The decay phase of average miniature events was best fit with a double exponential function, where τ_{fast} was responsible for 89.0 ± 3.0 % of the mEPSC amplitude (see Table 1, and example Figure 4.6D). The average τ_{fast} and τ_{slow} of mEPSCs were 0.17 ± 0.01 ms and 1.72 ± 0.43 ms, respectively (*N* = 3 neurons, 1873 mEPSCs). The inter-event interval (IEI) between mEPSCs ranged from 6.8 ms to 2.6 seconds, and each event was counted and sorted into 20 ms bins (Figure 4.6E). The distribution of binned mEPSC inter-event intervals was best described with a single exponential equation (τ = 0.20 seconds), reflecting that the miniature events were stochastic in nature (Fatt and Katz, 1952). The average and median mEPSC amplitudes were 57.5 ± 0.9 pA and 52.5 pA, respectively, and ranged from 27.2 pA to 146.9 pA (Figure 4.6F). In comparison with light-evoked EPSCs from IC and VCN (Table 1), these results confirmed that the majority of mEPSCs were due to fast-gating AMPARs. Together, supportive of data from light-evoked EPSCs and glutamate-puff evoked currents, these results suggest that fast-gating CP-AMPARs are the major component of excitatory synaptic transmission at MOC neurons.

4.8 Ascending and descending inputs to medial olivocochlear neurons show distinct, opposite forms of short-term plasticity

The AMPARs mediating transmission from VCN and IC were biophysically similar (Table 1). However, input-specific repetitive activation of VCN or IC inputs revealed strikingly opposing forms of short-term plasticity (Figure 4.7). During 20-pulse tetanus stimuli (20 or 50 Hz), light-evoked VCN-originating EPSCs depressed whereas IC-originating EPSCs facilitated (Figure 4.7A-D). Plasticity from either input was observed bilaterally in the VNTB and the data was combined. To quantify change in EPSC amplitude during VCN stimulation, the ratio of the amplitude of the last three EPSCs of the tetanus over the amplitude of the first EPSC was calculated. For IC stimulation, the amplitude of the last three EPSCs of the tetanus was compared to the average amplitude of the first three EPSCs. This 'plasticity index' showed about 70% depression for VCN inputs, with no difference between 20 Hz or 50 Hz activity (0.31 ± 0.02 for 20 Hz, N = 8; 0.29 ± 0.04 for 50 Hz, N = 7, p=.59, Student's t-test, Figure 4.7C). By contrast, inputs from IC showed marked enhancement of the plasticity index during the train, although again with no differences between 20 Hz and 50 Hz (1.82 ± 0.17 for 20 Hz, N = 8; 1.65 ± 0.26 for 50 Hz N = 7, p=.59, Student's t-test, Figure 4.7C). The degree of plasticity was independent of whether ChR2 was excited near or far from synaptic terminals (Figure 4.7—Supplemental Figure 1).

To analyze recovery from facilitation or depression, a test EPSC was evoked after a 20-pulse tetanus at time intervals increasing from 100 ms to 25.6 seconds (Figure 4.7A and E). This was repeated five to twenty times for each test pulse with a 30-second or

greater gap between sweeps and the results were averaged. We fit recovery data with single exponential functions, and found that depression observed by VCN input recovered with a time-course ($\tau_{20\ Hz}$ = 3.5 ± 0.7 sec, $\tau_{50\ Hz}$ = 3.1 ± 0.4 sec) comparable to the recovery from IC input facilitation ($\tau_{20\ Hz}$ = 4.5 ± 1.4 sec, $\tau_{50\ Hz}$ = 4.4 ± 1.7 sec, Figure 4.7E). While classical short-term facilitation lasts for only hundreds of milliseconds after tetanus stimuli (Zucker and Regehr, 2002), IC input facilitation onto MOC neurons lasted for tens of seconds. This longer-lasting facilitation resembles synaptic augmentation, which has a longer lifespan (seconds) than classical short-term facilitation (milliseconds) and a recovery time-course that is insensitive to the duration or frequency of repetitive activation (Magleby, 1987; Zucker and Regehr, 2002). Thus, while ascending and descending inputs to MOC neurons employ similar postsynaptic receptors, they differ dramatically in short-term plasticity.

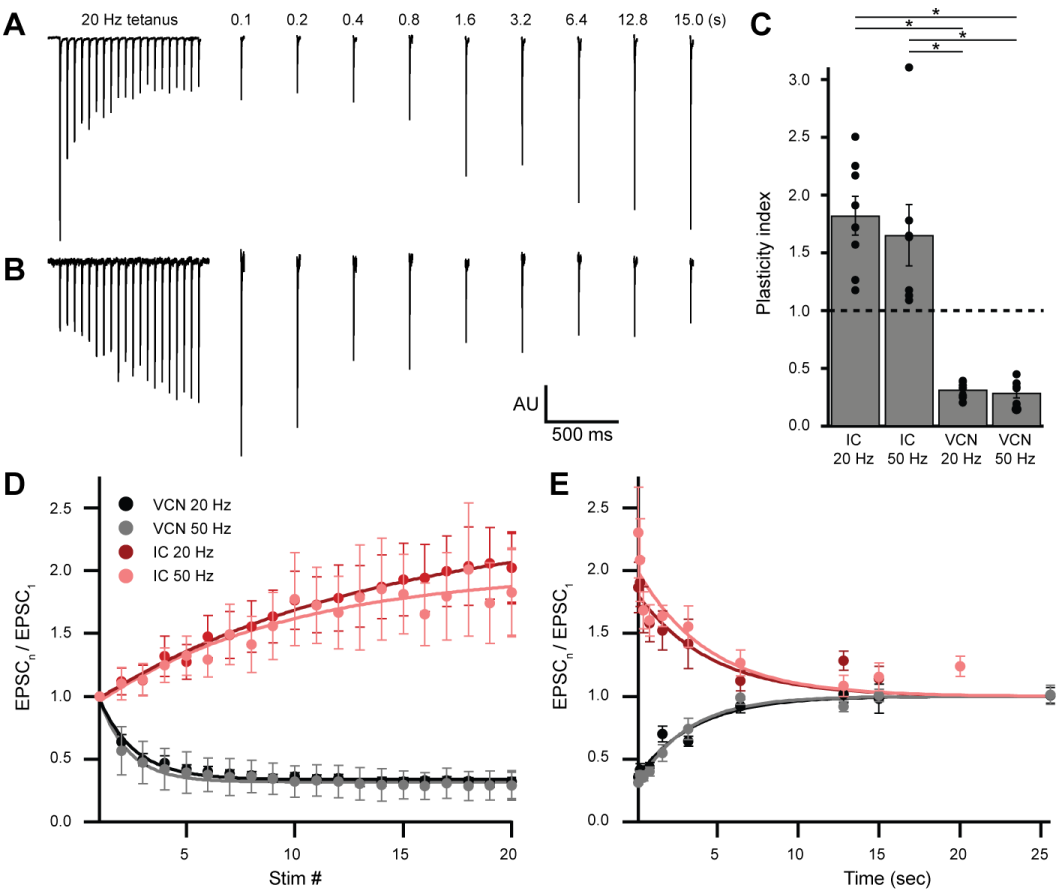

Figure 4.7: Ascending and descending inputs to medial olivocochlear neurons showed distinct short-term plasticity.

(**A**-**B**) Light-evoked EPSCs originating from VCN (**A**) or IC (**B**) input. During a 20 Hz tetanus stimulus, VCN-originating EPSCs depressed, whereas IC-originating EPSCs facilitated. After each 20-pulse tetanus, a test EPSC was evoked at time intervals increasing from 100 ms to 25.6 seconds. Each average test EPSC was normalized to the first EPSC of their respective tetanus stimulus.

(**C**) "Plasticity index" to illustrate the degree of facilitation or depression. The index for IC input was the ratio of the amplitude of the last three EPSCs of the tetanus over the amplitude of the first three EPSCs. The index for VCN input was the ratio of the amplitude of the last three EPSCs over the amplitude of the first EPSC of the tetanus. There was no significant difference between 20 Hz and 50 Hz stimulation between inputs of the same origin, however all IC input was significantly different to all VCN input ($p < .01$, two-way ANOVA with post-hoc Tukey test). Error bars are ± SEM.

(**D**) Ascending VCN input depresses in amplitude during a tetanus stimulation at both 20 Hz and 50 Hz (20 pulses) while descending IC input facilitates. The average normalized EPSC during a tetanus stimulation is shown for both VCN (*N*=7, 50 Hz; *N*=8, 20 Hz) and IC (*N*=7, 50 Hz; *N*=8, 20 Hz) input.

(**E**) Depression observed by ascending VCN input ($\tau_{20\,Hz}$ = 3.5 ± 0.7 sec, $\tau_{50\,Hz}$ = 3.1 ± 0.4 sec) recovered with a similar time-course to IC input facilitation ($\tau_{20\,Hz}$ = 4.5 ± 1.4 sec, $\tau_{50\,Hz}$ = 4.4 ± 1.7 sec).

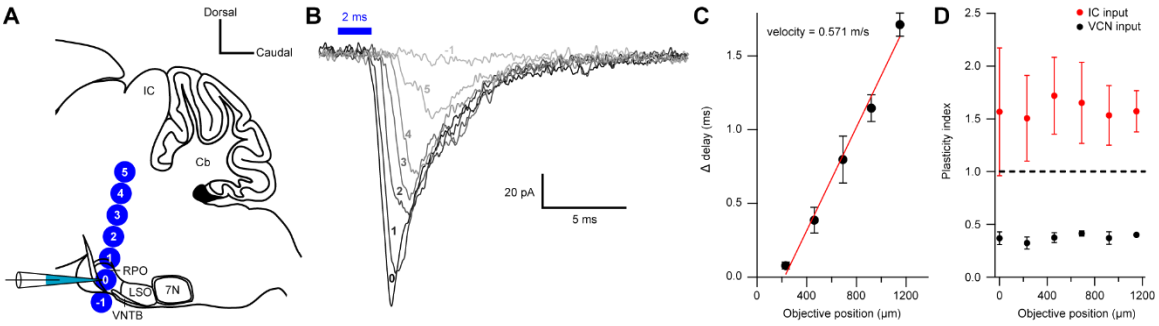

Figure 4.7—Supplemental Figure 1: Short-term plasticity from VCN and IC inputs onto medial olivocochlear neurons were observed with axonal and terminal level light-stimulation.

(**A**) Schematic illustrating the positioning of a 40X objective lens at varying distances with respect to a recording pipette attached to an MOC neuron (not to scale). For both VCN and IC input, the objective lens was moved either toward or away from the IC in 230 µm increments. It was assumed that axonal stimulation of IC input resulted in orthodromic activation, while axonal stimulation of VCN input resulted in antidromic activation, as VCN originating T-stellate neurons project to the IC, further confirming that T-stellate neurons make functional depressing synapses onto MOC neurons.

(**B**) Example traces of EPSCs evoked from activating IC input at varying distances from the recording pipette. Numbers -1 through 5 correspond to the objective positions illustrated in panel **A**. As the objective lens was moved further from the recording location, EPSC onset was delayed. The EPSC amplitude often reduced, likely due to a lower probability of intact fibers at distances further from the recording site. Each trace was an average of 20 sweeps, low-pass Bessel filtered at 3000 Hz and baselined to 0 pA.

(**C**) A plot showing the increase in delay from the first EPSC with increasing distance from the recorded MOC neuron. The 'onset' of each EPSC was measured at -5 pA from baseline. Data from IC and VCN were not significantly different and the data was combined (N = 9 at 0 through 690 µm, N = 8 at 920 µm and N = 5 at 1150 µm). Axon velocity was determined from the slope of a linear fit of the mean data ($y = 0.00175 * x - 0.3844, r^2 = 0.989$). Error bars are ± SEM.

(**D**) Light-stimulation of VCN or IC inputs at varying distances from the recorded MOC neuron had no effect on short-term depression or facilitation, respectively. (For IC input, N = 4 at 0 through 690 µm, N = 3 at 920 through 1150 µm; for VCN input, N = 5 at 0 through 920 µm, N = 2 at 1150 µm). Error bars are ± SEM.

4.9 The onset and dynamic range of MOC neuron output is controlled by integrating facilitating and depressing inputs

We showed above that the intrinsic properties of MOC neurons permit them to fire over a wide range. Moreover it has been previously shown that MOC neurons respond dynamically to a wide variety of binaural sound intensities and frequencies (Liberman and Brown, 1986; Brown, 1989; Lilaonitkul and Guinan, 2009), and thus we expect large variation in the number of presynaptic fibers driving their output. Given these results, we asked how do synaptic inputs from IC and VCN, with their distinct forms of short-term plasticity, fully engage the firing capacity of MOC neurons? Our opsin-dependent approach did not allow us to investigate how MOC neurons respond to this presynaptic variation, as one cannot independently control individual fibers in a large population, nor can ChR2 be reliably activated at high, physiological firing rates characteristic of auditory neurons. Thus, we examined how MOC neurons would respond to diverse inputs by injecting synaptic conductance waveforms modeled after physiological data (see Methods and Figure 3.1). To simulate the dynamic firing range of IC and VCN neurons in response to *in vivo* acoustic stimuli (Ehret and Moffat, 1985; Rhode and Smith, 1986; Smith and Rhode, 1989; Kuwada et al., 1997; Ono et al., 2017), we generated low-rate (Figure 4.8Ai), and high-rate (Figure 4.8Aii) excitatory postsynaptic conductance (EPSG) waveforms, referred to as ~40 Hz and ~180 Hz, respectively. In mice, the total number of inputs to a single MOC neuron from any region is currently unknown. However, comparing average minimally stimulated light responses to maximal light responses from our *in vitro* data, we estimated that each MOC neuron in the brain slice receives an average of 4.2 ± 1.0 unilateral inputs from the IC (maximum of

13.8, $N = 15$), and 11.1 ± 2.4 unilateral inputs from the VCN (maximum of 35.5, $N = 15$). As these numbers were likely an underestimation due to our experimental preparation (e.g. dependence on virally induced ChR2 expression and damage of inputs during acute brain sectioning), our EPSG waveforms were varied to simulate a broad range of inputs (10, 20, 40 or 80). Additionally, each input's form of presynaptic short-term plasticity could be set to facilitating or depressing, based on our measured parameters. All of our modeled inputs simulated activity of neurons that tonically fire, as we hypothesize that this type of input is most likely to drive sustained responses in MOC neurons, for example, sustained choppers (T-stellate cells) from the VCN. The cellular identity and intrinsic properties of IC neurons that project to MOC neurons are currently unknown; however, since their nerve terminals in VNTB exhibit facilitation to repetitive presynaptic firing, it seems likely that these neurons may also exhibit tonic firing.

In response to a small number of facilitating inputs (labeled 'Fac' in the following figures) firing at ~40 Hz, few action potentials were evoked in MOC neurons (1.8 ± 0.8 for 10 inputs, and 5.3 ± 1.5 for 20 inputs, $N = 6$) (Figure 4.8Bi, D, and E), and the first peak of postsynaptic firing generally occurred hundreds of milliseconds after stimulus onset (271.1 ± 74.4 ms for 10 inputs, and 183.8 ± 59.0 ms for 20 inputs, $N = 6$) (Figure 4.8Bi, D, and F). With only 10 facilitating inputs at ~40 Hz, 2 out of 6 MOC neurons failed to reach action potential threshold (e.g., first row of Figure 4.9C). MOC neurons responded to increasing numbers of facilitating inputs with a linearly increasing number of spikes during each stimulus for both ~40 Hz and ~180 Hz paradigms (Figure 4.8E). Facilitating EPSGs at ~180 Hz generally elicited more action potentials with an earlier

onset than ~40 Hz EPSGs with the same number of inputs (Figure 4.8Bii, E, and F). Additionally, the slope (increase in number of spikes for a given increase in number of inputs) of linear fits to the data in Figure 4.8E also significantly increased with presynaptic firing rate; this slope will be referred to as firing sensitivity (FS). FS was 0.31 ± 0.06 for 40 Hz and 1.0 ± 0.1 for 183 Hz ($p<.01$, paired samples Student's *t*-test). In a small number of experiments, an EPSG waveform would drive an MOC neuron into depolarization block toward the end of each trial, likely due to voltage-gated sodium channel inactivation (e.g., Figure 4.8D, 80 facilitating inputs at ~180 Hz). When this occurred, we measured the average instantaneous frequency (spikes per second) of all action potentials before the onset of depolarization block whose amplitude surpassed a -20 mV threshold, and divided this number by half to extrapolate the number of spikes per 500 ms (Figure 4.8E, 2.10D).

Similar to facilitating EPSGs, the majority of depressing EPSG waveforms (labeled 'Dep' in the figures) elicited action potentials that fired in a sustained manner (Figure 4.8Cii-E), and the FS in response to EPSG waveforms significantly increased with presynaptic firing rate (Figure 4.8E). FS was 0.095 ± 0.014 for 40 Hz, and 0.31 ± 0.08 for 180 Hz ($p<.01$, paired samples Student's *t*-test). Some MOC neurons failed to reach action potential threshold in response to depressing waveforms at ~40 Hz (6/6 failures with 10 inputs, and 3/6 with 20 inputs), and ~180 Hz (3/6 failures with 10 inputs) (e.g., last two rows of Figure 4.8D). When action potentials were elicited and the number of simulated inputs were equivalent, depressing waveforms at ~180 Hz always drove MOC neurons to threshold earlier than those at ~40 Hz (Figure 4.8F). At ~40 Hz, with 20

to 40 simulated inputs, depressing waveforms often elicited an onset response (Figure 4.8Ci) that occurred earlier than facilitating waveforms at the same rate (Figure 4.8D and F). When the presynaptic firing rate was increased to ~180 Hz, facilitating waveforms with 10 to 20 simulated inputs generally elicited an onset response sooner than with depressing inputs. As our previously described experiments demonstrated that inputs from IC facilitated and those from VCN depressed (Figure 4.7) our simulated inputs suggest that, individually, VCN inputs best drive slow rates of sustained activity in MOC neurons, and IC inputs best drive high-rates of activity. Combinations of these inputs are needed to access the full dynamic range of MOC neuron firing, as our simulated VCN-like (depressing) EPSGs could only drive the firing rate (47.8 ± 5.9 Hz average maximum, $N = 6$) to about half of the maximum rates measured *in vivo* (Liberman, 1988a; Brown, 1989), while IC-like (facilitating) EPSGs could drive MOC neurons to fire at maximal rates (180 ± 12 Hz average maximum, $N = 6$) more comparable to our *in vitro* experiments (Figure 4.2).

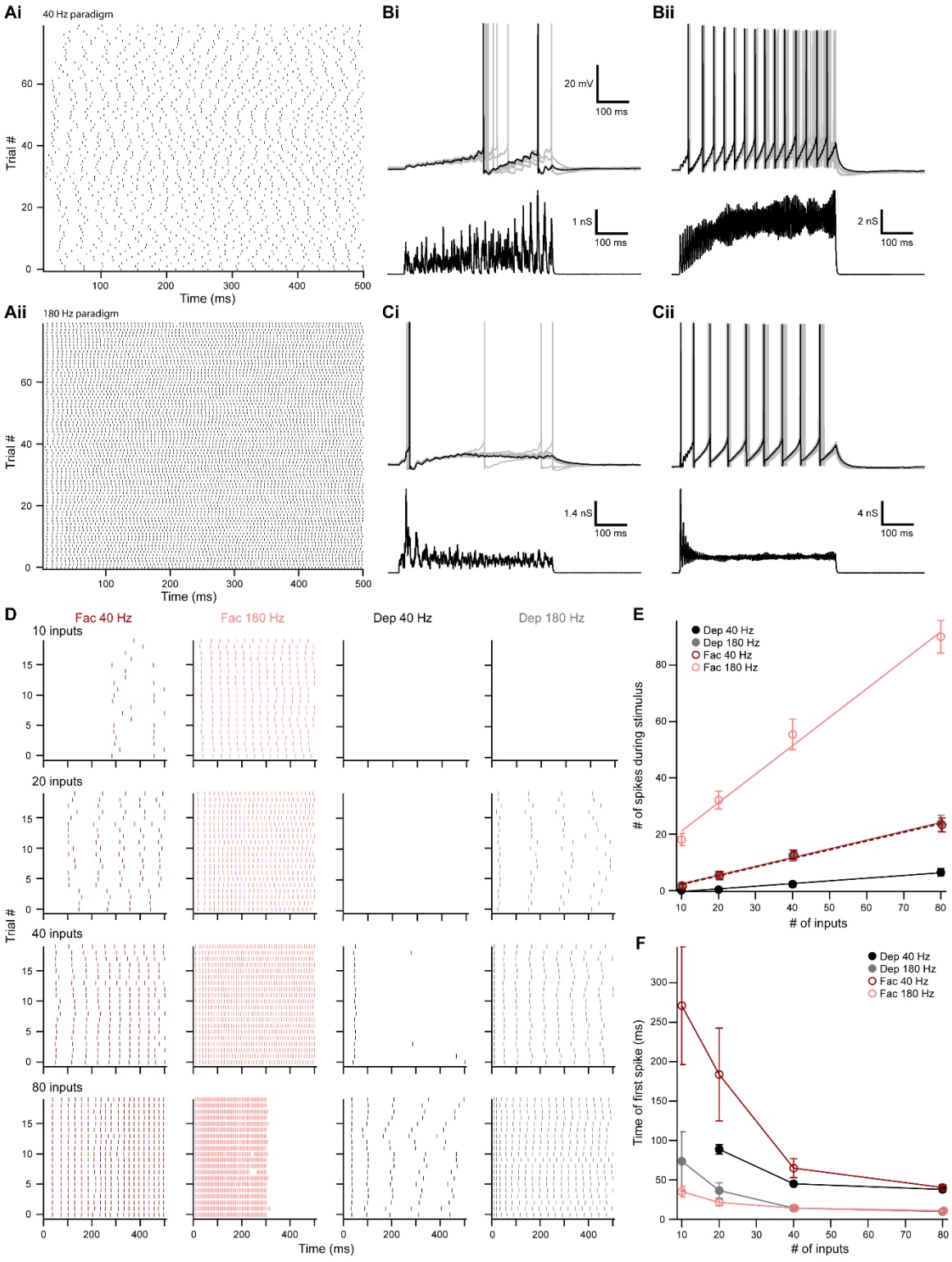

Figure 4.8: The number of presynaptic inputs and type of short term plasticity control the dynamic range and onset timing of MOC neuron output.
(Continued on next page)

(**A**) Raster plots of presynaptic EPSG onset timing. The ~40 Hz paradigm (**Ai**) had an average rate of 41.1 ± 0.5 Hz for all 80 trials. The ~180 Hz paradigm (**Aii**) had an average rate of 176 ± 1 Hz for all 80 trials. Each trial was considered a presynaptic input in our model.
(**B**) Ten examples traces of membrane voltage responses to injected conductance waveforms simulating 10 inputs at ~40 Hz (**Bi**) or ~180 Hz (**Bii**) that underwent short term facilitation. Scale bar is the same for all voltage responses in (**B**) and (**C**).
(**C**) Ten examples traces of membrane voltage responses to injected conductance waveforms simulating 40 inputs at ~40 Hz (**Ci**) or ~180 Hz (**Cii**) that underwent short term depression.
(**D**) Example raster plots of postsynaptic MOC neuron action potential timing in response to injected conductance waveforms. Rows of raster plots correspond to the number of simulated inputs, and columns correspond to the type of simulated presynaptic short term plasticity and firing rate. Blank raster plots represent an absence of firing. One example (80 presynaptic inputs at ~180 Hz with short term facilitation) underwent depolarization block after ~300 ms. All examples are from the same MOC neuron.
(**E**) Average total number of action potentials evoked in MOC neurons (N = 6) during each conductance waveform paradigm. Error bars are ± SEM.
(**F**) Average timing of the peak of the first action potential evoked in MOC neurons (N = 6) during each conductance waveform paradigm. Error bars are ± SEM.

4.10 Descending input to MOC neurons can enhance or override ascending reflex input

The output of MOC neurons *in vivo* depends on the integration of multiple input subtypes, where weaker ascending inputs may be optimized or overridden by more powerful descending inputs. To investigate how MOC neurons would respond to this type of integration, we injected EPSG waveforms simulating combinations of ascending (depressing) and descending (facilitating) inputs. In order to avoid artificially introducing synchrony between the modeled VCN and IC inputs we introduced a third average presynaptic firing rate, ~110 Hz (Figure 4.9A). Using the ~180 Hz paradigm, 20 depressing inputs elicited a low number of action potentials in MOC neurons, without any failures (5.5 ± 1.4 spikes on average, $N = 6$) (Dashed grey line, Figure 4.9D), with the first action potential occurring at 36.5 ± 6.6 ms after the stimuli onset (Dashed grey line, Figure 4.9E). To experimentally test how IC-like inputs altered this VCN-like response, we concurrently introduced 10 to 80 facilitating inputs at ~40 Hz or ~110 Hz (Figure 4.9). As expected, the number of action potentials evoked by facilitating or depressing input was increased when the both types were combined (Figure 4.9B-D). However, the magnitude of this effect was dependent on the strength of the facilitating input, as spikes evoked by weaker facilitating inputs (1.6 ± 0.8 spikes on average for 10 inputs at ~40 Hz, and 8.6 ± 2.6 spikes at ~110 Hz) were significantly enhanced when combined with the depressing paradigm (9.2 ± 2.3 spikes at ~40 Hz, 16.1 ± 3.1 spikes at ~110 Hz) ($p<.05$ within each group, paired samples Student's *t*-test), whereas stronger facilitating inputs were not enhanced (for example, 67.3 ± 8.0 spikes on average for 80 inputs at ~110 Hz versus 68.7 ± 0.4 when combined) (Figure 4.9D). Thus, our modeled

facilitating IC inputs effectively drive MOC firing, and input from depressing VCN synapses only enhanced firing when the IC input was relatively weak.

Combining facilitating and depressing inputs is expected to impact the timing of postsynaptic action potentials, and so we also examined the onset time of firing. At ~40 Hz, the onset of the first action potential evoked by facilitating inputs occurred earlier when combined with the depressing paradigm, but the strength of this effect decreased with increasing number of facilitating inputs (Figure 4.9E). The same was true of ~110 Hz facilitating inputs when simulating only 10 or 20 inputs. However, there was little difference as the number of inputs increased. The FS of facilitating inputs (0.32 ± 0.06 at ~40 Hz, and 0.82 ± 0.18 at ~110 Hz) was not significantly altered with the addition of a depressing input (0.30 ± 0.09 at ~40 Hz, and 0.74 ± 0.12 at ~110 Hz, $N = 5$) ($p>.05$ within each group, paired samples Student's *t*-test) (Figure 4.9D), demonstrating that MOC neurons generally summate concurrent inputs, and confirming that they linearly respond to signals in proportion to the intensity of their input (Figure 4.2). Overall, these results suggest that relatively weak descending inputs to MOC neurons are enhanced when combined with ascending input, while relatively strong descending inputs override ascending input—evoking an equivalent amount of spikes with similar onset, whether or not the ascending input is active. The data therefore confirm the potency of the descending control of the MOC system, as compared to the reflex pathway.

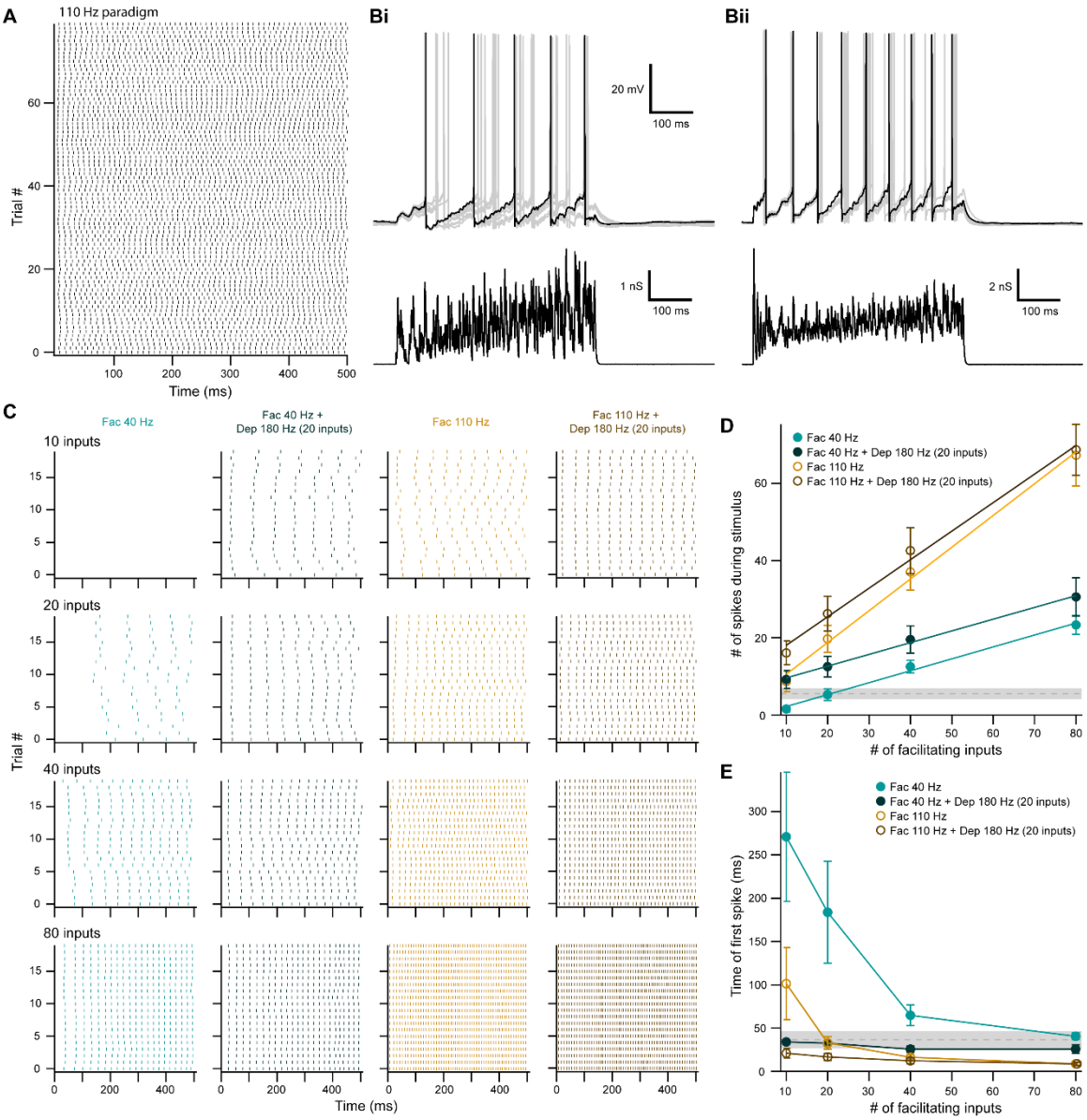

Figure 4.9: Facilitating inputs to MOC neurons can override or be enhanced by depressing inputs, depending on their number and rate.

(**A**) Raster plot of presynaptic EPSG onset timing for the ~110 Hz paradigm which had an average rate of 111 ± 1 Hz for all 80 trials. Each trial was considered a presynaptic input in our model.

(**B**) Ten examples traces of membrane voltage responses to injected conductance waveforms simulating 20 facilitating inputs at ~40 Hz without (**Bi**) or with (**Bii**) the addition of 20 depressing inputs at ~180 Hz. Scale bar is the same for both voltage responses.

(**C**) Example raster plots of postsynaptic MOC neuron action potential timing in response to injected conductance waveforms, without (even columns) or with (odd columns) the addition of 20 depressing inputs at ~180 Hz. Rows of raster plots correspond to the

(Continued on next page)

number of simulated inputs, and columns correspond to the type of simulated presynaptic short term plasticity and firing rate. Blank raster plots represent an absence of firing. All examples are from the same MOC neuron.
(**D**) Average total number of action potentials evoked in MOC neurons (N = 5) during each conductance waveform paradigm. Error bars are ± SEM. Grey dashed line represents 20 depressing inputs at ~180 Hz, and the shaded area represents ± SEM in (**D**) and (**F**).
(**F**) Average timing of the peak of the first action potential evoked in MOC neurons (N = 5) during each conductance waveform paradigm. Error bars are ± SEM.

CHAPTER V: DISCUSSION

In the present study, we contrasted excitatory inputs onto MOC neurons through two distinct sources, an ascending, reflex pathway, and a descending pathway from the midbrain. Few studies have explored the properties of MOC neurons, in part due to the difficulty of identifying the neurons in mature, heavily myelinated tissue. In order to overcome previous limitations and visualize MOC neurons in acute brain sections from older mice, we utilized a ChAT-Cre mouse line which genetically marks cholinergic neurons in the SOC. This line was recently characterized by Torrez Cadenas, Fischl, and Weisz (2019), where it was shown to label cholinergic MOC efferent neurons. Using CTB mediated retrograde tract tracing originating from the inner-ear, we were able to confirm and expand on their results. Agreeing with classic anatomical tract tracer studies of MOC neurons (for review see Warr, 1992), we demonstrated that approximately two thirds of ChAT-Cre/tdTomato positive VNTB neurons project to contralateral cochlea, whereas one third project to ipsilateral cochlea. Additionally, retrogradely labeled VNTB neurons were always positive for tdTomato, confirming that the ChAT-Cre mouse line expressed Cre recombinase in most, if not all, MOC efferent neurons in the VNTB.

5.1 Firing rates of MOC neurons

Our examination of intrinsic properties of MOC neurons revealed a remarkable capacity to encode the intensity of current steps with a linear increase in postsynaptic firing over a wide range. Further, we showed that this linearity is recapitulated in the

responses to synaptic activity, as modeled through conductance clamp. Previous work by Fujino et al. (1997) reported MOC and LOC neuron intrinsic membrane properties of neonatal rats (P3-9). However, due to the difficulty of visualizing brainstem neurons in older animals with tract tracers, they were not able to record from MOC neurons after the onset of hearing (P12-14). Additional studies on MOC neurons that used whole-cell recording and tract tracing were also limited to younger animals near or prior to onset of hearing (Wang and Robertson, 1997; Mulders and Robertson, 2001). Consistent with properties described in prehearing rats (Fujino et al., 1997), we reported that a majority of matured MOC neurons did not spontaneously fire, and that their spike frequency linearly increased with intensity of injected current pulses. This conclusion is supported by *in vivo* recordings at the level of the auditory nerve, where MOC efferents exhibit little-to-no spontaneous firing, and respond linearly to increasing sound intensity (Cody and Johnstone, 1982; Robertson, 1984; Robertson and Gummer, 1985). A recent study (Torres Cadenas et al., 2019) reported that MOC neurons from P12-23 mice exhibited spontaneous firing, which may be due to developmental changes specific to mice (we recorded from P30-48), or due to differences in acute brain slice preparation. Developmental transcriptomics of auditory efferent neurons could reveal the basis for these changes.

Intriguingly, *in vivo* recordings rarely report sound-driven firing rates in MOC efferents above 100 Hz, yet we report that many MOC neurons are able to fire action potentials at rates greater than 250 Hz in response to somatic current injections. The high firing rates achieved *in vitro* may better reflect MOC neuron capabilities, as *in vivo*

experiments are often performed with anesthetics that produce extensive systemic changes in neurotransmission. An alternative interpretation is that the wide firing range intrinsic to MOC neurons ensures that over the narrower range used *in vivo*, the linearity of input-output relations remains preserved. MOC neurons are known to receive modulatory inputs from adrenergic, serotonergic and peptidergic sources (Thompson and Thompson, 1995; Woods and Azeredo, 1999; Mulders and Robertson, 2000, 2001; Thompson and Schofield, 2000; Horvath et al., 2003), and can be excited by a handful of neuromodulators (Wang and Robertson, 1997, 1998). This suggest that sound-driven firing rates in MOC neurons observed *in vivo* may be contextually enhanced by activation of neuromodulatory inputs.

5.2 Excitatory MOC neuron inputs utilize fast-gating CP-AMPARs

The ability of the MOC system to dampen cochlear sensitivity likely depends on the convergence of excitatory synaptic inputs from ascending and descending brain regions. Tract-tracer and lesion studies have determined that ascending projections originate from the posteroventral cochlear nucleus (Thompson and Thompson, 1991; De Venecia et al., 2005; Darrow et al., 2012; Brown et al., 2013). These ascending projections are involved in the reflex MOC pathway, and are likely mediated by T-stellate neurons. However, bushy cells may also play a role, as they send axon collaterals which terminate in VNTB, the primary location of MOC neuron somata (Smith et al., 1991). Descending projections to MOC neurons originate from auditory and non-auditory regions, including brainstem, IC, thalamus and cortex (Thompson and Thompson, 1993; Vetter et al., 1993; Mulders and Robertson, 2002). The IC is a major source of dense,

tonotopically arranged, glutamatergic projections to ipsilateral VNTB (Thompson and Thompson, 1993; Saint Marie, 1996; Suthakar and Ryugo, 2017) where the majority of IC projections terminate, and their targets include MOC neurons.

In the present study, we elucidated pre- and postsynaptic properties of excitatory VCN and IC inputs onto MOC neurons by using nucleus- and cell-specific virally-driven optogenetic excitation. We demonstrated that MOC neurons receive excitatory input from VCN and IC, both of which transmit using fast-gating CP-AMPARs. Together with somatic puff application of glutamate and mEPSC analysis, our investigation revealed that inwardly rectifying, fast-gating CP-AMPARs are a fundamental postsynaptic feature of excitatory synaptic transmission at MOC neurons.

The utilization of GluR2-lacking AMPARs, with ultra-fast mEPSC decays (less than 200 μs), is reminiscent of auditory nerve synapses in the VCN, including those onto T-stellate cells (Gardner et al., 1999, 2001). Higher regions of the auditory pathway typically lack this feature of the synapse, even in the adjacent medial nucleus of the trapezoid body, whose mEPSCs are slower than in MOC neurons and likely contain GluR2 (Koike-Tani et al., 2005; Lujan et al., 2019). We do not know if the mEPSCs originated from synapses made by VCN or IC neurons or both, but the uniformity of mEPSC properties suggests that even descending fibers from IC can trigger insertion of such fast-gating receptors. While the presence of fast kinetic receptors is considered to be an adaptation to preserve microsecond precision of sensory timing (Trussell, 1999), it seems unlikely that such precise timing is needed in the efferent system. Further studies

are needed to examine how receptor channel kinetics impact the integrative functions of the MOC neuron.

5.3 T-stellate neurons are an MOC reflex interneuron

Neurons identified as T-stellate cells are believed to terminate in VCN, DCN, olivary nuclei, lemniscal nuclei, and IC (Warr, 1995; Oertel et al., 2011), but it is not clear if axons of the same neuron can have such diverse projections. Using an intersectional AAV approach, we directly demonstrated that T-stellate neurons drive activity in MOC neurons, consistent with suggestions from previous anatomical and lesion studies (Thompson and Thompson, 1991; De Venecia et al., 2005; Darrow et al., 2012). T-stellate projections and terminals in many known target nuclei were consistently observed in brain sections prepared for microscopy (Figure 4.4—Supplemental Figure 1). Nevertheless, eliciting a post-synaptic current was qualitatively difficult when compared to non-specific virally mediated ChR2 expression in the VCN. This was possibly due to sparse ChR2 expression among T-stellate neurons resulting from the requirement of coincident infection by two different viruses in the same neuron; alternatively, ChR2 expression may have been too low to consistently reach action potential threshold using the intersectional AAV scheme. There also may be sub-populations of T-stellate neurons which project to MOC neurons and do not project to the IC; non-IC projecting T-stellate neurons would not express ChR2 using this intersectional virus approach. Nevertheless, this approach highlights the enormous range of targets of these neurons, as at least a subset of IC projecting T-stellate neurons also directly synapsed onto MOC neurons. Genetic manipulation of only T-stellate neurons with this dual AAV approach will be

useful in future studies to help elucidate functional significance of T-stellate projections in other auditory circuits.

5.4 Effect of short-term synaptic plasticity on MOC neuron output

Neurons throughout the brain receive mixtures of synaptic inputs that vary not only in their origin or information content, but their short-term plasticity. A prominent example is that of cerebellar Purkinje neurons, whose parallel fiber inputs facilitate while climbing fiber inputs depress (Sakurai, 1987; Hansel and Linden, 2000). The physiological functions served by this diversity likely vary with brain region. In MOC neurons, we found that synaptic responses having properties of the ascending or descending inputs alone were not capable of encoding firing over a wide range and with short latency. However by combining these different types of input and varying input number and firing rate, sustained MOC output could vary over 20-fold. We suggest that this central synaptic mechanism could aid in grading the level of efferent dampening of cochlear function according to sound level.

Inputs from IC strengthened considerably for tens of seconds with repetitive presynaptic stimulation, resulting in a facilitation that resembles the augmentation seen at neuromuscular junction (Magleby and Zengel, 1976) (Figure 7), whereas VCN and T-stellate inputs (Figure 4G) decreased in synaptic strength, resulting in acute short-term depression. Both forms of plasticity recovered with a similar time course, suggesting that conditioning of these synapses could have lasting effects, and bias efferent signaling towards top-down control. The depression of VCN inputs to MOC neurons is not likely

due to desensitization of ChR2, since trains of light pulses triggered reliable spikes in VCN neurons. Moreover, injections into IC were made with the same virus, and those inputs never exhibited depression. Thus, distinct forms of presynaptic plasticity are likely exhibited by IC and VCN inputs to the same cell type. Depression of VCN inputs is surprising, given that they mediate a reflex pathway and one might therefore expect reliability within such a circuit. Moreover, as with MOC neurons, T-stellate neurons fire action potentials in a relatively sustained manner in response to sound stimuli. In *in vivo* recordings at the level of the auditory nerve, MOC neurons respond to sound input with latencies as short as 5 milliseconds (Robertson and Gummer, 1985; Liberman and Brown, 1986), and T-stellate cells are well suited to provide the rapid onset portion of this response, as demonstrated in our simulation of this input (Figure 8). However, our results suggest that for sustained activity of MOC efferents, non-VCN inputs, such as from the IC, may be a necessary component of efferent control of cochlear function. Indeed, a recent auditory system computational model suggested that descending IC inputs to the MOC system are necessary for persistent enhancement of signal in noise, and that the MOC system functions across a broad range of intensity (Farhadi et al., 2021). These features of the model are now affirmed by our observations of potent input from IC, dependent on synaptic augmentation, and the intrinsic properties of MOC neurons that support a remarkably wide dynamic range. Moreover, we suggest that the stable, excitatory control of efferent neurons by descending input raises the possibility that regulation of cochlear sensitivity may be under rapid control associated with attention (Delano et al., 2007; Wittekindt et al., 2014), preceding sounds (Otsuka et al., 2018), or other changes in brain state.

CHAPTER VI: SUMMARY AND CONCLUSIONS

The medial olivocochlear (MOC) reflex is part of an efferent system that controls auditory sensitivity by modulating the strength of cochlear amplification. MOC neurons provide efferent fibers to the cochlea and are contacted by multiple central pathways. This research aimed to determine how the MOC reflex is governed by such diverse inputs. The experiments in this dissertation used a combination of transgenic mutations, histochemistry, virally mediated optogenetics, and patch- and conductance-clamp electrophysiology to test hypotheses regarding three crucial components of this system: (1) MOC neurons, and (2) excitatory inputs from ventral cochlear nucleus (VCN) and (3) inferior colliculus (IC). Based on the findings of this work, it can be concluded that the acoustically evoked MOC reflex can be enhanced or overridden by remarkably powerful IC input—implicating a dominant role for descending pathways over efferent function.

6.1 MOC neuron-specific identification and manipulation in vitro

In order to study MOC neurons, I first required a strategy to selectively and routinely locate them in VNTB of acute mouse brain sections. Classically, olivocochlear neurons have been visualized in this type of preparation after retrograde tract tracers have been introduced into the inner ear (Warr, 1975a). In combination with whole-cell patch clamp recording, retrograde tract-tracing has aided in the characterization of MOC neuron electrophysiological properties and ion channel composition of prehearing, neonatal rats (Fujino et al., 1997; Wang and Robertson, 1997). Conversely, the difficulty

of visualizing tract tracer labeled MOC neurons in the presence of the dense neuropil and myelinated axons of older vertebrates has contributed to a paucity of whole-cell recording from animals after the onset of hearing. In order to study MOC neurons in hearing aged mice (>P15), an alternative method of routinely visualizing and manipulating MOC neurons *in vitro* was needed.

While MOC neurons are cholinergic and express choline acetyltransferase (ChAT), they were not revealed in transgenic mice created using bacteria artificial chromosome-mediated genetic labeling of ChAT (Gong et al., 2003; von Engelhardt et al., 2007; Leijon and Magnusson, 2014). However, a more recent mouse line, ChAT-IRES-Cre (Madisen et al., 2010; Rossi et al., 2011), expressing Cre recombinase under the ChAT promoter, greatly increased the labeling of cholinergic neurons in auditory brainstem, including auditory efferents (Torres Cadenas et al., 2019). It was only after confirming that this mouse line could indeed be used to express Cre recombinase dependent fluorophores in MOC neurons that I was able to move forward with this study. This was accomplished by determining that ChAT-Cre/tdTomato VNTB neurons were retrogradely labeled after injecting tract-tracer into the inner ear. Even with the aid of a genetically encoded marker, MOC neurons were difficult to visualize in older animals with fluorescent microscopy, as they were sparsely distributed across the superior olivary complex (SOC) and were partially obscured by heavy myelination. With practice, I was able to overcome this deficit in visibility and routinely record from MOC neurons in SOC of older animals and examine their intrinsic properties.

6.2 Electrical properties of MOC neurons in vitro

I first concentrated on exploring MOC neuron firing properties in response to current injections, as the only reported data from whole-cell recordings were either from or combined with those of prehearing animals (Fujino et al., 1997; Wang and Robertson, 1997; Torres Cadenas et al., 2019). This distinction between 'older' and 'prehearing' aged animals was needed because the intrinsic and synaptic properties of many auditory system neurons change around the onset of hearing (Brenowitz and Trussell, 2001; Sonntag et al., 2011; Rubio, 2020). Moreover, MOC efferents undergo discrete developmental changes over this critical time period, where they transiently contact inner hair cells near Type I spiral ganglion neurons (Simmons et al., 1996; Simmons, 2002). As MOC neurons are thought to play a homeostatic function at this time (Clause et al., 2014), it was conceivable that their firing properties were differentially adapted to the requirements of their pre- and post-hearing roles. However, my results were consistent with whole-cell recordings from prehearing rats, and *in vivo* recordings at the level of the auditory nerve, as MOC neurons from 30 – 48 day old mice showed little spontaneous firing and linearly responded to increasing current injections with an increasing spiking rate. While this was reminiscent of efferent fibers responding to increasing sound intensity *in vivo* (Cody and Johnstone, 1982; Robertson, 1984; Robertson and Gummer, 1985), they also demonstrated the ability to fire at maximum rates over two-fold higher. Further studies will be required to determine how this wide dynamic range of spiking rates is utilized, as neuromodulatory inputs likely enhance the excitability of MOC neurons, and the roles played by descending inputs, including those from auditory cortex,

have yet to be fully explored. Opsin mediated *in vivo* activation of these types of inputs may enhance the sound evoked response of efferent fibers, which could be measured at the level of the auditory nerve or by evaluating distortion product otoacoustic emissions (DPOAEs).

6.3 Inputs to MOC neurons

Previous studies suggest that ascending inputs to MOC neurons originate from VCN, and descending inputs originate from numerous higher brain regions, including IC. However, prior to the experiments in this dissertation, no specific excitatory input to MOC neurons had been functionally demonstrated. Of note is the field's interest in the cellular identity of ascending input from VCN, often referred to as the "reflex interneuron". Anatomical, lesion, and tract tracer studies propose that T-stellate cells provide this input (Warr, 1972; De Venecia et al., 2005; Darrow et al., 2012). The importance of identifying this neuron in particular is that it links the sound-evoked activity of the auditory nerve to MOC neurons, making them an essential relay for function of the reflex arc. Using a modern genetic toolset, I pioneered an intersectional AAV approach that enabled specific optogenetic activation of T-stellate cell synapses while recording from MOC neurons. I was able to provide the first direct evidence that T-stellate cells are a de facto interneuron of the MOC reflex using this method. However, as MOC efferent fibers are sharply tuned to unilateral pure tones (Fex, 1962; Cody and Johnstone, 1982) but respond best to bilateral broadband noise (Lilaonitkul and Guinan, 2009), additional studies are required to determine the frequency specificity of these inputs and their relative strengths. While it is likely that MOC neurons receive strong

ascending input at their characteristic frequency, this has never been definitively demonstrated. Genetically encoded markers that can be induced by acoustically evoked neural activity (Sørensen et al., 2016) would be particularly useful for determining the frequency specificity of inputs to MOC neurons. Studies such as these may further define the role of T-stellate cells or implicate the existence of additional circuitry that is involved in the reflex pathway. Furthermore, it is not known if their robust response to noise is due to the integration of many broadband ascending inputs from cochlear nucleus, or due to descending circuitry. Indeed, many IC neurons respond best to noise, and a recent model by Farhadi et al., (2021) suggests that these noise-sensitive inputs to MOC neurons play an essential role in detecting sound in noise.

The intersectional AAV approach used in Section 4.4 was useful for demonstrating that T-stellate cells make functional synapses onto MOC neurons. However, broad channelrhodopsin (ChR2) expression in VCN using an anterograde virus resulted in a higher probability of observing an EPSC when recording from MOC neurons. This was likely due to a few reasons: First, expression of ChR2 with the intersectional approach was dependent on the coincidence of two viral vectors in each individual T-stellate cell, lowering the overall probability of ChR2 expression. Second, it is unknown to what extent axons that synapse onto MOC neurons from VCN also send collaterals to IC. As a population, T-stellate neurons are documented to send axon collaterals to many far-spanning targets (medial geniculate, IC, lateral lemniscus, SOC, dorsal cochlear nucleus) (Oertel et al., 2011) and it is not known if each T-stellate cell terminates in all of these nuclei or if subpopulations exist with a narrower range of

targets. Non-IC projecting VCN neurons that synapse onto MOC neurons would not be excitable with this intersectional approach. Lastly, it is possible that MOC neurons receive ascending input from additional cell types, such as bushy cells in the VCN. Experiments using bushy cell specific transgenic lines, such as the Math5-Cre line (Saul et al., 2008), would be useful in determining if they play a role as an additional reflex interneuron.

While using optogenetics to stimulate IC or VCN inputs, I found that both utilized similar fast-gating, inwardly rectifying Ca^{2+}-permeable AMPA receptors on postsynaptic MOC neurons. The function of these presynaptic inputs had not been previously demonstrated, and I hypothesized they would show little to no plasticity with repetitive stimulation, acting purely as a relay to engage the MOC reflex. However, I was surprised to find that inputs from these two nuclei contrasted in presynaptic short-term plasticity, with VCN input showing depression and IC input showing facilitation.

One initial worry about these results was how much they were influenced by the use of opsins. ChR2 desensitizes in response to high-rate repetitive stimulation. In fibers with low ChR2 expression, desensitization could create an artificial onset response if early stimuli caused the membrane potential to reach spike threshold but subsequent stimuli did not. With my equipment, all ChR2-positive fibers were stimulated concurrently in the plane of the microscope objective. This may have led to the artificial enhancement of early responses where all fibers responded to early stimulation but only high ChR2-expressing fibers were able to follow the entire train. One way to test for this

type of artificial response would be to record from ChR2 positive T-stellate cell somata and confirm that light stimulation of distal axons could reliably evoke action potentials by detecting antidromic responses. Nevertheless, the exact same viral construct was used to express ChR2 in IC and VCN originating fibers, and opposing types of plasticity were indeed revealed—with IC input never showing depression. This stark and consistent difference in presynaptic plasticity validates that artificial responses were not likely with the viral construct or opsins used in this work.

6.4 Effect of short-term plasticity on MOC neuron spike output

Section 4.9 sought to answer the question: "how do synaptic inputs from IC and VCN, with their distinct forms of short-term plasticity, fully engage the firing capacity of MOC neurons?" To explore this question, it was ideal to have control over multiple, discrete excitatory inputs from each pathway, and to activate them at physiological firing rates while recording spike output from MOC neurons. Simulation of this type of control over presynaptic inputs was achieved with an analog conductance-clamp circuit, which allowed for the injection of synaptic-like conductances into MOC neurons. These experiments determined that, compared to ascending inputs, descending inputs exert more dominant control over the MOC system, and integration of both pathways is necessary to access the wide dynamic range of firing rates intrinsic to MOC neurons.

The broad range of presynaptic rates and the number of inputs simulated in these experiments were modeled after physiological data; however, the total number of synapses from either pathway is unknown, nor are the identities and firing properties of

neurons providing descending input from IC. Further studies are needed to refine the parameters used for modeling these synapses, such as serial electron microscopic reconstruction of whole MOC neurons with accurate counts of specific inputs. Moreover, the frequency in which innovative ChR2 variants are engineered and made available to the scientific community is remarkable (Boyden et al., 2005; Lin et al., 2009; Gunaydin et al., 2010; Klapoetke et al., 2014; Bedbrook et al., 2019). In combination with increasingly available 3D photoactivation techniques (Ronzitti et al., 2018), it is feasible that precise three-dimensional optogenetic control of entire neuronal networks will become commonplace. More modern toolsets such as these will allow for the disentangling of the diverse roles played by MOC efferents by bypassing many of the assumptions needed for the modeling and simulation of their inputs.

While the experiments in this dissertation were performed on the MOC efferent system, the mechanisms underlying its output are common to many sensory and reflex circuits—where dynamic integration and processing of convergent pathways is required to encode the output of a system. In the context of the efferent system, inhibition of the cochlear amplifier is most effective at high, repetitive frequencies, which cause slow decaying efferent mediated responses to facilitate and summate (Goutman et al., 2005). This suggests that the rate of efferent firing is more essential than precise timing. Thus, as determined by the work in this dissertation, MOC neurons and their inputs are specialized for engaging and maintaining repetitive firing over a wide dynamic range in order to directly influence acoustic signaling at the level of the cochlea.

APPENDIX: A CRE MOUSE LINE LABELING STELLATE CELLS OF THE POSTEROVENTRAL COCHLEAR NUCLEUS

A.1 Somatostatin-Cre labels stellate and bushy cells of the ventral cochlear nucleus

T-Stellate (planar multipolar) cells of the ventral cochlear nucleus (VCN) are excitatory neurons that receive frequency specific input from auditory nerve. Their axons have wide ranging targets, including local collaterals, superior olivary complex (SOC), dorsal cochlear nucleus (DCN) and inferior colliculus (IC) (Oertel et al., 2011). During *in vivo* recordings, they responds to pure tones with sustained, tonic firing, and the rate of firing increases monotonically with sound intensity (Rhode and Smith, 1986; Blackburn et al., 1989). The purpose of the following experiments were to characterize a transgenic mouse line that marked T-stellate cells in order to perform cell specific anatomical, electrophysiological, and optogenetic studies.

The peptide somatostatin (Sst) is expressed in VCN during early development (Sekitani et al., 1990; Wynne et al., 1995) and has been detected in neurons with stellate (multipolar) morphology (Wynne and Robertson, 1997). Reported in this appendix is an analysis of labeled cells in the VCN of an Sst-Cre mouse line (Sst(tm2.1(cre)Zjh), Jackson Laboratory). This line was crossed to an Ai9 tdTomato reporter to generate mice with tdTomato in Cre positive cells (Sst-Cre/tdTomato). In immunohistochemically enhanced sections (see methods in Section 3.2), labeled cells were observed throughout the VCN, with only sparse somata found in the DCN (Figure A.1, and Figure A.2A). This

mouse line was then crossed to a well characterized GlyT2-GFP BAC transgenic line (referred to as Sst-Cre/tdTomato::GlyT2-GFP) (Zeilhofer et al., 2005; Kuo et al., 2012; Moore and Trussell, 2017; Ngodup et al., 2020) to double label for Cre and glycinergic inhibitory neurons (Figure A.1A and B). In the VCN, most cells were not double labeled, suggesting that the majority of Cre positive cells were excitatory neurons (Figure A.1A). Hardly any GFP or tdTomato positive cells were observed in the octopus cell area (Figure A.1A), suggesting that octopus cells were not labeled in either mouse line. A few large, double-labeled cells were observed (Figure A.1B), and were consistent with the morphology of D-stellate neurons, a large inhibitory projection cell (Doucet et al., 1999).

T-stellate cells are named after the pathway followed by their axonal projections, which travel through the **t**rapezoid body after exiting the VCN (Oertel et al., 1990). TdTomato positive axons were visible in the trapezoid body of Sst-Cre/tdTomato mice, suggesting these projections may originate from T-stellate cells (Figure A.1C). Moreover, cells filled with biocytin during whole-cell recording were consistent with T-stellate cell morphology, as they presented planar dendrites parallel to the presumed path of auditory nerve fibers, and had highly branched dendritic tips (Oertel et al., 1990) (Figure A.2). Additionally, tdTomato positive boutons were present in nuclei where T-stellate cells are known to terminate, such as DCN (Figure A.3A), LSO (Figure A.3B), and ventral nucleus of the trapezoid body (VNTB) (Figure A.3C).

Globular bushy cells of the VCN send axons to the contralateral medial nucleus of the trapezoid body (MNTB) where they form large, visually distinct synapses called

calyces of Held (Smith et al., 1991). In the MNTB of Sst-Cre/tdTomato::GlyT2-GFP mice, an occasional calyx of Held was observed (Figure A.4). These calyces contact large inhibitory MNTB principal cells, which are glycinergic and well labeled in the GlyT2-GFP line (Albrecht et al., 2014) (Figure A.4A and C). TdTomato positive calyces on GFP positive principle cells were simple to visually identify due to their distinct morphology (see arrowheads in Figure A.4C). However, Sst-Cre/tdTomato sparsely labeled about 25% of these principal cells (Figure A.4A - B) and therefore it was not possible to distinguish if tdTomato positive calyces contacted them. Out of 683 principal cells that were both GFP-positive and tdTomato-negative, only 8 (1.6%) received a calyx (total of 865 cells counted from five 50 µm sections, $N = 1$ Sst-Cre/tdTomato::GlyT2-GFP mouse), suggesting that relatively few globular bushy cells are labeled in Sst-Cre/tdTomato mice. Thus, the majority of tdTomato labeled VCN cells were neither bushy cells nor inhibitory.

A.2 Electrophysiological properties suggest a majority of somatostatin-Cre positive posteroventral cochlear nucleus cells are sustained-chopper neurons

To further probe the identity of these Sst-Cre/tdTomato positive VCN cells, I conducted patch clamp recordings on them to assess their intrinsic firing properties in acute brain slices from 14-38 day old mice (methods were identical to sections 3.3 and 3.4). In sagittal sections of the VCN, I found that 81% (71 of 88) of tdTomato positive cells exhibited repetitive firing in response to steady depolarizing current steps (see examples in Figure A.5A). Hyperpolarizing current injections revealed a rectifying voltage response that was likely due to hyperpolarization-activated cyclic nucleotide-

gated (HCN) nonselective cation channels. Repetitive firing and HCN channels are characteristic of D- and T-stellate cells in the VCN (Rodrigues and Oertel, 2006). Cells that did not exhibit tonic firing responded only to the onset of suprathreshold depolarizing current steps with one or two action potentials, which is characteristic of bushy cells (Wu and Oertel, 1984). The VCN can be further divided into anterior (AVCN) and posterior regions (PVCN), with the AVCN containing a higher proportion of bushy cells than stellate cells (Romand and Avan, 1997). In coronal sections containing AVCN, only 1 of 13 (7.7%) neurons exhibited sustained firing, while in coronal sections containing PVCN, 11 of 19 (57.9%) neurons exhibited sustained firing, corresponding to the known distribution of bushy and T-stellate cells among these regions. These recordings suggests that Sst-Cre/tdTomato labels both stellate and bushy cells in the VCN, but the majority of cells labeled in PVCN are stellate.

There are three types of stellate cells in the VCN that respond to current injections with sustained action potentials: inhibitory D-stellate and L-stellate cells, and excitatory T-stellate cells (Oertel et al., 2011; Ngodup et al., 2020). Of the two inhibitory cell types, the smaller L-stellate cells are not genetically marked in the Sst-Cre/tdTomato line (Ngodup et al., 2020). Between D- and T-stellate cells, only T-stellate express nicotinic acetylcholine receptors (nAChR) and are therefore sensitive to cholinergic agonists (Fujino and Oertel, 2001). Bath application of 100 µM carbachol, an nAChR agonist, depolarized the resting membrane potential to spike threshold in 100% of tdTomato positive VCN cells tested (N = 8), resulting in sustained firing (Figure A.5B)—

confirming that the majority of Sst-Cre/tdTomato cells that exhibit tonic firing are T-stellate.

The *in vivo* spiking pattern of VCN cells can be classified by their characteristic responses to short tone bursts. T-stellate cells are associated with chopper responses, and bushy cells with primary-like responses (Rhode and Smith, 1986) (see examples in Figure A.6A). While these *in vivo* responses depend on acoustically driven synaptic input, they are also a reflection of each cell-type's intrinsic membrane properties. Peristimulus time histograms (PSTH) were created by injecting 150 repetitions of a 0.2 nA depolarizing current into tdTomato positive cells in acute *in vitro* brain sections. The PSTH of spike timing from repetitively firing cells closely resembled the chopping profile of T-stellate cells (Figure A.6B). Additionally, the first spike typically occurred within a millisecond of stimulus onset (see example in Figure A.6D), and subsequent spikes fired at a sustained rate throughout the duration of the stimulus (Figure A.6E). Overall, these spike pattern properties were consistent with the classification of a "sustained chopper" response and are associated with T-stellate cells (Rhode and Smith, 1986; Oertel et al., 2011). While the Sst-Cre/tdTomato mouse line also labels D-stellate cells (Figure A.1B), they can be easily be differentiated from T-stellate cells by their intrinsic membrane properties, neurotransmitter content (e.g. GlyT2-GFP mouse line), response to cholinergic agonists (Fujino and Oertel, 2001), and morphology (Oertel et al., 1990). Characterizing tdTomato positive VCN neurons was valuable for investigating to what extent they correspond to T-stellate cells, but it did not reveal to what extent T-stellate cells were labeled as a population.

A.3 Somatostatin-Cre labels a subset of inferior colliculus projecting T-stellate neurons

T-stellate are the only VCN cells known to send axons to the midbrain, and a large proportion of these axons terminate in the contralateral IC. To determine if the Sst-Cre mouse line labels all or only a subset of IC projecting T-stellate cells, a retrograde tract-tracer, green fluorescent latex microspheres (RetroBeads, Lumafluor), was pressure injected into the central nucleus of the IC in 22 day old Sst-Cre/tdTomato mice (Figure A.7A) (injection methods are described in Section 3.7). Four days post injection, the majority of retrograde label detected in the PVCN colocalized with tdTomato positive cell somata (Figure A.7B and C). This retrograde labeling of IC projecting VCN neurons demonstrated that Sst-Cre/tdTomato mice mark a subset of T-stellate neurons. However, fluorescent microspheres were difficult to visualize. This was likely because they were punctate in appearance (Figure A.7B and C) making them difficult to detect, and they were narrowly confined to the injection site (Figure A.7A) which likely diminished the overall quantity of retrogradely labeled T-stellate cells. To overcome these deficits in visualization, a 100 nanoliters of a retrograde adeno-associated virus (rgAAV2-CAG-GFP) was pressure injected into the central nucleus of the IC in 22 day old Sst-Cre/tdTomato mice (Figure A.8). The use of an AAV assured greater spread at the site of injection (Figure A.8A). Additionally, the expression of cytosolic fluorophore was more readily detected than punctate microspheres (Figure A.8B). Combined, these retrograde tract-tracing experiments determined that only a subset of T-stellate neurons are labeled in Sst-Cre/tdTomato mice.

In the context of this dissertation, the Sst-Cre mouse line was not ideal for specifically activating T-stellate inputs onto medial olivocochlear (MOC) neurons, as it would not be possible to differentiate these inputs from those of bushy cells. Additionally, many neurons were tdTomato positive in the ventral nucleus of the trapezoid body (VNTB) (data not shown), where MOC neuron somata reside. The ChAT-Cre mouse line described in Section 4.1 was essential for locating MOC neurons in acute brain sections for use with whole-cell recording. Because both of these lines label VNTB neurons, crossing them would not be ideal for locating MOC neurons. This means that visualization of MOC neurons in the Sst-Cre line would depend on retrograde tract tracing from the cochlea—a method which has proven to be unsuccessful for use with patch clamp electrophysiology in hearing aged rodents (Fujino et al., 1997). Nevertheless, this line is useful for visualizing a subset of VCN neurons in adult mice, virally driven tract tracing, and functional optogenetic studies of auditory circuitry. Moreover, it was recently used by Ngodup, Romero and Trussell (2020) to aid in the characterization of an overlooked but highly abundant inhibitory neuron in the VCN, the L-stellate cell.

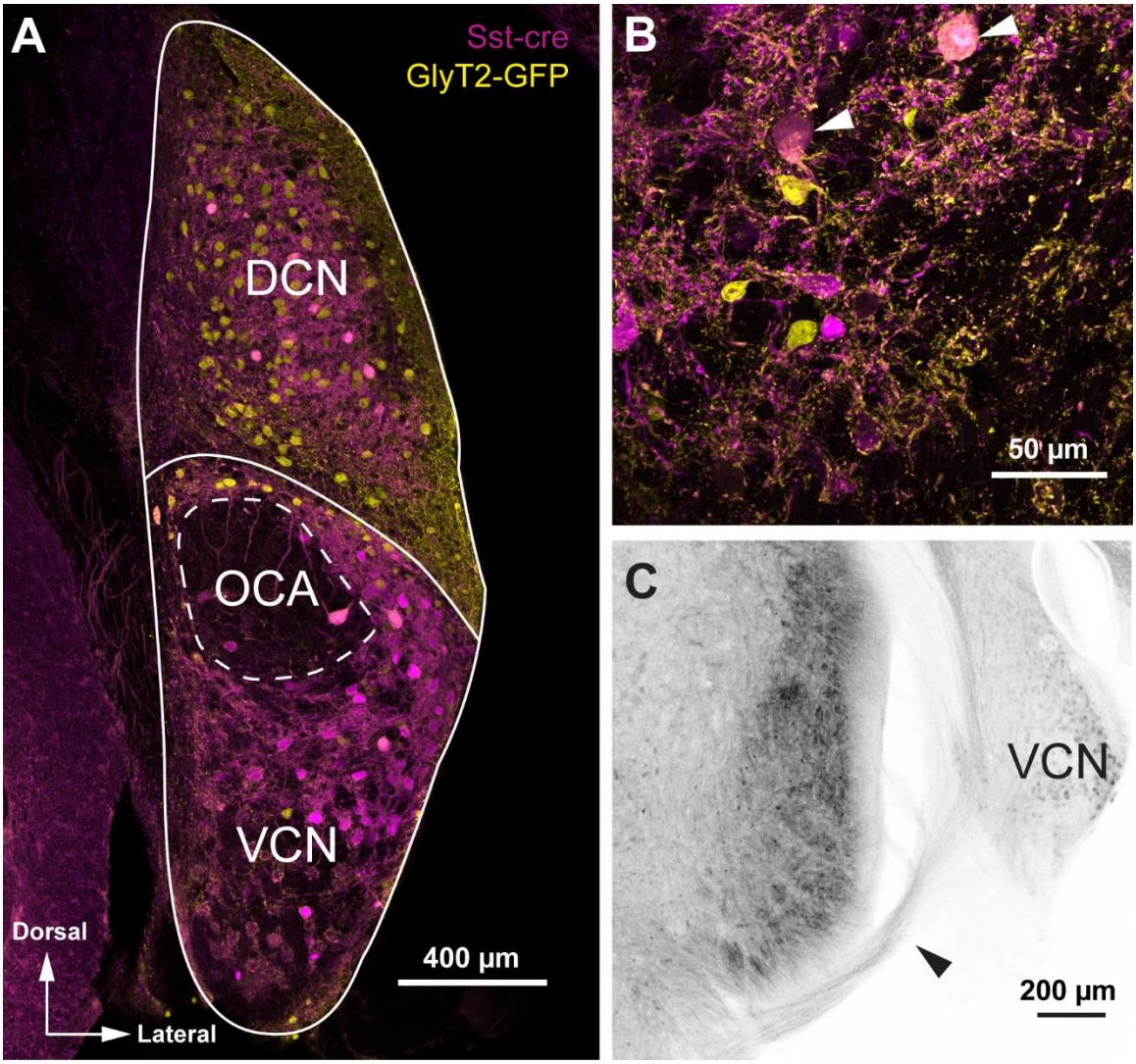

Figure A.1: Sst-Cre/tdTomato labels cells throughout the VCN.
(**A**) The Sst-Cre line was crossed to an Ai9 reporter to generate mice with tdTomato in Cre positive cells (Sst-Cre/tdTomato). This line was then crossed to a GlyT2-GFP transgenic line to double label for Cre and glycinergic neurons. In histological sections, Sst-Cre/tdTomato labeled cells were observed throughout the ventral cochlear nucleus (VCN) with only sparse somata observed in the dorsal cochlear nucleus (DCN). In the DCN, GlyT2-GFP somata were observed, and few GFP positive somata were seen in the VCN. Few GFP or tdTomato positive cells were observed in the octopus cell area (OCA).
(**B**) Sst-Cre/tdTomato and GlyT2-GFP labeled somata and neurite in the VCN. The majority of Sst-Cre/tdTomato neurons were negative for GFP, suggesting they are glutamatergic (excitatory). Cells that are double labeled are likely large inhibitory D-stellate neurons (white arrows).
(**C**) Axons of Cre expressing cells project from the VCN through the trapezoid body, consistent with T-stellate cell projections. TdTomato positive fibers can be seen in the trapezoid body (black arrow) of a coronal brain slice from an Sst-Cre/tdTomato mouse. The image was inverted and uncolored to better depict fibers of the trapezoid body. Black represents td-tomato fluorescence.

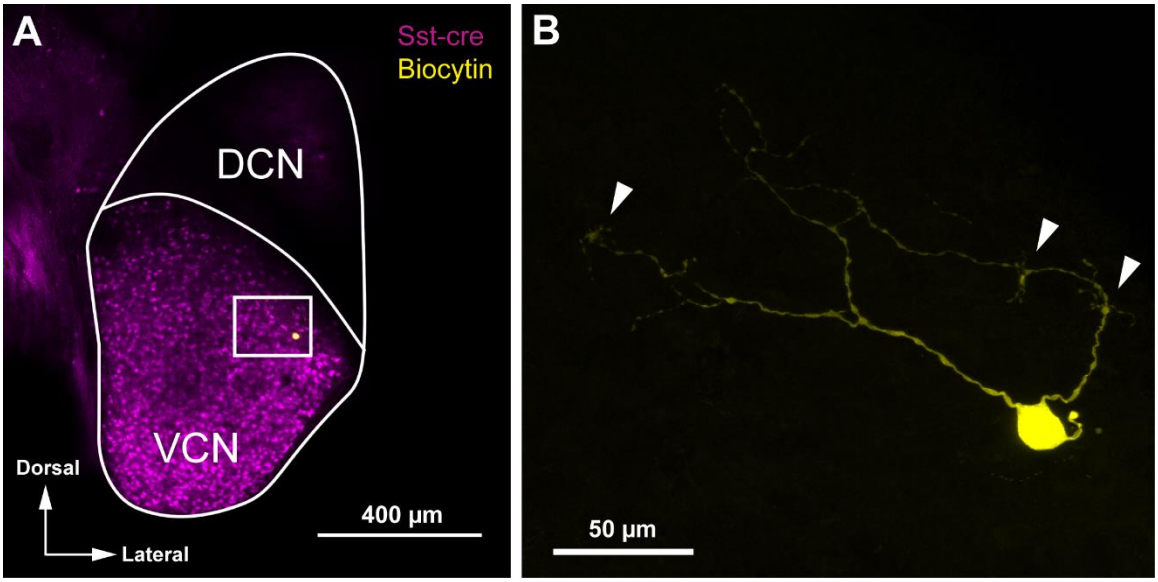

Figure A.2: TdTomato positive cells in the posteroventral cochlear nucleus are morphologically characteristic of T-stellate cells.
(**A**) Parasagittal section of the cochlear nucleus of an Sst-Cre/tdTomato mouse. A distinct population of neurons are positive for tdTomato in the VCN. A cell that was recorded from in whole-cell configuration was filled with biocytin and reacted against Alexa Fluor 488 conjugated streptavidin.
(**B**) This cell has a dendritic layout consistent with T-stellate morphology; planar dendrites aligned along the presumed path of auditory nerve fibers and prominent dendritic tufts (white arrows).

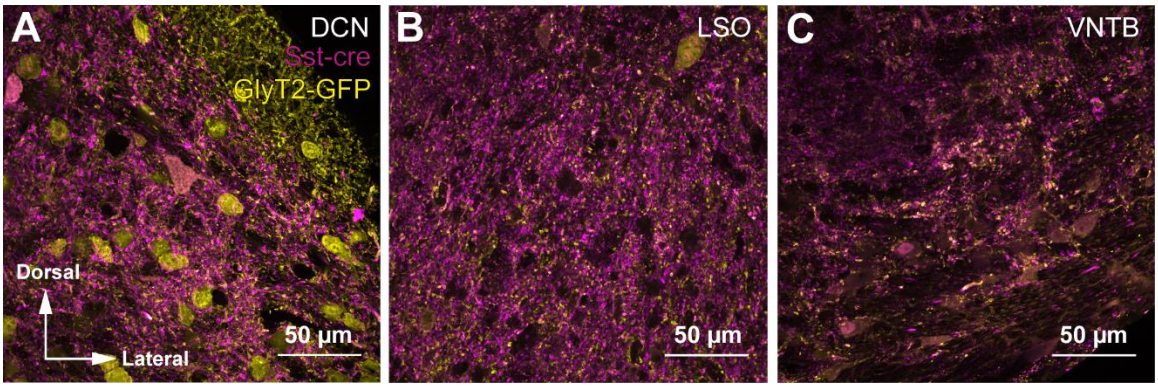

Figure A.3: TdTomato positive boutons are present in target nuclei of T-stellate cell projections. Non-glycinergic (GFP negative) tdTomato positive boutons are present in the dorsal cochlear nucleus (DCN, **A**), lateral superior olive (LSO, **B**), and ventral nucleus of the trapezoid body (VNTB, **C**), all nuclei where T stellate cell projections are known to terminate.

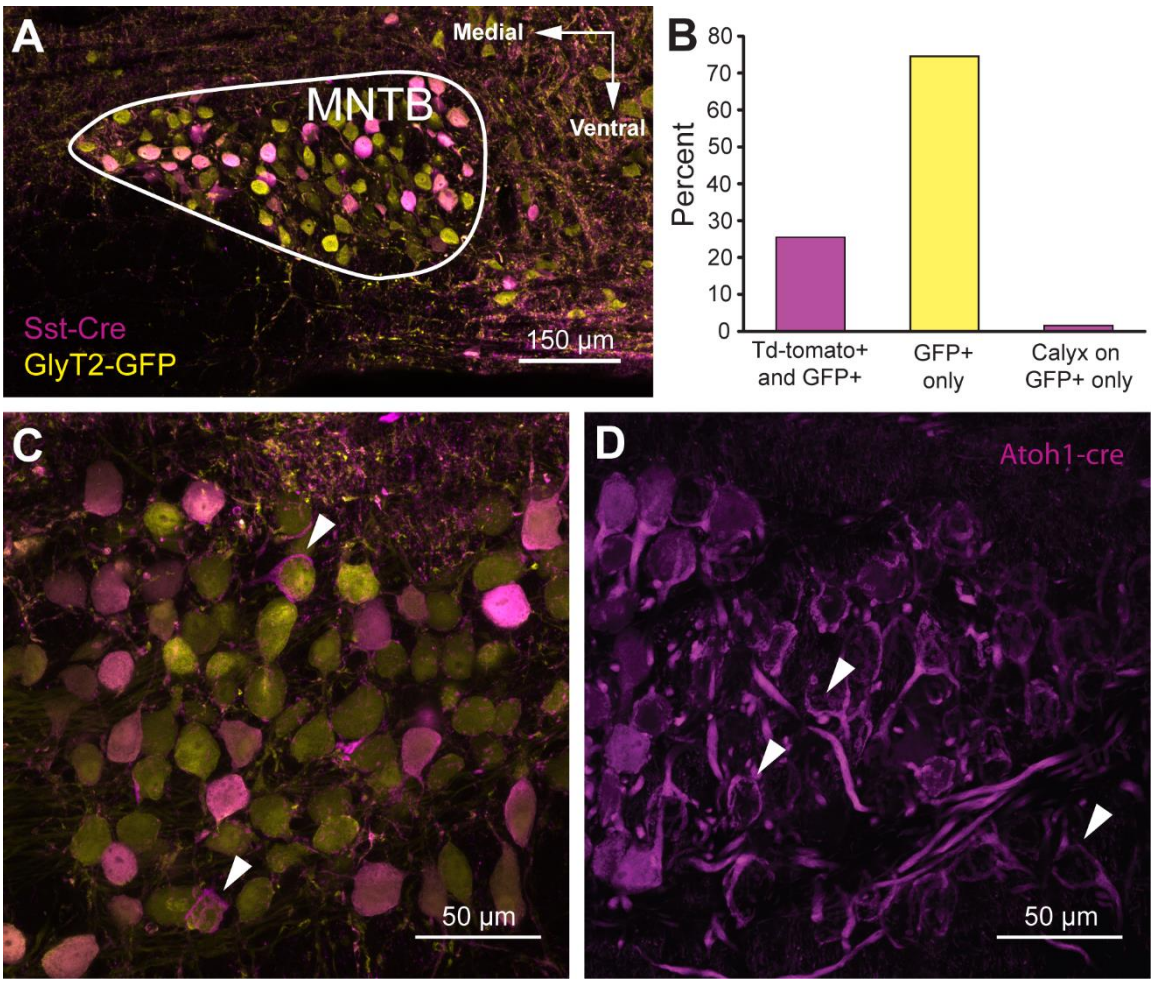

Figure A.4: Few principal cells of the medial nucleus of the trapezoid body, and few globular bushy cells, are tdTomato positive.
(**A**) Coronal section of the medial nucleus of the trapezoid body (MNTB) in an Sst-Cre/tdTomato mouse crossed with a GlyT2-GFP mouse. Glutamatergic globular bushy cells (GBC) of the VCN project their axons and synapse onto glycinergic MNTB principal neurons (GlyT2-GFP positive neurons in the MNTB) forming the visually distinct calyx of Held (see panel **C** and **D** arrowheads). Each MNTB neuron receives a GBC originating calyceal synapse. Some MNTB principal neuron soma are positive for both GlyT2-GFP and tdTomato.
(**B**) Bar graph depicting the percentage of MNTB principal neurons that are both tdTomato and GFP positive, or only GFP positive. All MNTB principal neurons are GFP positive, as they are glycinergic, and a total of 683 were counted. As it is not possible to accurately quantify a td-tomato positive calyx of Held synapse on a td-tomato positive MNTB principal neuron, only the percentage of td-tomato positive calyces onto td-tomato negative principal neurons was quantified.
(Continued on next page)

(**C**) The MNTB in Sst-Cre/tdTomato mice crossed with GlyT2-GFP mice. Few MNTB principal neurons receive a GBC originating calyx of Held (white arrows).
(**D**) For visual comparison with **C**. The MNTB in Atoh1-Cre/tdTomato mice, which express tdTomato in many calyces of Held (white arrows identify only three examples, however there many calyces in this micrograph).

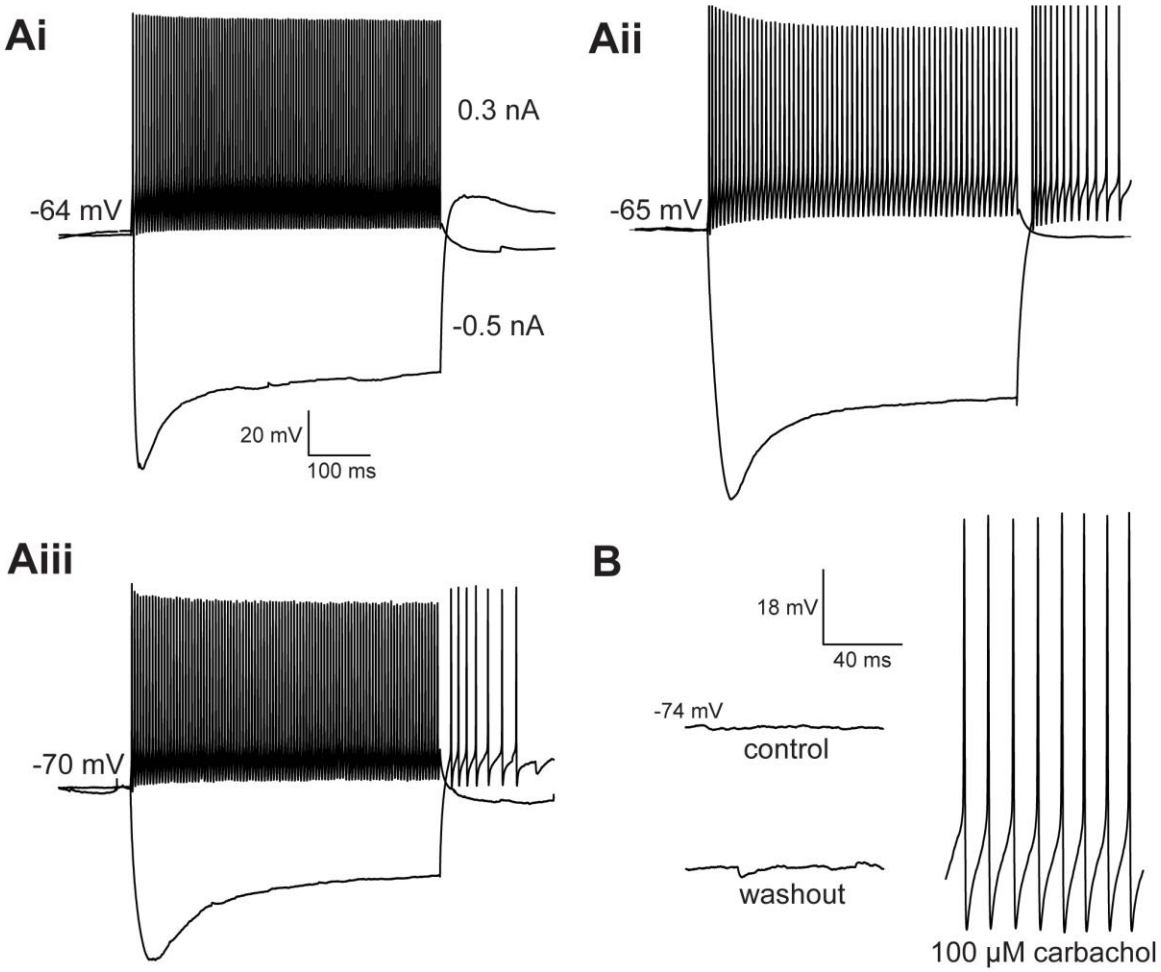

Figure A.5: Firing properties of tdTomato positive posteroventral nucleus cells resemble those of T-stellate cells.
(**Ai**), (**Aii**), and (**Aiii**) Three examples of current-clamp whole-cell patch recordings from Sst-Cre/tdTomato positive cells in the VCN (all traces are the same scale). The majority of randomized recordings from exhibited voltage responses to current injections that were characteristic of T stellate cells. Action potentials fired tonically with a sustained rate in response to depolarizing current injections (0.3 nA), and hyperpolarizing current injections (-0.5 nA) revealed a rectifying voltage response that was likely due to hyperpolarization-activated cyclic nucleotide-gated (HCN) nonselective cation channels. (**B**) There are two types of cells in the VCN that respond to current injections with sustained action potentials throughout the duration of a stimulus, inhibitory D-stellate and excitatory T-stellate cells. Of the two, only T-stellate express nicotinic acetylcholine receptors (nAChR) and are sensitive to cholinergic agonists. Application of 100 µM carbachol, an nAChR agonist, depolarized the resting membrane potential to action potential threshold in 8 out of 8 td-tomato positive VCN cells tested.

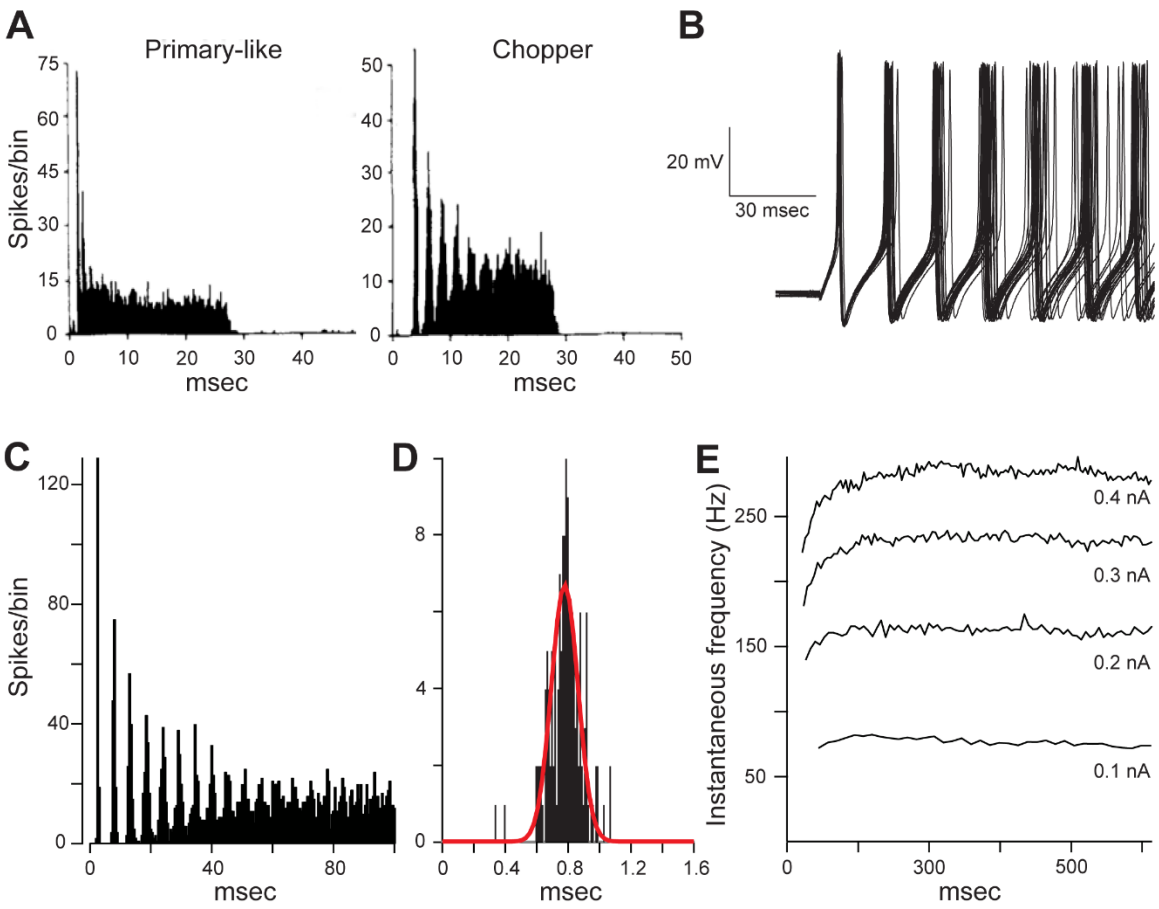

Figure A.6: TdTomato positive posteroventral cochlear nucleus cells produce a "sustained-chopper" response to depolarizing current injections.
(**A**) Two examples of in vivo peristimulus time histograms (PSTH) from VCN neurons in young adult cats. Each histogram was constructed from intracellular recordings in response to 250 repetitions of a 25 millisecond tone at the characteristic frequency of the cell. Spike bins were 3.9 milliseconds. Adapted from Rhode and Smith, Journal of Neurophysiology, 1986, with permission. Chopper response on the right is characteristic of T-stellate cells.
(**B**) In an Sst-Cre positive VCN neuron, twenty applications of 0.2 nA current injections were applied, which generate action potentials with increasing temporal jitter.
(**C**) In the cell shown in B, a chopper PSTH was apparent (150 repetitions of a 0.2 nA depolarizing current injection). Spike bins are 0.5 milliseconds.
(**D**) Depicts the latency of the first action potential from A., using 0.02 millisecond bins. The standard deviation was 85 ± 12 microseconds, measured with a Gaussian curve fit (red). This fast response to depolarizing stimuli enables this cell to quickly convey the onset of auditory information.
(**E**) Plot of instantaneous frequency of each action potential throughout the duration of depolarizing stimuli ranging 100-400 pA. The instantaneous frequency is sustained throughout the duration of the stimulus. Thus, these neurons are considered "sustained-choppers".

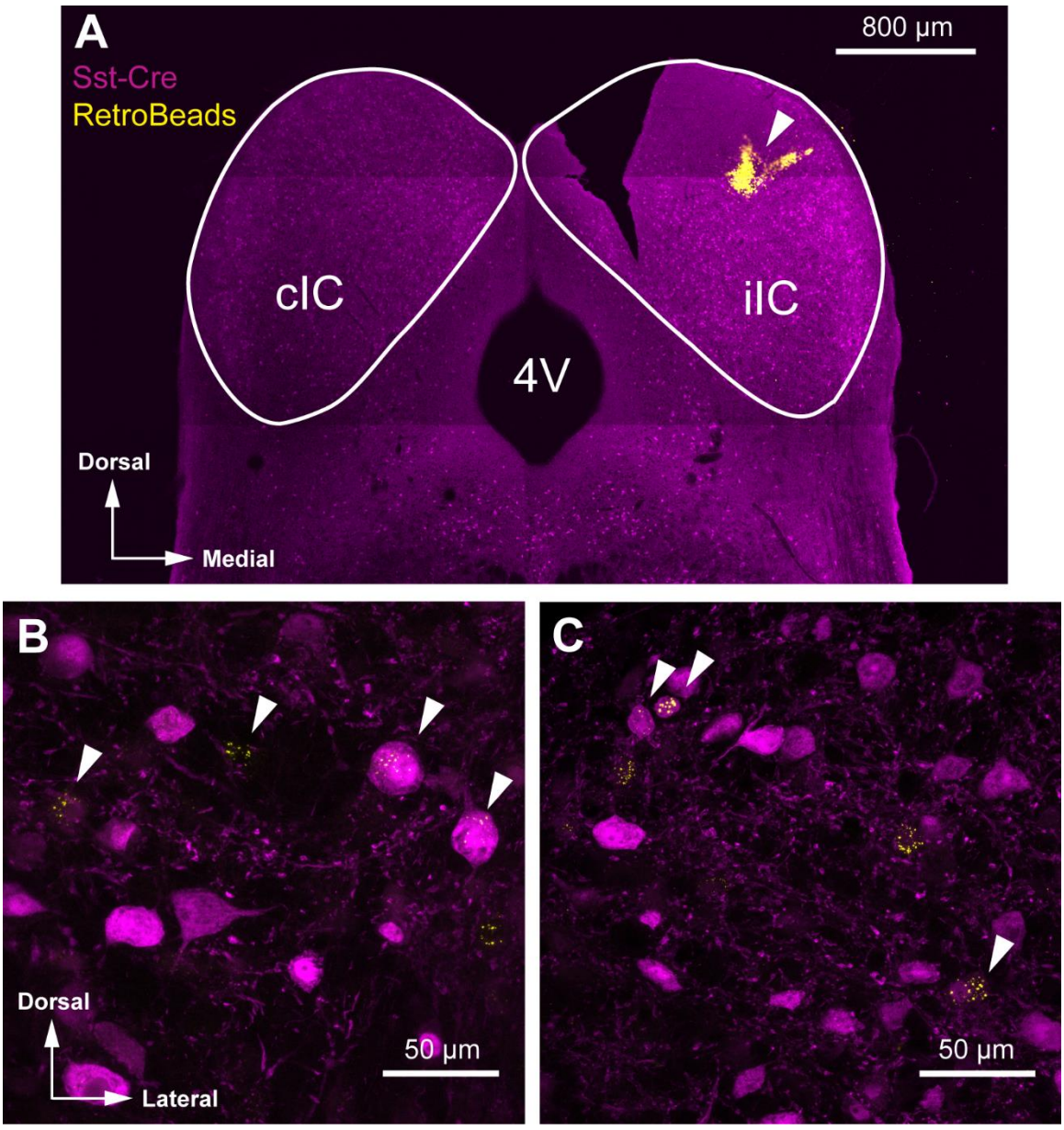

Figure A.7: Retrograde tracer originating from the inferior colliculus colocalizes with tdTomato positive neurons in the ventral cochlear nucleus.
(**A**) An inferior colliculus injection site (white arrow) of Lumafluor green RetroBeads (50 nL) in an Sst-Cre/tdTomato mouse. Abbreviations: fourth ventricle (4V), ipsilateral inferior colliculus (iIC), contralateral inferior colliculus (cIC).
(**B**) Green RetroBeads in the pVCN contralateral to the injection site in **A**. The majority of tracer in the pVCN colocalized with tdTomato positive cells (white arrows). This indicated that the colocalized cells are T-stellate, as their axons terminate in the contralateral inferior colliculus (see Figure 1), the site of tracer injection. No tracer was detected in the VCN ipsilateral to the injection site.
(**C**) Green RetroBeads in the VCN contralateral to the injection site in a second mouse.

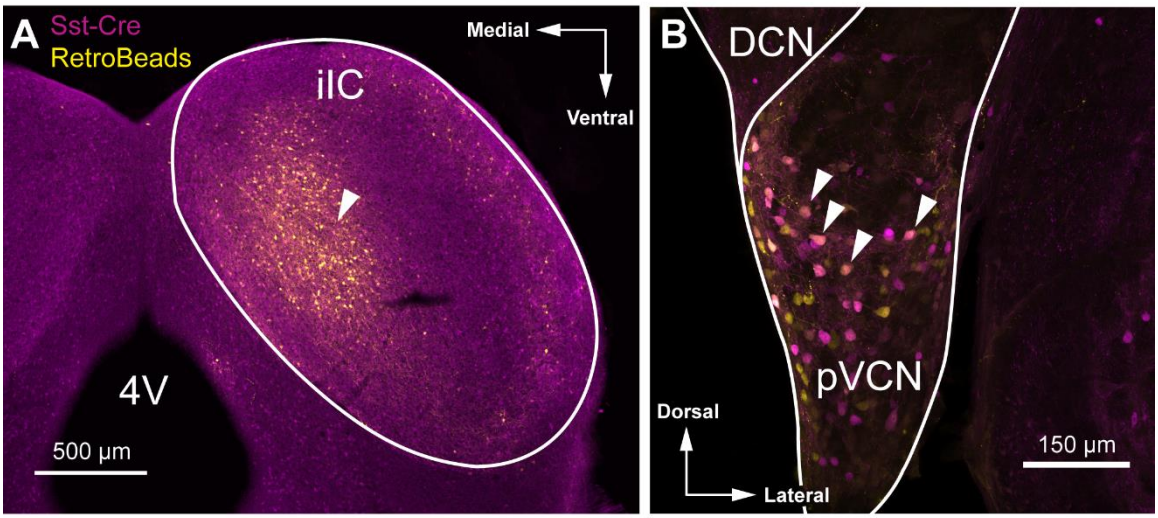

Figure A.8: Retrograde adeno-associated virus originating from the inferior colliculus colocalizes with tdTomato positive neurons in the ventral cochlear nucleus.
(**A**) An inferior colliculus injection site (white arrow) of the retro- and anterograde rgAAV2-CAG-GFP (100 nL) in an Sst-Cre/tdTomato mouse. Abbreviations: fourth ventricle (4V), ipsilateral inferior colliculus (iIC). Scale bar, 500 µm.
(**B**) Infected neurons in the pVCN contralateral to the injection site in **A** expressed GFP. In many neurons, GFP colocalized with tdTomato positive cells (white arrows point to four examples, but there are many co-labeled cells in this micrograph). This indicates that the colocalized cells are T-stellate.

REFERENCES

Adams JC (1979) Ascending projections to the inferior colliculus. J Comp Neurol 183:519–538.

Aedo C, Tapia E, Pavez E, Elgueda D, Delano PH, Robles L (2015) Stronger efferent suppression of cochlear neural potentials by contralateral acoustic stimulation in awake than in anesthetized chinchilla. Front Syst Neurosci 9.

Albrecht O, Dondzillo A, Mayer F, Thompson JA, Klug A (2014) Inhibitory projections from the ventral nucleus of the trapezoid body to the medial nucleus of the trapezoid body in the mouse. Front Neural Circuits 8.

Arnesen AR (1984) Fibre population of the vestibulocochlear anastomosis in humans. Acta Otolaryngol (Stockh) 98:501–518.

Attanasio G, Barbara M, Buongiorno G, Cordier A, Mafera B, Piccoli F, Nostro G, Filipo R (1999) Protective Effect of the Cochlear Efferent System During Noise Exposure. Ann N Y Acad Sci 884:361–367.

Backus BC, Guinan JJ (2006) Time-course of the human medial olivocochlear reflex. J Acoust Soc Am 119:2889–2904.

Bedbrook CN, Yang KK, Robinson JE, Mackey ED, Gradinaru V, Arnold FH (2019) Machine learning-guided channelrhodopsin engineering enables minimally invasive optogenetics. Nat Methods 16:1176–1184.

Benson TE, Brown MC (1996) Synapses from medial olivocochlear branches in the inferior vestibular nucleus. J Comp Neurol 372:176–188.

Blackburn CC, Sachs MB, Sachs B (1989) Classification of unit types in the anteroventral cochlear nucleus: PST histograms and regularity analysis. J Neurophysiol 62:1303–1329.

Bowie D, Mayer ML (1995) Inward rectification of both AMPA and kainate subtype glutamate receptors generated by polyamine-mediated ion channel block. Neuron 15:453–462.

Boyden ES, Zhang F, Bamberg E, Nagel G, Deisseroth K (2005) Millisecond-timescale, genetically targeted optical control of neural activity. Nat Neurosci 8:1263–1268.

Brenowitz S, Trussell LO (2001) Maturation of synaptic transmission at end-bulb synapses of the cochlear nucleus. J Neurosci 21:9487–9498.

Brown GJ, Ferry RT, Meddis R (2010) A computer model of auditory efferent suppression: implications for the recognition of speech in noise. J Acoust Soc Am 127:943–954.

Brown MC (1987) Morphology of labeled afferent fibers in the guinea pig cochlea. J Comp Neurol 260:591–604.

Brown MC (1989) Morphology and response properties of single olivocochlear fibers in the guinea pig. Hear Res 40:93–109.

Brown MC (1993) Fiber pathways and branching patterns of biocytin-labeled olivocochlear neurons in the mouse brainstem. J Comp Neurol 337:600–613.

Brown MC (2014) Single-unit labeling of medial olivocochlear neurons: the cochlear frequency map for efferent axons. J Neurophysiol 111:2177–2186.

Brown MC (2016) Recording and labeling at a site along the cochlea shows alignment of medial olivocochlear and auditory nerve tonotopic mappings. J Neurophysiol 115:1644–1653.

Brown MC, Ledwith JV (1990) Projections of thin (type-II) and thick (type-I) auditory-nerve fibers into the cochlear nucleus of the mouse. Hear Res 49:105–118.

Brown MC, Levine JL (2008) Dendrites of medial olivocochlear neurons in mouse. Neuroscience 154:147–159.

Brown MC, Liberman MC, Benson TE, Ryugo DK (1988) Brainstem branches from olivocochlear axons in cats and rodents. J Comp Neurol 278:591–603.

Brown MC, Mukerji S, Drottar M, Windsor AM, Lee DJ (2013) Identification of inputs to olivocochlear neurons using transneuronal labeling with pseudorabies virus (PRV). JARO - J Assoc Res Otolaryngol 14:703–717.

Brown MC, Nuttall AL (1984) Efferent control of cochlear inner hair cell responses in the guinea-pig. J Physiol 354:625–646.

Brown MC, Nuttall AL, Masta RI (1983) Intracellular recordings from cochlear inner hair cells: effects of stimulation of the crossed olivocochlear efferents. Science 222:69–72.

Brownell WE, Bader CR, Bertrand D, de Ribaupierre Y (1985) Evoked mechanical responses of isolated cochlear outer hair cells. Science 227:194–196.

Buño W (1978) Auditory nerve fiber activity influenced by contralateral ear sound stimulation. Exp Neurol 59:62–74.

Caicedo A, Herbert H (1993) Topography of descending projections from the inferior colliculus to auditory brainstem nuclei in the rat. J Comp Neurol 328:377–392.

Campbell JP, Henson MM (1988) Olivocochlear neurons in the brainstem of the mouse. Hear Res 35:271–274.

Cant NB (2019) Axon Trajectories in the Auditory Brainstem. In: The Oxford Handbook of the Auditory Brainstem (Kandler K, ed), pp 472–502. Oxford University Press.

Cant NB, Oliver DL (2018) Overview of Auditory Projection Pathways and Intrinsic Microcircuits. In: The Mammalian Auditory Pathways (Oliver DL, Cant NB, Fay RR, Popper AN, eds), pp 7–39 Springer Handbook of Auditory Research. Cham: Springer International Publishing.

Chambers AR, Hancock KE, Maison SF, Liberman MC, Polley DB (2012) Sound-Evoked Olivocochlear Activation in Unanesthetized Mice. J Assoc Res Otolaryngol 13:209–217.

Chumak T, Bohuslavova R, Macova I, Dodd N, Buckiova D, Fritzsch B, Syka J, Pavlinkova G (2016) Deterioration of the Medial Olivocochlear Efferent System Accelerates Age-Related Hearing Loss in Pax2-Isl1 Transgenic Mice. Mol Neurobiol 53:2368–2383.

Clause A, Kim G, Sonntag M, Weisz CJC, Vetter DE, Rűbsamen R, Kandler K (2014) The Precise Temporal Pattern of Prehearing Spontaneous Activity Is Necessary for Tonotopic Map Refinement. Neuron 82:822–835.

Clements JD, Bekkers JM (1997) Detection of spontaneous synaptic events with an optimally scaled template. Biophys J 73:220–229.

Cody AR, Johnstone BM (1982) Acoustically evoked activity of single efferent neurons in the guinea pig cochlea. J Acoust Soc Am 72:280–282.

Coomes DP, Schofield BR (2007) Projections from auditory cortex contact ascending pathways that originate in the superior olive and inferior colliculus. Hear Res 232:67–77.

Cooper NP, Guinan JJ (2003) Separate mechanical processes underlie fast and slow effects of medial olivocochlear efferent activity. J Physiol 548:307–312.

Corey DP, Hudspeth AJ (1979) Ionic basis of the receptor potential in a vertebrate hair cell. Nature 281:675–677.

Dallos P (2008) Cochlear amplification, outer hair cells and prestin. Curr Opin Neurobiol 18:370–376.

Darrow KN, Benson TE, Brown MC (2012) Planar multipolar cells in the cochlear nucleus project to medial olivocochlear neurons in mouse. J Comp Neurol 520:1365–1375.

Darrow KN, Maison SF, Liberman MC (2007) Selective removal of lateral olivocochlear efferents increases vulnerability to acute acoustic injury. J Neurophysiol 97:1775–1785.

Darrow KN, Simons EJ, Dodds L, Liberman MC (2006) Dopaminergic innervation of the mouse inner ear: Evidence for a separate cytochemical group of cochlear efferent fibers. J Comp Neurol 498:403–414.

de Boer J, Thornton ARD, Krumbholz K (2012) What is the role of the medial olivocochlear system in speech-in-noise processing? J Neurophysiol 107:1301–1312.

De Venecia RK, Liberman MC, Guinan JJ, Brown MC, Ronald K, Al VET, De Venecia RK, Liberman MC, Guinan JJ, Brown MC (2005) Medial olivocochlear reflex interneurons are located in the posteroventral cochlear nucleus: A kainic acid lesion study in guinea pigs. J Comp Neurol 487:345–360.

Delano PH, Elgueda D, Hamame CM, Robles L (2007) Selective Attention to Visual Stimuli Reduces Cochlear Sensitivity in Chinchillas. J Neurosci 27:4146–4153.

Donevan SD, Rogawski MA (1995) Intracellular polyamines mediate inward rectification of Ca(2+)-permeable alpha-amino-3-hydroxy-5-methyl-4-isoxazolepropionic acid receptors. Proc Natl Acad Sci 92:9298–9302.

Doucet JR, Ross AT, Gillespie MB, Ryugo DK (1999) Glycine immunoreactivity of multipolar neurons in the ventral cochlear nucleus which project to the dorsal cochlear nucleus. J Comp Neurol 408:515–531.

Doucet JR, Ryugo DK (2003) Axonal pathways to the lateral superior olive labeled with biotinylated dextran amine injections in the dorsal cochlear nucleus of rats. J Comp Neurol 461:452–465.

Dragicevic CD, Aedo C, León A, Bowen M, Jara N, Terreros G, Robles L, Delano PH (2015) The olivocochlear reflex strength and cochlear sensitivity are

independently modulated by auditory cortex microstimulation. J Assoc Res Otolaryngol JARO 16:223–240.

Ehret G, Moffat AJM (1985) Inferior colliculus of the house mouse. J Comp Physiol A 156:619–635.

Elgueda D, Delano PH, Robles L (2011) Effects of electrical stimulation of olivocochlear fibers in cochlear potentials in the chinchilla. J Assoc Res Otolaryngol JARO 12:317–327.

Eybalin M (1993) Neurotransmitters and neuromodulators of the mammalian cochlea. Physiol Rev 73:309–373.

Farhadi A, Jennings SG, Strickland EA, Carney LH (2021) A closed-loop gain-control feedback model for the medial efferent system of the descending auditory pathway. ICASSP. In press.

Fatt P, Katz B (1952) Spontaneous subthreshold activity at motor nerve endings. J Physiol 117:109–128.

Faye-Lund H (1986) Projection from the inferior colliculus to the superior olivary complex in the albino rat. Anat Embryol (Berl) 175:35–52.

Ferragamo MJ, Golding NL, Oertel D (1998) Synaptic Inputs to Stellate Cells in the Ventral Cochlear Nucleus. J Neurophysiol 79:51–63.

Fex J (1962) Auditory activity in centrifugal and centripetal cochlear fibres in cat. A study of a feedback system. Acta Physiol Scand Suppl 189:1–68.

Frank MM, Goodrich LV (2018) Talking back: Development of the olivocochlear efferent system. Wiley Interdiscip Rev Dev Biol 7:1–20.

Fuchs PA, Murrow BW (1992a) A novel cholinergic receptor mediates inhibition of chick cochlear hair cells. Proc Biol Sci 248:35–40.

Fuchs PA, Murrow BW (1992b) Cholinergic inhibition of short (outer) hair cells of the chick's cochlea. J Neurosci Off J Soc Neurosci 12:800–809.

Fuente A (2015) The olivocochlear system and protection from acoustic trauma: a mini literature review. Front Syst Neurosci 9.

Fujino K, Koyano K, Ohmori H (1997) Lateral and Medial Olivocochlear Neurons Have Distinct Electrophysiological Properties in the Rat Brain Slice. J Neurophysiol 77:2788–2804.

Fujino K, Oertel D (2001) Cholinergic modulation of stellate cells in the mammalian ventral cochlear nucleus. J Neurosci Off J Soc Neurosci 21:7372–7383.

Galambos R (1956) Supression of Auditory Nerve Activity by Stimulation of Efferent Fibers to Cochlea. J Neurophysiol 19:424–437.

Gardner SM, Trussell LO, Oertel D (1999) Time Course and Permeation of Synaptic AMPA Receptors in Cochlear Nuclear Neurons Correlate with Input. J Neurosci 19:8721–8729.

Gardner SM, Trussell LO, Oertel D (2001) Correlation of AMPA Receptor Subunit Composition with Synaptic Input in the Mammalian Cochlear Nuclei. J Neurosci 21:7428–7437.

Geiger JRP, Melcher T, Koh D-S, Sakmann B, Seeburg PH, Jonas P, Monyer H (1995) Relative abundance of subunit mRNAs determines gating and Ca2+ permeability of AMPA receptors in principal neurons and interneurons in rat CNS. Neuron 15:193–204.

Gifford ML, Guinan JJ (1987) Effects of electrical stimulation of medial olivocochlear neurons on ipsilateral and contralateral cochlear responses. Hear Res 29:179–194.

Glowatzki E (2000) Cholinergic Synaptic Inhibition of Inner Hair Cells in the Neonatal Mammalian Cochlea. Science 288:2366–2368.

Golding NL, Ferragamo MJ, Oertel D (1999) Role of Intrinsic Conductances Underlying Responses to Transients in Octopus Cells of the Cochlear Nucleus. J Neurosci 19:2897–2905.

Gong S, Zheng C, Doughty ML, Losos K, Didkovsky N, Schambra UB, Nowak NJ, Joyner A, Leblanc G, Hatten ME, Heintz N (2003) A gene expression atlas of the central nervous system based on bacterial artificial chromosomes. Nature 425:917–925.

Goutman JD, Fuchs PA, Glowatzki E (2005) Facilitating efferent inhibition of inner hair cells in the cochlea of the neonatal rat. J Physiol 566:49–59.

Groff JA, Liberman MC (2003) Modulation of Cochlear Afferent Response by the Lateral Olivocochlear System: Activation Via Electrical Stimulation of the Inferior Colliculus. J Neurophysiol 90:3178–3200.

Guinan JJ (1996) Physiology of Olivocochlear Efferents. In: The Cochlea (Dallos P, Popper AN, Fay RR, eds), pp 435–502 Springer Handbook of Auditory Research. New York, NY: Springer New York.

Guinan JJ (2006) Olivocochlear efferents: anatomy, physiology, function, and the measurement of efferent effects in humans. Ear Hear 27:589–607.

Guinan JJ (2010) Cochlear efferent innervation and function. Curr Opin Otolaryngol Head Neck Surg 18:447–453.

Guinan JJ (2011) Physiology of the Medial and Lateral Olivocochlear Systems. In: Auditory and Vestibular Efferents (Ryugo DK, Fay RR, eds), pp 39–81 Springer Handbook of Auditory Research. New York, NY: Springer.

Guinan JJ (2018) Olivocochlear efferents: Their action, effects, measurement and uses, and the impact of the new conception of cochlear mechanical responses. Hear Res 362:38–47.

Guinan JJ, Warr WB, Norris BE (1983) Differential olivocochlear projections from lateral versus medial zones of the superior olivary complex. J Comp Neurol 221:358–370.

Guinan JJ, Warr WB, Norris BE (1984) Topographic organization of the olivocochlear projections from the lateral and medial zones of the superior olivary complex. J Comp Neurol 226:21–27.

Guitton MJ, Avan P, Puel J-L, Bonfils P (2004) Medial olivocochlear efferent activity in awake guinea pigs. NeuroReport 15:1379–1382.

Gunaydin LA, Yizhar O, Berndt A, Sohal VS, Deisseroth K, Hegemann P (2010) Ultrafast optogenetic control. Nat Neurosci 13:387–392.

Hansel C, Linden DJ (2000) Long-Term Depression of the Cerebellar Climbing Fiber–Purkinje Neuron Synapse. Neuron 26:473–482.

Horváth M, Kraus KS, Illing R-B (2000) Olivocochlear neurons sending axon collaterals into the ventral cochlear nucleus of the rat. J Comp Neurol 422:95–105.

Horvath M, Ribari O, Gabor R, Toth IE, Boldogkoi Z, Palkovits M (2003) Intracochlear injection of pseudorabies virus labels descending auditory and monoaminerg projections to olivocochlear cells in guinea pig. Eur J Neurosci 18:1439–1447.

Housley GD, Ashmore JF (1991) Direct measurement of the action of acetylcholine on isolated outer hair cells of the guinea pig cochlea. Proc R Soc Lond B Biol Sci 244:161–167.

Hudspeth AJ (1989) How the ear's works work. Nature 341:397–404.

Hudspeth AJ, Jacobs R (1979) Stereocilia mediate transduction in vertebrate hair cells (auditory system/cilium/vestibular system). Proc Natl Acad Sci U S A 76:1506–1509.

Jackman SL, Beneduce BM, Drew IR, Regehr WG (2014) Achieving High-Frequency Optical Control of Synaptic Transmission. J Neurosci 34:7704–7714.

Jia Y, Zhao Y, Kusakizako T, Wang Y, Pan C, Zhang Y, Nureki O, Hattori M, Yan Z (2020) TMC1 and TMC2 Proteins Are Pore-Forming Subunits of Mechanosensitive Ion Channels. Neuron 105:310-321.e3.

Katz E, Elgoyhen AB, Gómez-Casati ME, Knipper M, Vetter DE, Fuchs PA, Glowatzki E (2004) Developmental regulation of nicotinic synapses on cochlear inner hair cells. J Neurosci Off J Soc Neurosci 24:7814–7820.

Katz E, Verbitsky M, Rothlin CV, Vetter DE, Heinemann SF, Elgoyhen a B (2000) High calcium permeability and calcium block of the alpha9 nicotinic acetylcholine receptor. Hear Res 141:117–128.

Kawase T, Liberman MC (1993) Antimasking effects of the olivocochlear reflex. I. Enhancement of compound action potentials to masked tones. J Neurophysiol 70:2519–2532.

Kim DO, Dorn PA, Neely ST, Gorga MP (2001) Adaptation of distortion product otoacoustic emission in humans. J Assoc Res Otolaryngol JARO 2:31–40.

Klapoetke NC et al. (2014) Independent optical excitation of distinct neural populations. Nat Methods 11:338–346.

Koike-Tani M, Saitoh N, Takahashi T (2005) Mechanisms underlying developmental speeding in AMPA-EPSC decay time at the calyx of Held. J Neurosci 25:199–207.

Kong J-H, Adelman JP, Fuchs P a (2008) Expression of the SK2 calcium-activated potassium channel is required for cholinergic function in mouse cochlear hair cells. J Physiol 586:5471–5485.

Köppl C (2011) Evolution of the Octavolateral Efferent System. In: Auditory and Vestibular Efferents (Ryugo DK, Fay RR, eds), pp 217–259 Springer Handbook of Auditory Research. New York, NY: Springer.

Koyano K, Ohmori H (1996) Cellular approach to auditory signal transmission. Jpn J Physiol 46:289–310.

Kujawa SG, Liberman MC (1997) Conditioning-Related Protection From Acoustic Injury: Effects of Chronic Deefferentation and Sham Surgery. J Neurophysiol 78:3095–3106.

Kujawa SG, Liberman MC (2009) Adding insult to injury: cochlear nerve degeneration after “temporary” noise-induced hearing loss. J Neurosci Off J Soc Neurosci 29:14077–14085.

Kumar UA, Vanaja CS (2004) Functioning of olivocochlear bundle and speech perception in noise. Ear Hear 25:142–146.

Kuo SP, Lu H-W, Trussell LO (2012) Intrinsic and synaptic properties of vertical cells of the mouse dorsal cochlear nucleus. J Neurophysiol 108:1186–1198.

Kuwada S, Batra R, Yin TCT, Oliver DL, Haberly LB, Stanford TR (1997) Intracellular Recordings in Response to Monaural and Binaural Stimulation of Neurons in the Inferior Colliculus of the Cat. J Neurosci 17:7565–7581.

Larsen E, Liberman MC (2010) Contralateral cochlear effects of ipsilateral damage: no evidence for interaural coupling. Hear Res 260:70–80.

Le Prell C, Dolan D, Schacht J, Miller J, Lomax M, Altschuler R (2003) Pathways for protection from noise induced hearing loss. Noise Health 5:1–17.

Le TN, Straatman LV, Lea J, Westerberg B (2017) Current insights in noise-induced hearing loss: a literature review of the underlying mechanism, pathophysiology, asymmetry, and management options. J Otolaryngol - Head Neck Surg 46.

Leijon S, Magnusson AK (2014) Physiological Characterization of Vestibular Efferent Brainstem Neurons Using a Transgenic Mouse Model Alsina B, ed. PLoS ONE 9:e98277.

LeMasurier M, Gillespie PG (2005) Hair-Cell Mechanotransduction and Cochlear Amplification. Neuron 48:403–415.

Liberman MC (1980) Efferent synapses in the inner hair cell area of the cat cochlea: an electron microscopic study of serial sections. Hear Res 3:189–204.

Liberman MC (1988a) Response properties of cochlear efferent neurons: monaural vs. binaural stimulation and the effects of noise. J Neurophysiol 60:1779–1798.

Liberman MC (1988b) Physiology of cochlear efferent and afferent neurons: Direct comparisons in the same animal. Hear Res 34:179–191.

Liberman MC (1990) Effects of chronic cochlear de-efferentation on auditory-nerve response. Hear Res 49:209–223.

Liberman MC, Brown MC (1986) Physiology and anatomy of single olivocochlear neurons in the cat. Hear Res 24:17–36.

Liberman MC, Puria S, Guinan JJ (1996) The ipsilaterally evoked olivocochlear reflex causes rapid adaptation of the 2f1-f2 distortion product otoacoustic emission. J Acoust Soc Am 99:3572–3584.

Lilaonitkul W, Guinan JJ (2009) Human Medial Olivocochlear Reflex: Effects as Functions of Contralateral, Ipsilateral, and Bilateral Elicitor Bandwidths. JARO J Assoc Res Otolaryngol 10:459–470.

Lin JY, Lin MZ, Steinbach P, Tsien RY (2009) Characterization of Engineered Channelrhodopsin Variants with Improved Properties and Kinetics. Biophys J 96:1803–1814.

Lopez-poveda EA, Eustaquio-martín A, Stohl JS, Wolford RD, Schatzer R, Wilson BS (2016) A Binaural Cochlear Implant Sound Coding Strategy Inspired by the Contralateral Medial Olivocochlear Reflex. Ear Hear:1–11.

Lujan B, Dagostin A, Von Gersdorff H (2019) Presynaptic diversity revealed by Ca2+-permeable AMPA receptors at the calyx of held synapse. J Neurosci.

Madisen L, Zwingman TA, Sunkin SM, Oh SW, Zariwala HA, Gu H, Ng LL, Palmiter RD, Hawrylycz MJ, Jones AR, Lein ES, Zeng H (2010) A robust and high-throughput Cre reporting and characterization system for the whole mouse brain. Nat Neurosci 13:133–140.

Magleby KL (1987) Short-term changes in synaptic efficacy. In: Synaptic function (Edelman GM, Gall WE, Cowan WM, eds). N Y Wiley:21–56.

Magleby KL, Zengel JE (1976) Augmentation: A process that acts to increase transmitter release at the frog neuromuscular junction. J Physiol 257:449–470.

Maison SF, Adams JC, Liberman MC (2003) Olivocochlear innervation in the mouse: Immunocytochemical maps, crossed versus uncrossed contributions, and transmitter colocalization. J Comp Neurol 455:406–416.

Maison SF, Liu X-P, Eatock RA, Sibley DR, Grandy DK, Liberman MC (2012) Dopaminergic Signaling in the Cochlea: Receptor Expression Patterns and Deletion Phenotypes. J Neurosci 32:344–355.

Maison SF, Usubuchi H, Liberman MC (2013) Efferent feedback minimizes cochlear neuropathy from moderate noise exposure. J Neurosci Off J Soc Neurosci 33:5542–5552.

Malmierca MS (2003) The structure and physiology of the rat auditory system: an overview. Int Rev Neurobiol 56:147–211.

Messing DP, Delhorne L, Bruckert E, Braida LD, Ghitza O (2009) A non-linear efferent-inspired model of the auditory system; matching human confusions in stationary noise. Speech Commun 51:668–683.

Mishra SK, Lutman ME (2014) Top-down influences of the medial olivocochlear efferent system in speech perception in noise. PloS One 9:e85756.

Moore LA, Trussell LO (2017) Corelease of Inhibitory Neurotransmitters in the Mouse Auditory Midbrain. J Neurosci 37:9453–9464.

Mosbacher J, Schoepfer R, Monyer H, Burnashev N, Seeburg PH, Ruppersberg JP (1994) A molecular determinant for submillisecond desensitization in glutamate receptors. Science 266:1059–1062.

Mountain DC (1980) Changes in endolymphatic potential and crossed olivocochlear bundle stimulation alter cochlear mechanics. Science 210:71–72.

Mulders WH, Robertson D (2000) Evidence for direct cortical innervation of medial olivocochlear neurones in rats. Hear Res 144:65–72.

Mulders WHAM, Robertson D (2001) Origin of the noradrenergic innervation of the superior olivary complex in the rat. J Chem Neuroanat 21:313–322.

Mulders WHAM, Robertson D (2002) Inputs from the cochlea and the inferior colliculus converge on olivocochlear neurones. Hear Res 167:206–213.

Murugasu E, Russell IJ (1996) The effect of efferent stimulation on basilar membrane displacement in the basal turn of the guinea pig cochlea. J Neurosci Off J Soc Neurosci 16:325–332.

Ngodup T, Romero GE, Trussell LO (2020) Identification of an inhibitory neuron subtype, the L-stellate cell of the cochlear nucleus Bergles DE, Shinn-Cunningham BG, Bergles DE, eds. eLife 9:e54350.

Oertel D, Wright S, Cao XJ, Ferragamo M, Bal R (2011) The multiple functions of T stellate/multipolar/chopper cells in the ventral cochlear nucleus. Hear Res 276:61–69.

Oertel D, Wu SH, Garb MW, Dizack C (1990) Morphology and physiology of cells in slice preparations of the posteroventral cochlear nucleus of mice. J Comp Neurol 295:136–154.

Ono M, Bishop DC, Oliver DL (2017) Identified GABAergic and Glutamatergic Neurons in the Mouse Inferior Colliculus Share Similar Response Properties. J Neurosci 37:8952–8964.

Osen KK, Mugnaini E, Dahl AL, Christiansen AH (1984) Histochemical localization of acetylcholinesterase in the cochlear and superior olivary nuclei. A reappraisal with emphasis on the cochlear granule cell system. Arch Ital Biol 122:169–212.

Otsuka S, Nakagawa S, Furukawa S (2018) A preceding sound expedites medial olivocochlear reflex. Acta Acust United Acust 104:804–808.

Ottersen OP, Takumi Y, Matsubara A, Landsend AS, Laake JH, Usami S (1998) Molecular organization of a type of peripheral glutamate synapse: the afferent synapses of hair cells in the inner ear. Prog Neurobiol 54:127–148.

Pan B, Akyuz N, Liu X-P, Asai Y, Nist-Lund C, Kurima K, Derfler BH, György B, Limapichat W, Walujkar S, Wimalasena LN, Sotomayor M, Corey DP, Holt JR (2018) TMC1 Forms the Pore of Mechanosensory Transduction Channels in Vertebrate Inner Ear Hair Cells. Neuron 99:736-753.e6.

Petreanu L, Mao T, Sternson SM, Svoboda K (2009) The subcellular organization of neocortical excitatory connections. Nature 457:1142–1145.

Popelar J, Mazelová J, Syka J (2002) Effects of electrical stimulation of the inferior colliculus on 2f1−f2 distortion product otoacoustic emissions in anesthetized guinea pigs. Hear Res 170:116–126.

Rajan R (1988) Effect of electrical stimulation of the crossed olivocochlear bundle on temporary threshold shifts in auditory sensitivity. II. Dependence on the level of temporary threshold shifts. J Neurophysiol 60:569–579.

Rasmussen GL (1946) The olivary peduncle and other fiber projections of the superior olivary complex. J Comp Neurol 84:141–219.

Rasmussen GL (1953) Further observations of the efferent cochlear bundle. J Comp Neurol 99:61–74.

Reiter ER, Liberman MC (1995) Efferent-mediated protection from acoustic overexposure: relation to slow effects of olivocochlear stimulation. J Neurophysiol 73:506–514.

Rhode WS, Smith PH (1986) Encoding timing and intensity in the ventral cochlear nucleus of the cat. J Neurophysiol 56:261–286.

Robertson D (1984) Horseradish peroxidase injection of physiologically characterized afferent and efferent neurones in the guinea pig spiral ganglion. Hear Res 15:113–121.

Robertson D (1985) Brainstem location of efferent neurones projecting to the guinea pig cochlea. Hear Res 20:79–84.

Robertson D (2009) Centrifugal Control in Mammalian Hearing. Clin Exp Pharmacol Physiol 36:603–611.

Robertson D, Cole KS, Corbett K (1987) Quantitative estimate of bilaterally projecting medial olivocochlear neurones in the guinea pig brainstem. Hear Res 27:177–181.

Robertson D, Gummer M (1985) Physiological and morphological characterization of efferent neurones in the guinea pig cochlea. Hear Res 20:63–77.

Robertson D, Winter IM (1988) Cochlear nucleus inputs to olivocochlear neurones revealed by combined anterograde and retrograde labelling in the guinea pig. Brain Res 462:47–55.

Rodrigues AR a, Oertel D (2006) Hyperpolarization-activated currents regulate excitability in stellate cells of the mammalian ventral cochlear nucleus. J Neurophysiol 95:76–87.

Romand R, Avan P (1997) Anatomical and functional aspects of the cochlear nucleus. In: Ehret G, Romand R (eds) The central auditory system., pp pp 97-191. Oxford University Press, New York.

Ronzitti E, Emiliani V, Papagiakoumou E (2018) Methods for Three-Dimensional All-Optical Manipulation of Neural Circuits. Front Cell Neurosci 12:469.

Rossi J, Balthasar N, Olson D, Scott M, Berglund E, Lee CE, Choi MJ, Lauzon D, Lowell BB, Elmquist JK (2011) Melanocortin-4 receptors expressed by cholinergic neurons regulate energy balance and glucose homeostasis. Cell Metab 13:195–204.

Rothman JS, Silver RA (2018) NeuroMatic: An Integrated Open-Source Software Toolkit for Acquisition, Analysis and Simulation of Electrophysiological Data. Front Neuroinformatics 12:14.

Rubio ME (2020) Auditory brainstem development and plasticity. Curr Opin Physiol 18:7–10.

Russell IJ, Murugasu E (1997) Medial efferent inhibition suppresses basilar membrane responses to near characteristic frequency tones of moderate to high intensities. J Acoust Soc Am 102:1734–1738.

Ryan AF, Keithley EM, Wang Z-X, Schwartz IR (1990) Collaterals from lateral and medial olivocochhlear efferent neurons innervate different regions of the cochlear nucleus and adjacent brainstem. J Comp Neurol 300:572–582.

Safieddine S, Eybalin M (1992) Triple Immunofluorescence Evidence for the Coexistence of Acetylcholine, Enkephalins and Calcitonin Gene-related Peptide Within Efferent (Olivocochlear) Neurons of Rats and Guinea-pigs. Eur J Neurosci 4:981–992.

Saint Marie RL (1996) Glutamatergic connections of the auditory midbrain: Selective uptake and axonal transport of D-[3H]aspartate. J Comp Neurol 373:255–270.

Sakurai M (1987) Synaptic modification of parallel fibre-Purkinje cell transmission in in vitro guinea-pig cerebellar slices. J Physiol 394:463–480.

Saldaña E (2015) All the way from the cortex: a review of auditory corticosubcollicular pathways. Cerebellum Lond Engl 14:584–596.

Saul SM, Iv JAB, Altschuler RA, Shore SE, Rudolph DD, Kabara LL, Halsey KE, Hufnagel RB, Zhou J, Dolan DF, Glaser T (2008) Math5 expression and function in the central auditory system. Mol Cell Neurosci 37:153–169.

Schindelin J, Arganda-Carreras I, Frise E, Kaynig V, Longair M, Pietzsch T, Preibisch S, Rueden C, Saalfeld S, Schmid B, Tinevez JY, White DJ, Hartenstein V, Eliceiri K, Tomancak P, Cardona A (2012) Fiji: An open-source platform for biological-image analysis. Nat Methods 9:676–682.

Schofield BR, Beebe NL (2019) Descending Auditory Pathways and Plasticity. In: The Oxford Handbook of the Auditory Brainstem (Kandler K, ed), pp 610–638. Oxford University Press.

Schofield BR, Cant NB (1999) Descending auditory pathways: projections from the inferior colliculus contact superior olivary cells that project bilaterally to the cochlear nuclei. J Comp Neurol 409:210–223.

Sekitani M, Shiosaka S, Kuriyama H, Lee Y, Ikeda M, Tohyama M (1990) Transient expression of somatostatin mRNA in the auditory system of neonatal rat. Brain Res Mol Brain Res 7:177–181.

Simmons DD (2002) Development of the inner ear efferent system across vertebrate species. J Neurobiol 53:228–250.

Simmons DD, Mansdorf NB, Kim JH (1996) Olivocochlear innervation of inner and outer hair cells during postnatal maturation: evidence for a waiting period. J Comp Neurol 370:551–562.

Smith DW, Aouad RK, Keil A (2012) Cognitive task demands modulate the sensitivity of the human cochlea. Front Psychol 3:30.

Smith PH, Joris PX, Carney LH, Yin TC (1991) Projections of physiologically characterized globular bushy cell axons from the cochlear nucleus of the cat. J Comp Neurol 304:387–407.

Smith PH, Joris PX, Yin TC (1993) Projections of physiologically characterized spherical bushy cell axons from the cochlear nucleus of the cat: evidence for delay lines to the medial superior olive. J Comp Neurol 331:245–260.

Smith PH, Rhode WS (1989) Structural and functional properties distinguish two types of multipolar cells in the ventral cochlear nucleus. J Comp Neurol 282:595–616.

Smith PH, Spirou GA (2002) From the Cochlea to the Cortex and Back. In: Integrative Functions in the Mammalian Auditory Pathway (Oertel D, Fay RR, Popper AN, eds), pp 6–71 Springer Handbook of Auditory Research. New York, NY: Springer New York.

Sonntag M, Englitz B, Typlt M, Rübsamen R (2011) The calyx of Held develops adult-like dynamics and reliability by hearing onset in the mouse in vivo. J Neurosci Off J Soc Neurosci 31:6699–6709.

Sørensen AT, Cooper YA, Baratta MV, Weng F-J, Zhang Y, Ramamoorthi K, Fropf R, LaVerriere E, Xue J, Young A, Schneider C, Gøtzsche CR, Hemberg M, Yin JC, Maier SF, Lin Y (2016) A robust activity marking system for exploring active neuronal ensembles. eLife 5.

Sridhar T, Liberman M, Brown M, Sewell W (1995) A novel cholinergic “slow effect” of efferent stimulation on cochlear potentials in the guinea pig. J Neurosci 15:3667–3678.

Suthakar K, Ryugo DK (2017) Descending projections from the inferior colliculus to medial olivocochlear efferents: Mice with normal hearing, early onset hearing loss, and congenital deafness. Hear Res 343:34–49.

Suzuki J, Hashimoto K, Xiao R, Vandenberghe LH, Liberman MC (2017) Cochlear gene therapy with ancestral AAV in adult mice: complete transduction of inner hair cells without cochlear dysfunction. Sci Rep 7:45524.

Terreros G, Delano PH (2015) Corticofugal modulation of peripheral auditory responses. Front Syst Neurosci 9:134.

Tervo DGR, Hwang B-Y, Viswanathan S, Gaj T, Lavzin M, Ritola KD, Lindo S, Michael S, Kuleshova E, Ojala D, Huang C-C, Gerfen CR, Schiller J, Dudman JT, Hantman AW, Looger LL, Schaffer DV, Karpova AY (2016) A Designer AAV Variant Permits Efficient Retrograde Access to Projection Neurons. Neuron 92:372–382.

Thompson AM (1998) Heterogeneous projections of the cat posteroventral cochlear nucleus. J Comp Neurol 390:439–453.

Thompson AM, Schofield B (2000) Afferent Projections of the Superior Olivary Complex. Microsc Res Tech 51:355–363.

Thompson AM, Thompson GC (1991) Posteroventral cochlear nucleus projections to olivocochlear neurons. J Comp Neurol 303:267–285.

Thompson AM, Thompson GC (1993) Relationship of descending inferior colliculus projections to olivocochlear neurons. J Comp Neurol 335:402–412.

Thompson AM, Thompson GC (1995) Light microscopic evidence of serotoninergic projections to olivocochlear neurons in the bush baby (Otolemur garnettii). Brain Res 695:263–266.

Torres Cadenas L, Fischl MJ, Weisz CJC (2019) Synaptic inhibition of medial olivocochlear efferent neurons by neurons of the medial nucleus of the trapezoid body. J Neurosci:1288–19.

Trussell LO (1999) Synaptic mechanisms for coding timing in auditory neurons. Annu Rev Physiol 61:477–496.

Twomey EC, Yelshanskaya M V., Vassilevski AA, Sobolevsky AI (2018) Mechanisms of Channel Block in Calcium-Permeable AMPA Receptors. Neuron 99:956-968.e4.

Vetter DE, Adams JC, Mugnaini E (1991) Chemically distinct rat olivocochlear neurons. Synapse 7:21–43.

Vetter DE, Mugnaini E (1992) Distribution and dendritic features of three groups of rat olivocochlear neurons. Anat Embryol (Berl) 185:1–16.

Vetter DE, Saldaña E, Mugnaini E (1993) Input from the inferior colliculus to medial olivocochlear neurons in the rat: A double label study with PHA-L and cholera toxin. Hear Res 70:173–186.

Von Békésy G (1960) Experiments in hearing. Oxford, England: Mcgraw Hill.

von Engelhardt J, Eliava M, Meyer AH, Rozov A, Monyer H (2007) Functional Characterization of Intrinsic Cholinergic Interneurons in the Cortex. J Neurosci 27:5633–5642.

Walsh EJ, McGee J, McFadden SL, Liberman MC (1998) Long-term effects of sectioning the olivocochlear bundle in neonatal cats. J Neurosci Off J Soc Neurosci 18:3859–3869.

Walsh KP, Pasanen EG, McFadden D (2015) Changes in otoacoustic emissions during selective auditory and visual attention. J Acoust Soc Am 137:2737–2757.

Wang X, Robertson D (1997) Two Types of Actions of Norepinephrine on Identified Auditory Efferent Neurons in Rat Brain Stem Slices. J Neurophysiol 78:1800–1810.

Wang X, Robertson D (1998) Substance P-Induced Inward Current in Identified Auditory Efferent Neurons in Rat Brain Stem Slices. J Neurophysiol 80:218–229.

Warr WB (1972) Fiber degeneration following lesions in the multipolar and globular cell areas in the ventral cochlear nucleus of the cat. Brain Res 40:247–270.

Warr WB (1975a) Olivocochlear and vestibular efferent neurons of the feline brain stem: their location, morphology and number determined by retrograde axonal transport and acetylcholinesterase histochemistry. J Comp Neurol 161:159–181.

Warr WB (1975b) Olivocochlear and vestibular efferent neurons of the feline brain stem: their location, morphology and number determined by retrograde axonal transport and acetylcholinesterase histochemistry. J Comp Neurol 161:159–181.

Warr WB (1992) Organization of Olivocochlear Efferent Systems in Mammals. In: The Mammalian Auditory Pathway: Neuroanatomy (Webster DB, Popper AN, Fay RR, eds), pp 410–448 Springer Handbook of Auditory Research. New York, NY: Springer.

Warr WB (1995) Parallel Ascending Pathways from the Cochlear Nucleus. In: Contributions to Sensory Physiology, pp 1–38. Elsevier.

Warr WB, Beck Boche J, Neely ST (1997) Efferent innervation of the inner hair cell region: origins and terminations of two lateral olivochlear systems. Hear Res 108:89–111.

Warr WB, Beck Boche J, Ye Y, Kim DO (2002) Organization of Olivocochlear Neurons in the Cat Studied with the Retrograde Tracer Cholera Toxin-B. JARO - J Assoc Res Otolaryngol 3:457–478.

Warr WB, Guinan JJ (1979) Efferent innervation of the organ of corti: two separate systems. Brain Res 173:152–155.

Warren EH, Liberman MC (1989) Effects of contralateral sound on auditory-nerve responses. I. Contributions of cochlear efferents. Hear Res 37:89–104.

Weisstaub N, Vetter D, Elgoyhen A, Katz E (2002) The alpha9alpha10 nicotinic acetylcholine receptor is permeable to and is modulated by divalent cations. Hear Res 167:122–135.

Wersinger E, Fuchs PA (2011) Modulation of hair cell efferents. Hear Res 279:1–12.

White JS (1986) Differences in the ultrastructure of labyrinthine efferent neurons in the albino rat. In: ARO Abstr, pp 34–35.

Wiederhold ML, Kiang NYS (1970) Effects of Electric Stimulation of the Crossed Olivocochlear Bundle on Single Auditory-Nerve Fibers in the Cat. J Acoust Soc Am 48:950–965.

Wilson JL, Henson MM, Henson OW (1991) Course and distribution of efferent fibers in the cochlea of the mouse. Hear Res 55:98–108.

Winslow RL, Sachs MB (1987a) Effect of electrical stimulation of the crossed olivocochlear bundle on auditory nerve response to tones in noise. J Neurophysiol 57:1002–1021.

Winslow RL, Sachs MB (1987b) Effect of electrical stimulation of the crossed olivocochlear bundle on auditory nerve response to tones in noise. J Neurophysiol 57:1002–1021.

Wittekindt A, Kaiser J, Abel C (2014) Attentional modulation of the inner ear: A combined otoacoustic emission and EEG study. J Neurosci 34:9995–10002.

Woods CI, Azeredo WJ (1999) Noradrenergic and serotonergic projections to the superior olive: Potential for modulation of olivocochlear neurons. Brain Res 836:9–18.

Wu JS, Yi E, Manca M, Javaid H, Lauer AM, Glowatzki E (2020) Sound exposure dynamically induces dopamine synthesis in cholinergic LOC efferents for feedback to auditory nerve fibers King AJ, Carr CE, Evans M, Liberman C, Holt JC, eds. eLife 9:e52419.

Wu SH, Oertel D (1984) Intracellular injection with horseradish peroxidase of physiologically characterized stellate and bushy cells in slices of mouse anteroventral cochlear nucleus. J Neurosci 4:1577–1588.

Wu SH, Oertel D (1987) Maturation of synapses and electrical properties of cells in the cochlear nuclei. Hear Res 30:99–110.

Wynne B, Harvey AR, Robertson D, Sirinathsinghji DJ (1995) Neurotransmitter and neuromodulator systems of the rat inferior colliculus and auditory brainstem studied by in situ hybridization. J Chem Neuroanat 9:289–300.

Wynne B, Robertson D (1997) Somatostatin and substance P-like immunoreactivity in the auditory brainstem of the adult rat. J Chem Neuroanat 12:259–266.

Ye Y, Machado DG, Kim DO (2000) Projection of the marginal shell of the anteroventral cochlear nucleus to olivocochlear neurons in the cat. J Comp Neurol 420:127–138.

Zaitsev AV, Kim KK, Fedorova IM, Dorofeeva NA, Magazanik LG, Tikhonov DB (2011) Specific mechanism of use-dependent channel block of calcium-permeable AMPA receptors provides activity-dependent inhibition of glutamatergic neurotransmission. J Physiol 589:1587–1601.

Zeilhofer HU, Studler B, Arabadzisz D, Schweizer C, Ahmadi S, Layh B, Bösl MR, Fritschy J-M (2005) Glycinergic neurons expressing enhanced green fluorescent protein in bacterial artificial chromosome transgenic mice. J Comp Neurol 482:123–141.

Zhang W, Dolan DF (2006) Inferior colliculus stimulation causes similar efferent effects on ipsilateral and contralateral cochlear potentials in the guinea pig. Brain Res 1081:138–149.

Zhao W, Dhar S (2011) Fast and Slow Effects of Medial Olivocochlear Efferent Activity in Humans. PLoS ONE 6.

Zheng J, Shen W, He DZ, Long KB, Madison LD, Dallos P (2000) Prestin is the motor protein of cochlear outer hair cells. Nature 405:149–155.

Zucker RS, Regehr WG (2002) Short-term synaptic plasticity. Annu Rev Physiol 64:355–405.